Global Nonlinear Analysis of Piezoelectric Energy Harvesting from Ambient and Aeroelastic Vibrations

Abdessattar Abdelkefi

Dissertation submitted to the faculty of the
Virginia Polytechnic Institute and State University
in partial fulfillment of the requirements for the degree of

Doctor of Philosophy
in
Engineering Mechanics

Ali H. Nayfeh, Co-Chair
Muhammad R. Hajj, Co-Chair
Mark R. Paul
Saad A. Ragab
Craig A. Woolsey

July 12, 2012
Blacksburg, Virginia

Keywords: Energy harvesting, piezoelectricity, aeroelasticity, electromechanical modeling, nonlinear dynamics, vortex-induced vibrations

Global Nonlinear Analysis of Piezoelectric Energy Harvesting from Ambient and Aeroelastic Vibrations

Abdessattar Abdelkefi

(ABSTRACT)

Converting vibrations to a usable form of energy has been the topic of many recent investigations. The ultimate goal is to convert ambient or aeroelastic vibrations to operate low-power consumption devices, such as microelectromechanical systems, heath monitoring sensors, wireless sensors or replacing small batteries that have a finite life span or would require hard and expensive maintenance. The transduction mechanisms used for transforming vibrations to electric power include: electromagnetic, electrostatic, and piezoelectric mechanisms. Because it can be used to harvest energy over a wide range of frequencies and because of its ease of application, the piezoelectric option has attracted significant interest.

In this work, we investigate the performance of different types of piezoelectric energy harvesters. The objective is to design and enhance the performance of these harvesters. To this end, distributed-parameter and phenomenological models of these harvesters are developed. Global analysis of these models is then performed using modern methods of nonlinear dynamics. In the first part of this Dissertation, global nonlinear distributed-parameter models for piezoelectric energy harvesters under direct and parametric excitations are developed. The method of multiple scales is then used to derive nonlinear forms of the governing equations and associated boundary conditions, which are used to evaluate their performance and determine the effects of the nonlinear piezoelectric coefficients on their behavior in terms of softening or hardening.

In the second part, we assess the influence of the linear and nonlinear parameters on the dynamic behavior of a wing-based piezoaeroelastic energy harvester. The system is composed of a rigid airfoil that is constrained to pitch and plunge and supported by linear and nonlinear torsional and flexural springs with a piezoelectric coupling attached to the plunge degree of freedom. Linear analysis is performed to determine the effects of the linear spring coefficients and electrical load resistance on the flutter speed. Then, the normal form of the

Hopf bifurcation (flutter) is derived to characterize the type of instability and determine the effects of the aerodynamic nonlinearities and the nonlinear coefficients of the springs on the system's stability near the bifurcation. This is useful to characterize the effects of different parameters on the system's output and ensure that subcritical or "catastrophic" bifurcation does not take place. Both linear and nonlinear analyses are then used to design and enhance the performance of these harvesters.

In the last part, the concept of energy harvesting from vortex-induced vibrations of a circular cylinder is investigated. The power levels that can be generated from these vibrations and the variations of these levels with the freestream velocity are determined. A mathematical model that accounts for the coupled lift force, cylinder motion and generated voltage is presented. Linear analysis of the electromechanical model is performed to determine the effects of the electrical load resistance on the natural frequency of the rigid cylinder and the onset of the synchronization region. The impacts of the nonlinearities on the cylinder's response and energy harvesting are then investigated.

Dedicated to

My wife Samah

My parents Mihrziya and Afif

My parents in law Chefia and Mohamed

My brothers Aymen and Omar

My brothers in law Houda and Ahmed

All my family and my friends

My supervisors

Acknowledgments

First of all, I thank ALLAH, the most Merciful and most Gracious, for this achievement.

I would like to express my deepest gratitude and appreciation to my advisors, Professors Ali H. Nayfeh and Muhammad R. Hajj, for giving me the opportunity to work with them. Professors Nayfeh and Hajj have been great advisors who were always available to discuss and carefully guide my research. They provided a very helpful research environment that allowed me to work on several research projects and collaborate with other students and professors. With their great advice and precious guidance, Professors Nayfeh and Hajj gave me the opportunity to develop my own academic style during the past two years and a half. They encouraged me to write journal papers and attend several conferences. My previous two years and a half have been the most important stage in my professional life during whoch I was able to meet and discuss my research with these two prestigious professors. My dream is to follow my advisors' career for the rest of my life.

I would also like to thank Profs. Mark Paul, Saad Ragab, and Craig Woolsey for serving on my PhD Committee and for their support and useful feedback about my research.

I would like to especially thank Prof. Abdullah Nuhait of King Saud University for having introduced me to the unsteady vortex lattice method and for contributing to my work with beneficial advice and meaningful discussions. Special thanks also go to Prof. Flavio Marques and his student Rui Vasconcellos of the University of Sao Paolo for giving me the opportunity to work with them on aeroelastic problems (not covered here). Rui Vasconcellos is one of the best students that I have met in my life. He helped me a lot in preparing my experiments at the Department of Engineering Science and Mechanics. I thank him as well for his interesting discussions in the field of aeroelasticity. Special thanks also go to my colleague Dr. Mehdi

Ghommem who was my office mate. We have worked together on many problems. I have enjoyed collaborating with him on aeroelastic phenomena (not covered here) during the first two years of my PhD studies.

As a teacher, Prof. Nayfeh taught me perturbation techniques, normal forms, and nonlinear dynamics. I thank him for his precious directions when applying the Method of Multiple Scales and the Center-Manifold for piezoelectric energy harvesters.

Professor Hajj taught me digital time series and identification techniques of nonlinear systems, which have been beneficial in my research. He also gave me the opportunity to participate and work with his other students and visitors. He has helped me develop my professional career. I have had the great pleasure to work with Arshad Mehmood on vortex-induced vibration problems and with Youssef Bichiou on aeroelastic and wind-turbine problems. Finally, I would like to thank Abdulmohsen Alothman and Zhimiao Yan; two students I am mentoring in starting their PhD research on thermoelectric generators and galloping energy harvesters, respectively.

I would like to extend my appreciation to the Department of Engineering Science and Mechanics and particularly to the Graduate Committee for honoring me with the prestigious awards: Liviu Librescu Memorial Scholarship and Amir Chand and Dewki Bai Batra Scholarship in my first two years at this Department. These awards have made me more responsible and given me a strong push to pursue my engineering education with greater pledge.

I would like to thank all staff members of the Department of Engineering Science and Mechanics. Special thanks go to Lisa Smith and Sally Shrader for their precious help.

My deep thanks go to my wife Samah Ben Ayed whose encouragement, love, advice, and prayers have been the main source of my success in my life and particularly in my PhD.

I would like to thank my mother Mihrziya Abida, my father Afif Abdelkefi, my mother-in-law Chefia Elleuch, my father-in-law Mohamed Ben Ayed, my brothers Aymen and Omar Abdelkefi, and my brothers-in-law Houda and Ahmed Ben Ayed. Thanks for their encouragement, support, sincere kindness, and prayers.

Special thanks go to Dr. Saher Lahouar and his wife Afek Jaballah, Omar Al-Abbasi and his wife Yasmeen Al-Khaja, Dr. Shouib Maabdah and his wife Lubna Shihadah, Zakariya Dalalah and his wife Wafa Arshedet, and Faycal Beji and his wife Autumn Taylor for their

help and encouragement. I and my wife will never forget the good moments that we spent with these families. I wish them all the best in their lifes.

I shall also mention all of my colleagues in the Department of Engineering Science and Mechanics, namely former students (Drs. Andrea Mola and Giovanni Sansavini) and current students (Mohamed Jrad, Bilel Aydi, Najib Masghouni, Hassan Fayed, Haitham Taha, Kareem Akhtar, Ahmad Naveed, Yasser Aboelkassem, and Brendan Kullback) who have been great friends. I would like also to thank all my friends in Blacksburg, namely Dr. Mohamed Ben Romdhane, Dr. Amara Loulizi, Ahmed Ali, Karim Fadhloun, and Khaled Adjerid. My thanks go to my best friends in Tunisia Morsi Ben Ayed, Said Mseddi, Firas Atitallah, Ali Mohamed, Mehdi felhi, Bilel Fehri, Ala Zouaghi, Mohamed Amami, Omar Agili, and Slim Ben Hlima.

I am also grateful to Profs. Slim Choura, Sami El-Borgi, and Fehmi Najar for having recommended me to the Department of Engineering Science and Mechanics.

Contents

List of Figures

List of Tables

Chapter 1

Introduction

The interest in using natural energy sources, such as thermal energy (1), chemical, light energy (2) and mechanical energy (3), to generate inexhaustible electric energy has grown over the past two decades. Such energy harvesters have been proposed to operate self-powered devices, including microelectromechanical systems or actuators (4–6), health monitoring, and wireless sensors (7; 8), or to replace small batteries that have a finite life span or would require hard and expensive maintenance (9–11). For powering electronic devices, mechanical energy has received the most attention because it is readily available. Harvesting mechanical energy through converting vibrations to electrical energy can be achieved using either electromagnetic (12–14), electrostatic (14; 15), or piezoelectric (15–18) transduction. Of these mechanisms, the piezoelectric transduction is most suitable for MEMS devices (4) and wireless sensors (7; 8); mostly because it can be effectively placed in small volumes and used to harvest energy over a wide range of frequencies. Piezoelectric energy conversion occurs when strain energy is applied to a piezoelectric material resulting in a deformation of the electric dipole and the formation of electrical charge and current.

The harvested power depends on the quantity and available form of kinetic energy and the efficiency of the harvester. Over the last decade, many investigations have been concerned with harvesting energy from base vibrations (3; 15–17; 19–36). On the other hand, harvesting energy from aeroelastic vibrations or flow-induced vibrations has been the topic of more recent investigations. In both applications, one or two piezoceramic layers bounded by electrodes

that generate an alternating voltage output are used to convert the ambient or aeroelastic vibrations to electrical power. The electrodes are externally connected by an electric circuit that is usually modeled as a simple electrical load resistance.

In this Dissertation, we investigate the performance of different types of piezoelectric energy harvesters. The objectives are to design and enhance the performance of these harvesters. To this end, distributed-parameter and phenomenological models of these harvesters are developed. Global analysis of these models is then performed using modern methods of nonlinear dynamics. The use of these models for accurate prediction of the harvester's performance in each case is also discussed.

1.1 Energy Harvesting through Piezoelectric Configurations

The piezoelectric effect was discovered by Pierre and Jacques Curie in 1880. There are two distinct piezoelectric effects. The direct piezoelectric effect describes the ability of some materials (such as quartz, Rochelle salt, tourmaline, and barium titanate) to transform mechanical strain into electrical charge. This effect is used to convert the mechanical strain to electrical energy. The second piezoelectric effect is the converse effect, which is the ability to convert an applied electrical potential into mechanical strain.

To convert mechanical vibrations to a usable form of energy, different types of piezoelectric materials have been used. The most common type is the lead zirconate titanate (PZT). This piezoelectric material is widely employed to harvest energy. However, PZT is brittle, thereby causing limitations in the applied strain. Furthermore, when it is subjected to high-frequency motions, piezoceramic is susceptible to fatigue crack and can be easily damaged (15; 37). To avoid this characteristic of piezoceramic transducers and improve their efficiency and flexibility, researchers have developed, more flexible piezoelectric material, namely, polyvinylindene fluoride (PVDF). Kymissis et al. (38) investigated power harvesting from piezoelectric shoes using a unimorph strip made of piezoceramic composite material and a stave made from a multilayer laminate of PVDF foil that periodically broadcasts a digital radio frequency wireless identification (RFID) as the bearer walks. Because of the shoe's toe flexibility, the PVDF stave was set into the front of an athletic shoe. It was determined that the average

generated power by the stave is around 1.3 mW at 0.9 Hz walking pace when the electrical load resistance is set equal to 250 $k\Omega$. PZT unimorphs working off heel were implemented into a US Navy work boot that has a rigid heel cup. The generated power of two curved PZT unimorphs in a clam shell configuration is around 8.4 mW for a load resistance of 500 $k\Omega$. The feasibility of piezoelectric energy harvesting from shoes was proven by creating and installing a self-powered radio frequency (RF) tag into the shoe. It was demonstrated that, during walking, the tag was capable of transmitting a short-range 12-bit wireless identification (ID) code.

A PVDF film coated with poly(3,4-ethylenedioxy-thiophene) (PEDOT) and poly(4-styrenesulfonate) (PSS) electrodes, was developed by Lee et al. (37; 39) who studied its efficiency compared to the inorganic electrode materials, indium tin oxide (ITO) and platinum (Pt). The films with ITO electrodes were destroyed due to fatigue crack at a frequency of 213 Hz. The Pt electrodes showed fatigue crack at a frequency of 33 kHz. The results showed that the PEDOT/PSS film is more resistant and lasted at 1 MHz for about 10 $hours$ without damage to the electrodes. Consequently, the electrodes have an important influence on the behavior of the piezoelectric material. The results also showed that a piezoelectric transducer can operate over a wide range of frequencies.

The efficiencies of three piezoelectric materials were investigated by Sodano et al. (40): a traditional PZT, a quick pack (QP) actuator, and the macro-fiber composite (MFC). Each material was subjected to a resonance excitation, a 0-500 Hz chirp, random excitations. The efficiency of the harvester was computed by measuring the power into the system and the harvested power for frequencies between 0 and 500 Hz. The efficiency of the traditional PZT is the highest one for all considered vibration types. The QP has a higher efficiency than the MFC. It was also demonstrated that PZT-5A yields the largest amount of harvested power when using the same dimensions (41).

For power harvesting, flexible piezoelectric materials have received significant attention because of their ability to resist large strain levels needed to increase the level of the harvested energy. Furthermore, piezoelectric energy harvesters can work in two different coupling modes: the –31 mode and the –33 mode, as shown in Figure 1.1. For the first coupling mode –31, a lateral force is applied in the direction perpendicular to the poling direction; an exam-

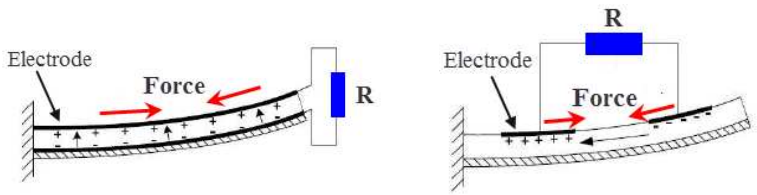

(a) (b)

Figure 1.1: Two types of piezoelectric energy harvesters: (a) –31 mode and (b) –33 mode.

ple of which is a bending cantilever beam that has electrodes on the top and bottom surfaces, as shown in Figure 1.1 (a). For the second coupling mode –33, a lateral force is applied in the same direction as the poling direction, such as the example illustrated in Figure 1.1 (b) where a bending cantilever beam has all electrodes on the top surface. The first coupling mode –31 is the most commonly used (15) because, when a cantilever beam bends, it is easier to use the –31 coupling mode in comparison to the –33 coupling mode simply because bending of the cantilever beam produces more lateral stress than vertical stress. However, the –31 coupling mode yields lower coupling coefficients than the second coupling mode (42). Baker et al. (42) demonstrated that the stack, which has higher coupling coefficients, is more robust. On the other hand, when subjected to the same force amplitude, the piezoelectric cantilever beam generates two orders of magnitude more power than the piezoelectric stack. Baker et al. (42) explained that this is due to the importance of the mechanical stiffness in the piezoelectric stack compared to the piezoelectric cantilever beam. This high mechanical stiffness results in a difficult production of the mechanical strain and then a reduction in the level of the harvested voltage and power. Baker et al. (42) also demonstrated that, depending on the subjected force amplitude, the first or second coupling modes are more beneficial. For a small-amplitude force, the –31 coupling mode, used in the piezoelectric cantilever beam, is more efficient. On the other hand, for high force amplitudes, such as in large operating machinery, the piezoelectric stack configuration is more durable and generates more useful power (15).

1.2 Piezoelectric Energy Harvesting from Base Excitations

As a part of this Dissertation, we focus on piezoelectric energy harvesters under base or ambient excitations. The most common vibration-based energy harvester consists of a composite cantilever beam with one or two piezoelectric layers. These layers are bounded by electrodes that harvest the produced voltage. The electrodes are externally connected by an electric circuit that is usually modeled as a simple electrical load resistance. Furthermore, in many applications, the ambient vibrations may be random or composed of a few discrete frequency components (43). Ambient vibrations suitable for energy harvesting can be found in various aspects of human experience, such as buildings, bridges, machines, etc. Luca et al. (44) presented numerous spectra of vibrations of a car hood in motion, an operating microwave oven, and a running train floor. They showed that these vibrational energy sources vary significantly, depending on the nature of motion. The presence of various behaviors in the natural vibration energy sources gives the opportunity to develop energy harvesters, depending on the available frequencies. In the literature, several studies (42; 45–54) have been proposed to tune the global fundamental frequency of a harvester to the dominant frequency of the excitation. Other studies (35; 55–61) have focused on harvesting energy from random vibrations or noise displacements.

1.2.1 Linear representations and enhancement of energy harvesters

Modeling piezoelectric energy harvesters is used to estimate or determine the voltage output and hence the level of harvested power across an electrical circuit when it is subjected to a base vibration. Several studies have focused on the coupled electromechanical problem of piezoelectric energy harvesters under base vibrations. Roundy et al. (62) and duToil et al. (63) modeled a piezoelectric cantilever beam as a mass-spring-damper system. Such a model is limited to the fundamental frequency of the structure and it does not account for the effects of the dynamic mode shapes on the electrical response of the harvester. The effect of the spring mass (distributed mass) was not considered in the forcing amplitude. This assumption can lead to erroneous results particularly if the proof mass is small. Erturk and Inman (22) showed that the use of the traditional form of the lumped-parameter model

leads to erroneous results for both transverse and longitudinal cantilevered beams under base vibrations. They showed that the predicted response can be underestimated when using the conventional effective mass of cantilevered beams or bars. This is particularly true when there is a small or no tip mass. They introduced correction factors to improve the prediction capability of lumped models for harmonic base excitation for both transverse and longitudinal vibrations.

An improved model that is based on the Rayleigh-Ritz discrete formulation was used by Sodano et al. (64) and duToil et al. (63). This method is more accurate in comparison to the lumped-parameter models. Using the Euler-Bernoulli beam theory, Sodano et al. (64) and duToil et al. (63) employed the Rayleigh-Ritz discrete formulation to model a cantilevered piezoelectric energy harvester. Their approach accounted for the effects of the higher vibration modes on the electromechanical response of the harvester.

Several investigations have been performed to maximize the level of the harvested power of piezoelectric energy harvesters. Anton and Sodano (15) presented in their review paper some strategies to enhance the level of the harvested power using more efficient piezoelectric materials, using distinct piezoelectric mode couplings, and by optimizing the power conditioning circuitry. In order to enhance the level of the harvested power, different efforts investigated the effects of varying the beam shapes (65), using asymmetric tip masses (a bending-torsion energy harvester) (29; 36), using an axially compressed piezoelectric bimorph in order to decrease resonance frequency (50; 66), and using a multilayer structure (67).

1.2.2 Nonlinear representations of energy harvesters

Although the piezoelectric constitutive equations are nonlinear, most of the current analyses consider only the linearized form of these equations. Yet, the nonlinear behavior of piezoelectric cantilever beams has been considered for the actuation purpose (68–73). Recently, nonlinear modeling of piezoelectric energy harvesters from base excitations has received some attention. In most of these studies, authors considered a single-mode representation, even in the presence of quadratic and cubic nonlinearities. In other studies, the added coupling between the mechanical and the electrical equations was taken into account.

Hu et al. (74) studied theoretically the performance of a piezoelectric harvester near

resonance under thickness/shear vibrations. The physical basis of their electromechanical representation was the cubic theory of nonlinear electroelasticity (75–77). Triplett and Quinn (78) considered a nonlinear lumped model by including a nonlinear term in the electromechanical coefficient. They demonstrated that nonlinearities in the electromechanical coupling can increase the harvested electrical power. Based on the nonlinear Euler-Bernoulli beam theory, Masana and Daqaq (50) developed an electromechanical model of a clamped-clamped energy harvester subjected to transverse excitations and static axial loading based on a one-mode Galerkin discretization without considering the linear and nonlinear piezoelectric effects. Stanton et al. (28) identified the nonlinear coefficients based on a nonlinear least-squares optimization algorithm that utilizes an approximate analytical solution obtained by the method of harmonic balance. Their energy harvester is a bimorph cantilever beam without tip mass and subjected to direct excitations. In their analysis, they considered a one-mode approximation for the identification. Daqaq et al. (79) studied energy harvesting using a parametric excitation. In their approach, the dynamic response of the system was investigated using a lumped-parameter model. They only used the first mode and did not account for piezoelectric effects on the beam response or for quadratic and cubic nonlinear piezoelectric coupling.

1.3 Piezoelectric Energy Harvesting from Aeroelastic Vibrations

1.3.1 Aeroelastic instabilities

When a structure is subjected to wind loads, it may undergo various responses (80–87), such as vortex-induced vibrations, flutter, buffeting, and galloping, which may result in unwanted and excessive vibrations. In the fields of civil and aerospace engineering, researchers work on avoiding these types of vibrations to reduce possible damage. On the other hand, the aerodynamic instability phenomena can be exploited to harvest energy. In this section, we discuss some of these aerodynamic instability phenomena that can be used as a source of harvesting energy.

Flutter phenomenon

Flutter is an aerodynamic instability phenomenon. As the wind speed increases, there may be a point at which self-excited motions take place because the structural damping is insufficient to damp out motions, which are due to coupled aerodynamic effects.

Vortex-induced vibrations

When a fluid flows past a bluff body, the flow exhibits the so-called Karman vortex street. This street consists of vortices that shed from both sides of the bluff body. The alternate shedding of these vortices causes unsteady aerodynamic forces on the body. When these vortices are shed at a frequency near the natural frequency of the bluff body, lock-in or synchronization takes place and resonant transverse vibrations occur (88–104). These vibrations are referred to as vortex-induced vibrations (VIV).

Galloping phenomenon

Galloping is a large-amplitude aeroelastic oscillation that can be exhibited by prismatic cylinders with different types of cross-section, such as triangles, squares, D-section, etc. The oscillation occurs in a plane normal to the incoming flow. The galloping phenomenon takes place when the derivative of the steady state aerodynamic lift coefficient is negative. This is known as the Den Hartog (105) necessary condition for galloping.

1.3.2 Wing-based piezoaeroelastic energy harvesters

Aeroelastic flutter in two-dimensional wings is a self-excited instability phenomenon. For an elastically-mounted wing, flutter takes place at a critical speed, named flutter speed, at which the structural damping is insufficient to damp out the oscillations. Below this critical speed, any disturbance in the pitch and plunge direction will decay. Above the flutter speed, the pitch and plunge oscillations grow drastically for a linear configuration. Complex aeroelastic responses such as divergence, limit-cycle oscillations (LCOs), internal resonances, chaos and bifurcations can take place. These responses affect the performance of the aircraft and may result in structural problems and material fatigue (80; 106–109). Regarding

structural nonlinearities, they can arise from large structural deflections and/or partial loss of structural integrity (110–114). Furthermore, the effects of aging, loose attachments, and material features could lead to undesirable and dangerous responses (37; 114–116). To ensure the safety of the aircrafts, bridges, and other structures, these complex aeroelastic phenomena must be avoided or controlled. In the literature of aeroelasticity, piezoelectric materials (as actuators, converse effect) and other actuators have been used as active or passive controllers to modify the aeroelastic behavior of wings (117–124). Researchers have also used piezoelectric materials as actuators for morphing wings or morphing aircrafts (125; 126). Macro-Fiber-Composite (MFC) actuators have been used to suppress buffeting oscillations on the vertical fins of an F-18 (127; 128). From a different perspective, these responses have been proposed as a new source of power generation. The nonlinearities responsible for these responses can be classified as either distributed or concentrated depending on the region of their existence. Distributed nonlinearities arise generally from deformations of the entire structure. Concentrated nonlinearities arise from loose or worn hinges of control surfaces.

Observations based on experimental studies

Recently, several studies have focused on wing-based piezoaeroelastic energy harvesters. Erturk et al. (129) investigated energy harvesting from a flow-excited morphing airfoil. In their study, the span of the used airfoil is 133 mm and its chord is 127 mm. The airfoil is a flat plate bimorph with four M 8557 P1 MFC piezoceramic patches (two on the top surface and two on the bottom surface) where the substrate material is stainless steel. They considered only the two piezoelectric patches on the top surface for power generation. Their experimental results showed that the maximum root mean square (RMS) level of the harvested power is about 7 μW and was obtained when the angle of attack was set equal to 20 *degrees* and for an electrical load resistance equal 98 $k\Omega$ at a flow velocity of 15 m/s. Anton and Inman (130) performed a proof of concept study for piezoelectric energy harvesting from unmanned air vehicle (UAV) driving a flight test of a remote controlled aircraft. The aircraft had a wing span of 1.8 m, a length of 1.1 m, and a flying weight of 0.9 Kg out of the box. This particular plane was selected primarily because of its long wing span and flexible foam wings, which provide a good environment for piezoelectric vibration harvesting using wing deflections. An

MFC patch was attached to the spar with epoxy under vacuum at locations near the roots of the wings. The MFC patch is a M8507-P1 with a length of 10.2 cm, width of 1.6 cm, thickness of 0.3 mm, and a mass of 3 g. They reported that a small battery can be fully charged when increasing the volume of piezoelectric material. They presented the possibility of installing a small on-board camera that can take photographs during flight.

Wing-based piezoaeroelastic energy harvester: Linear theoretical and experimental models

Bryant and Garcia (131) proposed and analyzed theoretically a two degree of freedom airfoil section as a power harvesting device driven by aeroelastic vibrations. The airfoil was attached to a cantilever beam. A time-domain switching energy extracting scheme was considered in order to increase the level of harvested power from linear aeroelastic vibrations. They reported that this method takes advantage of the damping effect by removing electrical energy from the system through the piezoelectric to dynamically shift the stability of the aeroelastic system. Bryant and Garcia (132) reported experimentally a piezoelectric energy harvesting device driven by aeroelastic flutter vibrations which is modeled as a two degree of freedom typical section. A time-domain linear analysis was performed to determine the linear flutter speed of the device. They performed a wind tunnel test for two wing geometries which are a flat plate and a NACA 0012 airfoil. They reported that the wing section geometry did not affect the linear flutter speed and its frequency. They also showed that the optimal wing profile depends on the operating range of wind speeds and on the required level of harvested power.

An electromechanical linear analysis was performed by Elvin et al. (133) of a cantilever pipe to investigate the effects of passive piezoelectric damping with a load resistance on the flutter speed. They reported that the mechanical stiffening effects of the open-circuit causes an increase in the flutter speed compared to the short-circuit. They showed that the larger the piezoelectric electromechanical coupling coefficient, the larger is flutter speed. They reported that the piezoelectric capacitance has a small effect on the variations of the flutter speed.

Erturk et al. (134) presented a frequency domain analysis and experimental validations for a two degree of freedom airfoil section as a wing-based piezoaeroelastic energy harvester. In their study, they focused on the linear problem of harvesting energy near the flutter

boundary. They analyzed the effects of the piezoelectric coupling on the linear flutter speed. They reported an electrical harvested power of 10.7 mW for an electrical load resistance is set equal to 100 $k\Omega$ for a freestream velocity close to the linear flutter speed which is 9.30 m/s. In their mathematical modeling, they introduced a piezoelectric coupling to the plunge degree of freedom and considered a load resistance in the electrical field. They reported a very good agreement between the considered mathematical model and the experimental data. They showed that the generated voltage increases when increasing the electrical load resistance. Furthermore, there is an optimum value of the electrical load resistance for which the harvested power is maximized. They also reported that the percentage increase in the linear flutter speed depends on the electrical load resistance and there is a maximum value of the flutter speed for a specific value of the load resistance.

De Marqui et al. (135) presented a time-domain piezoaeroelastic model and numerical simulations of a generator wing with embedded piezoceramics for continuous- and segmented-electrode configurations. Their wing-based piezoaeroelastic energy harvester model was obtained by combining an electromechanically coupled finite element (FE) model (136) based on the classical plate theory with an unsteady vortex-lattice model (137; 138) representing the aerodynamic loads. They reported that low aerodynamic damping was obtained at low wind speeds and close to the flutter speed. They also showed that when using segmented electrodes, torsional motions of the coupled modes become more important and therefore change the linear flutter speed value and improve the broadband performance of the harvester. They also reported that the level of harvested power is more significant for the segmented-electrode than the continuous-electrode for a freestream velocity of 40 m/s in their specific case of study.

De Marqui et al. (139) analyzed a frequency domain piezoaeroelastic model of a generator wing with continuous electrodes. They used the doublet-lattice method to represent the unsteady aerodynamic loads. The p-k scheme (140) was used to solve the piezoaeroelastic equations. They also presented the frequency response functions (FRFs) for a desired wind speed and external circuit in which they combined the effects of the base excitation condition and the unsteady aerodynamic loads in the coupled system. They showed that the use of segmented electrodes could eliminate the cancellation and improve the performance of

the piezoaeroelastic energy harvester. They also demonstrated that the performance of the harvester can be enhanced by using a resistive-inductive circuit in the electrical domain instead of using a load resistance. In fact, over almost the entire range of frequencies, the level of harvested power obtained when using resistive-inductive circuit is about 20 times larger than the resistive case for the short circuit flutter speed and short circuit flutter frequency. They also reported that the linear flutter speed is increased by 7.5 % in the resistive-inductance circuit when compared to the resistive one.

Doare and Michelin (141) presented theoretically the possibility of harvesting energy from the flutter of a flexible plate subjected to an axial flow. This plate was equipped with small length piezoelectric patches on both sides. They presented local and global stability analyses based on the global coupled electromechanical equations of motion. They reported that using piezoelectric patches makes the flexible plate more rigid and adds damping. They also observed a destabilization by dissipation for negative energy waves propagating in the medium which results in enhancing the energy conversion efficiency.

Wing-based piezoaeroelastic energy harvester: Nonlinear theoretical and experimental models

In general, all of the above studies have stressed the linear characteristics of the piezoaeroelastic energy harvester with particular attention paid to the effect of different parameters on the flutter speed. Yet, the risks and potential of energy harvesting from aeroelastic systems can be best evaluated from assessing their nonlinear responses, such as limit-cycle oscillations, which can be controlled to yield a finite amplitude harvested power and to eliminate unwanted responses. These aspects can best be determined by performing nonlinear analysis of wing-based piezoaeroelastic energy harvesters.

Generally, the nonlinear response of an aeroelastic system involves a combination of nonlinear phenomena. When these nonlinearities (geometric, inertia, freeplay, damping, and/or aerodynamic) are combined, they lead to various behaviors, including multiple equilibria, bifurcations, limit cycles, chaos, and various types of resonances (internal and super/subharmonic). In the analysis of aeroelastic systems, the interest usually lies in their response near or at the onset of a bifurcation point. In this region, and depending on the

magnitudes and types of nonlinearities, the bifurcation can be of the supercritical or subcritical instability as shown in Figure 1.2. For the purpose of energy harvesting, it is important to design enhanced and safe piezoaeroelastic energy harvesters that can generate energy at low speeds and, as such, to decrease the flutter speed. Furthermore, it is important to attain limit-cycle oscillations at low freestream velocities while avoiding subcritical Hopf bifurcations, which can lead to catastrophic failures.

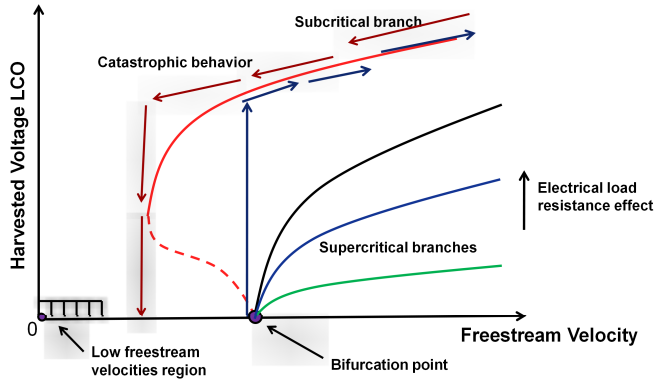

Figure 1.2: Schematic of LCO response of a piezoaeroelastic energy harvester airflow

1.3.3 Cylinder-based piezoaeroelastic energy harvesters

Allen et al. (142) investigated the response of a flexible membrane with PVDF or 'eel' to a fluid force due to vortex shedding downstream from a flat plate normal to the flow stream in a water tunnel. The vortices behind the bluff body caused the 'eel' to swing from one side to the other. They reported that membranes are able to exhibit lock-in behavior when the shedding frequency is near the fundamental frequency of the membrane. Taylor et al. (143) applied the 'eel' concept to harvest energy from ocean waves. They used a PVDF piezoelectric polymer to generate power. A prototype 'eel' was created and tested in a flow tank 241.3 mm long, 76.2 mm wide, and 150 μm thick. Their results showed that the harvested power

can be enhanced when the flapping frequency matches the vortex shedding frequency. They measured the generated voltage by the 'eel' to be the order of 3 V for a water velocity of 0.5 m/s. They did not provide any comparison between the simulations and experimental results of the outcome displacement, voltage output, and harvested power. Similar to the 'eel' created by Taylor et al. (143), Pobering and Schwesinger (144) investigated the use of a PVDF flag to harvest energy from flowing water. Their theoretical results showed that the harvested power can be the order of 68 W/m^3 for a river flowing at 2 m/s. However, these numbers were not validated.

The possibility of harvesting energy from forces generated by the von Karman vortex street behind a rectangular micro-prism in the laminar flow regime was investigated by Sanchez-Sanz et al. (145). Their objective was to assess whether this phenomenon could be used to harvest energy. They presented design guidelines for their energy-harvesting devices without giving any details about the fabrication procedure and experiments of the proposed device.

Wang and Ko (146) reported a small scale piezoaeroelastic energy harvester based on the von Karman vortex street. The harvester had a flexible diaphragm with a PVDF film being attached to it. Below this diaphragm, there was a chamber with flowing water. The pressure in the chamber causes the diaphragm to deflect in the upward direction. The diaphragm oscillating motion with the piezoelectric film gives the possibility to generate energy. They reported a maximum generated voltage of about 2.2 V_{pp} and an instantaneous power of about 0.2 μW when the excitation pressure oscillates with an amplitude of 1.196 kPa and a frequency of about 26 Hz. For this harvester, the active volume was 50 mm, 30 mm, and 7 mm. In a similar work, Wang et al. (147) used almost the same strategy by adding a bluff body at the center of the chamber. They reported that the movement of the diaphragm bent the piezoelectric film and hence generated energy. Their experimental results showed a maximum generated voltage of an open-circuit of the order of 0.12 V_{pp} and an instantaneous power of 0.7 nW when the pressure oscillates with an amplitude of 0.3 kPa at a frequency of about 52 Hz.

Some researchers focused on the possibility of harvesting energy from the von Karman vortex street induced by circular cylinders. Akaydin et al. (148) investigated piezoaeroelastic energy harvesting from the turbulent boundary layers and wakes of circular cylinders at a high

Reynolds number. They developed a computational framework that couples the structural and electrical governing equations with a fluid-flow solver. Their numerically predicted open-circuit voltages are good agreement with their experimental data. They did not include any circuit optimization to enhance the level of the harvested power.

As a follow-up of their previous work, Akaydin et al. (149) investigated experimentally the concept of piezoelectric energy harvesting from a turbulent flow exhibiting a large degree of coherence in its spatial and temporal scales. They considered several orientations of a thin flexible cantilever beam consisting of a PVDF layer and a mylar substrate. They demonstrated that the best orientation is when the beam is parallel to the upstream flow. They reported that the level of generated voltage was maximized when the natural frequency of the piezoelectric generator is tuned to the vortex shedding frequency. They also showed that minor mismatching between these two frequencies resulted in substantial reductions in the level of the harvested power, especially when the shedding frequency is smaller than the natural frequency of the harvester. They indicated that the pressure on the beam was affected by different flow patterns associated with the induced flow ahead and behind the vortices and the low pressure vortex core region. They reported that the harvested energy was enhanced when these two mechanisms are combined with the resonance conditions of the beam. They also demonstrated that the distance between the beam and the cylinder is very important. In fact, the measurement showed that the maximum harvested power was about 4 μW when the distance between the beam and the cylinder is set equal to 2 D. They explained the fact that the maximum harvested power was not obtained near the cylinder because the large vortical structures are not fully formed at these locations.

Akaydin et al. (150) presented a piezoaeroelastic energy harvester consisting of a cantilevered aluminum shim covered by a piezoelectric material near its base, and a circular cylinder on its tip. Using a free-vibration wind-tunnel test, they showed that the increase in the electrical load resistance is accompanied with an increase in the global frequency of the harvester. They also demonstrated that there is an optimum value of the load resistance for which the electromechanical damping is maximized. They reported that the maximum harvested power was 0.1 mW for a wind speed of about 1.192 m/s. They also reported that the variations of the global resonant frequency and structural damping with the load

resistance are relatively small, but measurable.

Xie et al. (151) investigated theoretically power harvesting from a poled and electroded flexible ceramic cylinder. They developed a one-dimensional mathematical model to determine the harvested power and the efficiency of this harvester. They reported that, when the shedding frequency is near the lowest flexural resonant frequency of the cylinder, the harvested power can be the order of 1 mW for a cylinder 40 cm in length and 1 cm in diameter in air with a flow speed of 5 m/s.

Hobbs et al. (152; 153) investigated piezoelectric energy generation from multiple elastic cylinders arranged in a line (154; 155). They demonstrated that, when grouping the piezoelectric cylinders, the flow generated by upstream cylinders can significantly increase the level of the harvested power by the downstream cylinders. They also reported that the harvested power can be enhanced for a well-defined spacing distance between the cylinders, which is L/D=3.3. They also showed that there is an optimum value of the wind speed at which the level of the generated power can be enhanced. The highest power generation was determined for wind speeds associated with f_s/f_n=1.6, which is unusual because usually one expects a maximum value of the harvested power when the shedding frequency is near the natural frequency of the harvester.

High fidelity simulations of the VIV phenomenon are very expensive in terms of computing power and time. Such simulations can be significantly complicated if three-dimensional effects, turbulence structures, and elasticity are considered. Consequently, assumptions are often made to produce simple and accurate predictions of the VIV phenomenon and the structural response. Different models that are based on the van der Pol oscillator or its combination with other nonlinear oscillators have been proposed for VIV predictions. Nayfeh and his coauthors (156–160) used modern methods of nonlinear dynamics to identify the parameters of phenomenological models that could be used to represent the lift coefficient and drag on stationary and moving circular cylinders.

1.3.4 Other possible piezoaeroelastic energy harvesters

Another possible aeroelastic phenomenon is galloping, which is usually observed in high tension electric transmission lines. Den Hartog (105) studied and explained the galloping

phenomenon for the first time in 1943. He used the quasi-steady hypothesis to describe the aerodynamic forces. On a specified section that has a well-defined lift and drag coefficients, he developed a criterion for the galloping phenomenon to take place. Generally, galloping of elastic bluff bodies takes place when the wind speed exceeds a critical value at which an instability is initiated and the bluff body starts to oscillate. It is also well-known that the galloping phenomenon causes large-amplitude oscillations. This is beneficial when using piezoelectric transducers because the generated voltage is related to the amplitudes of these oscillations.

Many studies (161–172) have investigated the effects of various parameters on the behavior of galloping of different structures. These studies have also investigated the influence of the geometry of the structure cross-section on its oscillation amplitudes (173). Barrero-Gil et al. (174) investigated theoretically the possibility of using galloping to extract energy. They considered and discussed different geometries that can be used to harvest energy. Specific methods on how to harvest this energy were not discussed.

Sirohi and Mahadik (175) investigated theoretically and experimentally piezoaeroelastic energy harvesting from galloping beams with a D-shaped cross section. They showed that the power output increases rapidly with increasing the wind speed. They reported that a wind speed of 5.6 mph was required to harvest energy from this device. They also reported that the maximum harvested power was 1.14 mW at a wind speed of 10.5 mph. They reported good agreement between their analytical model and experimental data. They demonstrated that using a quasi-steady approximation was sufficient to model the fluid forces during galloping. As a follow-up to their previous work, Sirohi and Mahadik (176) presented the concept of energy harvesting from galloping based on an equilateral triangle section attached to cantilever beams with surface-bonded piezoelectric sheets. They developed a prototype device that generated more than 50 mW at a wind speed of 11.6 mph. They reported that this level of power is sufficient to supply most of the commercially available wireless sensors. They reported a discrepancy between their analytical model and experimental results, particularly in terms of the natural frequency and the harvested power.

1.4 Analysis: Model Reduction

The analysis of the simplest energy harvesters (e.g. cantilever beams) could involve a large number of degrees of freedom. Modeling aeroelastic energy harvesters requires the addition of complex dynamics and fluid-structure interactions. As such, high fidelity simulations of energy harvesters involve solving partial-differential equations and hence are very expensive in terms of computing power and time. Such simulations can be significantly complicated if three-dimensional effects, turbulence structure, and elasticity are considered. Using simulation tools, such as finite volume, finite element methods, and higher order finite differences is very powerful in terms of capturing the main physics features and yielding accurate results at few design points. However, such simulations cannot be used to optimize, control, quantify uncertainties, and sensitivities of their performance. Furthermore, they cannot be used to determine the most relevant aspects for the harvester's performance. These shortcomings lead to the need for developing distributed-parameter and phenomenological models that easily characterize the system's behavior. These simplified models can accurately predict the harvester's performance when the right assumptions are made. They would also be used to determine the important underlying physics of the harvesters.

In this work, we derive global nonlinear distributed-parameter models for different types of nonlinear piezoelectric energy harvesters. The methods of multiple scales is then used to study the effects of the nonlinear piezoelectric coefficients, the quadratic damping, and the excitation amplitude on the performance of the piezoelectric energy harvester and to characterize the nonlinear response of the harvester near resonance in terms of softening and hardening behaviors.

Concerning wing-based piezoaeroelastic energy harvesters, we perform linear analysis to predict the flutter speed of a wing and subsequent limit-cycle oscillations. The quasi-steady approximation is then used to determine the aerodynamic loads. We also use the Center-Manifold theorem to derive the normal form of Hopf bifurcation (flutter onset) for these harvesters. The advantages of using these tools in the design and performance improvement of these harvesters are detailed.

We also consider cylinder-based piezoaeroelastic energy harvesters. A phenomenological

model based on a modified van der pol equation is used to represent the fluctuating lift for an oscillating circular cylinder. This model is then coupled with the cylinder's oscillations and Gauss law to determine the harvested power. The advantages of using this coupled model to determine nonlinear aspects of the performance of the harvesters and their effects on the synchronization region are discussed.

All presented methodologies are used to investigate the performance of the energy harvester, perform sensitivity analysis or determine the optimized configuration to harvest more energy. In addition, these models allow for the implementation of linear and nonlinear controllers to enhance the level of the harvested power and avoid subcritical instability.

1.5 Approaches and Tools

Because different types of piezoelectric energy harvesters are investigated, we derive many representative models to predict their responses and performances. In Figure 1.3, we summarize the approaches and tools used in this Dissertation. For harvesting energy from ambient vibrations, the harvester is usually subjected to random excitations with different dominant frequencies. These multifrequency excitations have different amplitudes and various directions. Consequently, the energy harvester can be directly excited (i.e., excited in a direction perpendicular to the beam length) or parametrically excited (i.e. excited in a direction parallel to the beam length). For the case of wing-based piezoaeroelastic energy harvesters, different representations can be used to model the aerodynamic loads, such as the quasi-steady approximation, an unsteady representation based on the Duhamel formulation, and the unsteady vortex-lattice method (UVLM). Concerning the case of cylinder-based piezoaeroelastic energy harvesters, we model the aerodynamic loads by using a phenomenological model or computational fluid dynamics codes based on the Navier-Stokes equations.

We investigate the linear and nonlinear behaviors of vibration-based energy harvesters with a focus on the global coupling between (a) the mechanical and electrical parts in the case of harvesting energy from ambient vibrations, and (b) the mechanical, electrical, and aerodynamic parts in the case of harvesting energy form aeroelastic vibrations. Depending on the type of the excitation, the linear global coupled analysis takes into consideration

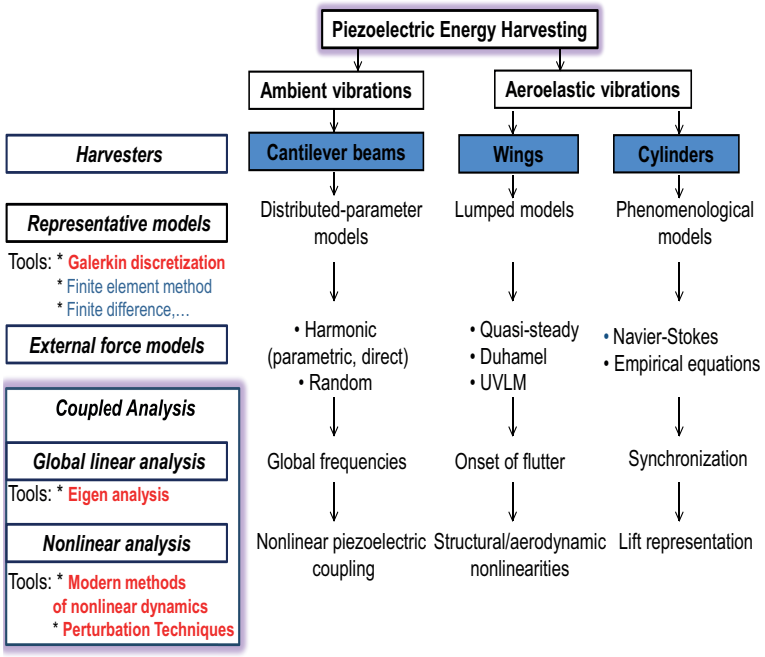

Figure 1.3: A descriptive schematic of the used approaches.

the effects of the electrical part on the natural frequency, flutter speed, or synchronization region of the harvester. In the nonlinear global coupled analysis, we focus on the effects of the nonlinear piezoelectric coupling on the behavior of energy harvesters from direct or parametric excitations. In the case of wing-based piezoaeroelastic energy harvesters, we focus on the effect of the structural and aerodynamic nonlinearities on the performance of the harvester in terms of type of instability (supercritical or subcritical) and enhancing the level of the harvested power. The Center-Manifold theorem is used to derive the normal form of the Hopf bifurcation. For cylinder-based piezoaeroelastic energy harvesters, we investigate the effect of the load resistance on the level of harvested power and the nonlinear behavior of the harvester (hardening or softening) by using a phenomenological model for the lift coefficient.

1.6 Layout of the Dissertation

This work consists of three major parts divided into seven chapters in which we focus on the modeling, analysis, and design of piezoelectric energy harvesters from ambient and aeroelastic vibrations using different methodologies and techniques to simulate and capture relevant physics and system's behavior at reduced computational costs.

The first part consists of two chapters. In this part, global nonlinear distributed-parameter models for piezoelectric energy harvesters under direct and parametric excitations are developed. The harvester consists of a unimorph piezoelectric cantilever beam with a tip mass. The representative models account for geometric, inertia, piezoelectric, and fluid drag nonlinearities. We develop reduced-order models by using the Euler-Lagrange equations and the Gauss law and implementing a Galerkin discretization. We then use the method of multiple scales to derive analytical expressions for the tip deflection, output voltage, and harvested power near the first principal resonance. The effects of the nonlinear piezoelectric coefficients, the quadratic damping, and the excitation amplitude on the output voltage and harvested electrical power are quantified.

The second part consists of four chapters. In this part, we focus on the modeling, design, and enhancement of wing-based piezoelectric energy harvesters from aeroelastic vibrations. In Chapter 4, we investigate the influence of linear and nonlinear parameters on the dynamic behavior of a wing-based piezoaeroelastic energy harvester. The system is composed of a rigid airfoil that is constrained to pitch and plunge and supported by linear and nonlinear torsional and flexural springs with a piezoelectric coupling attached to the plunge degree of freedom. A linear analysis is performed to determine the effects of the electrical load resistance and the linear spring coefficients on the flutter speed. Then, the normal form of the Hopf bifurcation is derived to determine the effects of the aerodynamic nonlinearities and the nonlinear plunge and pitch spring coefficients on the system's stability near the bifurcation. This is useful for characterizing the effects of different parameters on the system's output and ensure that the subcritical or "catastrophic" bifurcation does not take place.

In Chapter 5, we design a piezoaeroelastic energy harvester. We design the linear springs to produce the minimum flutter speed and,then, implement a linear velocity feedback to

reduce the flutter speed to any desired value and hence produce limit-cycle oscillations at low wind speeds. Then, we use the Center-Manifold theorem to derive the normal form of the Hopf bifurcation near the flutter onset, which, in turn, is used to choose nonlinear spring coefficients that produce supercritical bifurcations and increase the amplitudes of the ensuing limit cycles and hence the harvested power. We also investigate numerically variations of the system's outputs when increasing the freestream velocity and determine the effects of the appearance of the secondary Hopf bifurcations on the level of the harvested power.

In Chapter 6, we investigate the possibility of enhancing the level of the harvested power. Particularly, we determine the effects of varying the eccentricity between the gravity axis and the elastic axis on the flutter speed and harvested power. A linear analysis is performed to determine the impact of the eccentricity on the linear flutter speed. We evaluate two configurations in terms of the power generated from limit-cycle oscillations and a range of operating wind speeds. The nonlinear normal form is used to determine the critical values of the nonlinear torsional and flexural springs that yield supercritical Hopf bifurcation. The effects of varying the eccentricity on the level of the harvested power and pitch angle are also determined.

In Chapter 7, a stochastic approach is presented to evaluate the performance uncertainties that are associated with variations in the design parameters of the wing-based energy harvester. The sensitivities of the harvested power to variations in the load resistance, the eccentricity (distance between the center of mass and the elastic axis), and the nonlinear coefficients are determined. As a first step, we use the normal form of the Hopf bifurcation to determine the type of instability and select nonlinear coefficients of the springs that produce supercritical Hopf bifurcations. Moreover, the non-intrusive formulation of the Polynomial Chaos Expansion (PCE) in terms of the multivariate Hermite polynomials, is employed to quantify the sensitivities of the harvested power and the plunge and pitch motions to variations in the system's parameters.

In the third part, the concept of harvesting energy from vortex-induced vibrations of a circular cylinder is investigated. The power levels that can be generated from these vibrations and the variations of these levels with the freestream velocity are determined. A mathematical model that accounts for the coupled lift force, cylinder motion, and generated voltage is

presented. Linear analysis of the electromechanical model is performed to determine the effects of the electrical load resistance on the natural frequency of the rigid cylinder and the onset of the synchronization region for energy harvesting. The impacts of the nonlinearities on the cylinder's response and energy harvesting are investigated. The effects of the load resistance on the short- and open-circuit configurations are also discussed.

Part I

Global Nonlinear Piezoelectric Energy Harvesters from Base Excitations

Chapter 2

Global Nonlinear Distributed-Parameter Model of Piezoelectric Energy Harvesters under Direct Excitations

A common configuration of piezoelectric energy harvesters under base excitations is a cantilever beam with one or two piezoelectric layers and a tip mass. Various mathematical models have been proposed for cantilever beam energy harvesters (3; 19; 21; 177), including lumped and distributed-parameter models. Although the piezoelectric constitutive equations are nonlinear, most of the analyses are based on the linearized form of these equations (24; 177–179). Furthermore, in most of these studies (28; 50; 68; 180), only one mode approximation in the Galerkin discretization was considered, even in the presence of quadratic and cubic nonlinearities.

The aim of this chapter is to develop a global nonlinear analysis of an energy harvester consisting of a multi-layered cantilever beam with a tip mass. All nonlinearities (geometric, inertia, piezoelectric) are taken into account. A general Galerkin discretization is used to determine the number of modes required for accurate analysis of the system behavior. Based on the Lagrangian principle and Gauss law, we derive a reduced-order model of the harvester.

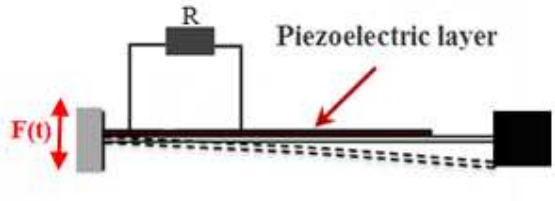

Figure 2.1: Schematic of an energy harvester under direct excitation.

The method of multiple scales is used to determine analytical expressions for the tip deflection, output voltage, and harvested power near the first global natural frequency. We use these expressions to investigate the effects of the nonlinear piezoelectric coupling on the behavior of the harvester and the level of the harvested power.

2.1 System Modeling and Reduced-Order Model

The energy harvester shown in Figure 2.1 is a cantilever beam with a tip mass excited by the supporting base. The beam is composed of brass and piezoelectric layers. The piezoelectric layer is bounded by two in-plane electrodes of negligible thickness connected to a load resistance R. The clamped end of the beam is subjected to a transverse harmonic displacement $Y(t) = Y_0 \cos(\Omega t)$. The geometric and physical properties of the harvester are given in Table 2.1.

We assume that the thickness of the beam is small compared to its length so that the shear deformation and rotary inertia can be neglected. Moreover, we assume that the damping is composed of linear viscous and quadratic terms. We model the beam as an Euler-Bernoulli beam of length L, width b, and height h, which comprises the thickness h_b of the brass layer and the thickness h_p of the piezoelectric layer. We let $u(x,t)$ and $v(x,t)$ be the components of the local displacement vector along the x- and y-axes, respectively, and assume that the beam is inextensional; that is, the axial strain $e = 0$. Because the axial strain of a differential element is given by (181)

Table 2.1: Physical and geometric properties of the unimorph cantilever beam

E_b	Brass Young's modulus (N/m^2)	105×10^9
E_p	Piezo Young's modulus (N/m^2)	66×10^9
ρ_b	Brass density (kg/m^3)	9000
ρ_p	Piezo density (kg/m^3)	7800
L	Length of the beam (mm)	50.8
b	Width of the beam (mm)	31.8
h_b	Brass layer thickness (mm)	0.14
h_p	Piezo layer thickness (mm)	0.26
M	Tip mass (g)	12
e_{31}	Piezoelectric coupling coefficient (C/m^2)	-12.54
$\in_{33}^s$	Piezoelectric permittivity (F/m)	1.328×10^{-8}

$$e = \sqrt{(1+u'^2)+v'^2} - 1 \tag{2.1}$$

hence

$$u' = -\frac{1}{2}v'^2 \text{ and } u = -\frac{1}{2}\int_0^s v'^2 ds \tag{2.2}$$

Moreover, we account for the geometric nonlinearities by using the following local strain measure (181):

$$\varepsilon_{11} = -y\left(v'' + \frac{1}{2}v''v'^2\right) \tag{2.3}$$

We develop a reduced–order model of the system by applying the Galerkin procedure to the Lagrangian and the Gauss law. To this end, we first calculate the kinetic energy T and potential energy Π. The kinetic energy of the harvester is the sum of the kinetic energies of the beam and tip mass, which are expressed as

$$T = \tfrac{1}{2}\int_0^L m(\dot{u}^2 + \dot{v}^2)dx + \tfrac{1}{2}M(\dot{u_L}^2 + \dot{v_L}^2) + \tfrac{1}{2}I_1\dot{v'_L}^2 \tag{2.4}$$

where the subscript L denotes variables evaluated at $x = L$, m is the mass per unit length for the bi-layered region, and I_1 is the rotary inertia of the tip mass M. The variation of the

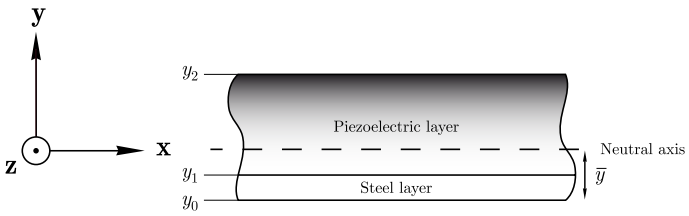

Figure 2.2: Neutral axis position.

total potential energy Π of the steel and piezoelectric layers is expressed as (181)

$$\delta\Pi \quad = \int_0^L \int_A \sigma_{11}^s \delta\varepsilon_{11} dA dx + \int_0^L \int_A \sigma_{11}^p \delta\varepsilon_{11} dA dx \tag{2.5}$$

where dA is the cross-section area of a differential beam element.

The strains and stresses in the steel and piezoelectric layers are, respectively, related by

$$\sigma_{11}^s = E_s \varepsilon_{11} \text{ and } \sigma_{11}^p = E_p \varepsilon_{11} - e_{31} E_2 + \tfrac{1}{2}\alpha_1 \varepsilon_{11}^2 + \tfrac{1}{2}\alpha_2 {E_2}^2 - \alpha_3 E_2 \varepsilon_{11} \tag{2.6}$$

where E_s and E_p are Young's moduli at constant electric field, the α_i are the nonlinear piezoelectric coefficients determined based on the Gibbs function (182–185), $E_2(t) = -\frac{V(t)}{h_p}$ is the electric field in the poling direction, and $V(t)$ is the potential of the upper electrode and thus represents the voltage between the piezoelectric electrodes. Using these expressions, we write the potential energy Π of the system as

$$\begin{aligned}\Pi = {} & \tfrac{1}{2}\int_0^L \Big[E y_3 (v''^2 + v'^2 v''^2) - e_{31} b (y_1 + y_2)(v'' + \tfrac{1}{2} v'^2 v'') V(t) - \tfrac{\alpha_1 b (y_2^4 - y_1^4)}{12} v''^3 \Big] dx \\ & + \tfrac{1}{2}\int_0^L \Big[- \tfrac{\alpha_2 b (y_2^2 - y_1^2)}{2 h_p^2} (v'' + \tfrac{1}{2} v'^2 v'') V^2(t) + \tfrac{\alpha_3 b (y_2^3 - y_1^3)}{3 h_p} (v''^2 + v'^2 v''^2) V(t) \Big] dx \end{aligned} \tag{2.7}$$

where

$$E_{y_3} = \frac{1}{3} E_s b \left(y_1^3 - y_0^3 \right) + \frac{1}{3} E_p b \left(y_2^3 - y_1^3 \right)$$

The positions of the layers are defined in Figure 2.2; they are given with respect to the position of the neutral axis $\bar{y} = \frac{(h_p + h_b) E_p h_p}{2(E_p h_p + E_s h_b)} + \frac{1}{2} h_b$ as:

$$y_0 = -\bar{y} \ , \ y_1 = h_b - \bar{y} \ , \ y_2 = (h_b + h_p) - \bar{y}$$

To complete the problem formulation, we relate the mechanical and electrical variables by using the Gauss law (186)

$$\frac{d}{dt} \int_A \mathbf{D}.\mathbf{n} \, dA = \frac{d}{dt} \int_A D_2 \, dA = \frac{V}{R} \tag{2.8}$$

where **D** is the electric displacement vector and **n** is the normal vector to the plane of the beam. Including the nonlinear piezoelectric contribution, one finds that D_2 is given by the following relation (182; 183):

$$D_2 = e_{31}\varepsilon_{11} + \in_{33}^{s} E_2 + \frac{1}{2}\alpha_3\varepsilon_{11}^2 + \frac{1}{2}\alpha_4 E_2^2 - \alpha_2 E_2\varepsilon_{11} \tag{2.9}$$

where e_{13} is the piezoelectric stress coefficient and $\in_{33}^{s}$ is the permittivity at constant strain. Substituting for ε_{11} from equation (2.3) into equation (2.9) yields

$$D_2 = -e_{31}y(v'' + \frac{1}{2}v''v'^2) + \in_{33}^{s} E_2 + \frac{1}{2}\alpha_3 y^2 v''^2 + \frac{1}{2}\alpha_4 E_2^2 + \alpha_2 E_2 y(v'' + \frac{1}{2}v''v'^2) \tag{2.10}$$

Substituting equation (2.10) into equation (2.8), we obtain

$$-e_{31}bh_p\int_0^L \left[\dot{v}'' + \tfrac{1}{2}\dot{v}''v'^2 + v''v'\dot{v}'\right]dx - \frac{\in_{33}^{s} bL}{h_p}\dot{V} + \alpha_3(y_2^2 - y_1^2)b\int_0^L v''\dot{v}''dx \tag{2.11}$$
$$+\frac{\alpha_4 bL}{h_p^2}V\dot{V} - \alpha_2 b\int_0^L (v'' + \tfrac{1}{2}v''v'^2)dx\dot{V} - \alpha_2 b\int_0^L \left[\dot{v}'' + \tfrac{1}{2}\dot{v}''v'^2 + v''v'\dot{v}'\right]dxV = \frac{V}{R}$$

To develop a reduced–order model of the harvester, we use the Galerkin procedure. For systems that possess quadratic and cubic nonlinearities, one term is not sufficient (187–191). Therefore, we express the displacement $v(x,t)$ in the form

$$v(x,t) = \sum_{i=1}^{n} \phi_i(x)q_i(t) \tag{2.12}$$

where the $\phi_i(x)$ are the mode shapes of a cantilever beam with a tip mass and the $q_i(t)$ are modal coordinates. The mode shapes are solutions of the following problem:

$$E_{y_3}v^{iv} + m\ddot{v} = 0 \tag{2.13}$$

$$v = 0 \text{ and } v' = 0 \text{ at } y = 0 \tag{2.14}$$

$$E_{y_3}v'' + I_1\ddot{v}' = 0 \text{ at } y = L \tag{2.15}$$

$$E_{y_3}v''' - M\ddot{v} = 0 \text{ at } y = L \tag{2.16}$$

To reduce the algebra, we perform the discretization by substituting equation (2.12) into equations (2.4), (2.7), and (2.11). Using the Lagrangian $\ell = T - \Pi$ of the system, carrying out the spatial integration, and using the extended Hamilton principle

$$\frac{d}{dt}\frac{\partial \ell}{\partial \dot{q}_i} - \frac{\partial \ell}{\partial q_i} = 0\ ,\ i = 1, 2, \cdots, n \tag{2.17}$$

up to cubic terms, we obtain the reduced-order model

$$\sum_{j=1}^{n} M_{ij}\ddot{q}_j + \sum_{j=1}^{n} B_{ij}q_j - \lambda_i V(t) - \sum_{j,k=1}^{n} D_{ijk}q_j q_k + \sum_{j,k,l=1}^{n} E_{ijkl}q_j q_k q_l - \theta_i V^2(t)$$
$$+ \sum_{j,k,l=1}^{n} F_{ijkl}(q_j q_k \ddot{q}_l + q_j \dot{q}_k \dot{q}_l) - \sum_{j,k=1}^{n} K_{ijk}q_j q_k V(t) + \sum_{j=1}^{n} N_{ij}q_j V(t) = \Omega^2 Y_0 \tilde{\Lambda}_i \cos(\Omega t) \tag{2.18}$$

and

$$\sum_{i=1}^{n} \chi_i \dot{q}_i + \sum_{i,j,k=1}^{n} L_{ijk}q_i q_j \dot{q}_k + \frac{\in_{33}^{s} bL}{h_p}\dot{V}(t) - \sum_{i,j=1}^{n} U_{ij}q_i \dot{q}_j - \frac{\alpha_4 bL}{h_p^2}V(t)\dot{V}(t) + \sum_{i=1}^{n} k_i q_i \dot{V}(t)$$
$$+ \sum_{i=1}^{n} \sigma_i \dot{q}_i V(t) + \frac{V}{R} = 0 \tag{2.19}$$

where

$$
\begin{aligned}
M_{ij} &= m\int_0^L \phi_i(x)\phi_j(x)dx + M\phi_i(L)\phi_j(L) + I_1\phi_i'(L)\phi_j'(L)\\
B_{ij} &= E_{y_3}\int_0^L \phi_i''(x)\phi_j''(x)dx\\
\lambda_i &= \tfrac{1}{2}\beta_1\phi_i'(L)\\
D_{ijk} &= \tfrac{3}{2}\beta_2\int_0^L \phi_i''(x)\phi_j''(x)\phi_k''(x)dx\\
E_{ijkl} &= E_{y_3}\int_0^L (\phi_i''(x)\phi_j''(x)\phi_k'(x)\phi_l'(x) + \phi_i'(x)\phi_j'(x)\phi_k''(x)\phi_l''(x))dx\\
F_{ijkl} &= m\int_0^L (\int_0^x \phi_i'\phi_j'ds)(\int_0^x \phi_k'\phi_l'ds)dx + M(\int_0^L \phi_i'\phi_j'dx)(\int_0^L \phi_k'\phi_l'dx)\\
K_{ijk} &= \tfrac{1}{4}\beta_1\int_0^L (\phi_i'(x)\phi_j'(x)\phi_k''(x) + \phi_i'(x)\phi_j''(x)\phi_k'(x) + \phi_i''(x)\phi_j'(x)\phi_k'(x))dx\\
\theta_i &= \tfrac{1}{2}\beta_3\phi_i'(L)\\
N_{ij} &= \beta_4\int_0^L \phi_i''(x)\phi_j''(x)dx\\
\chi_i &= e_{31}bh_p\phi_i'(L)\\
L_{ijk} &= e_{31}bh_p\int_0^L (\tfrac{1}{2}\phi_i'(x)\phi_j'(x)\phi_k''(x) + \phi_i'(x)\phi_j''(x)\phi_k'(x))dx\\
U_{ij} &= b\alpha_3(y_2^2 - y_1^2)\int_0^L \phi_i''(x)\phi_j''(x)dx\\
k_i &= b\alpha_2\phi_i'(L)\\
\tilde{\Lambda}_i &= m\int_0^L \phi_i(x)dx + M\phi_i(L)\\
\sigma_i &= b\alpha_2\phi_i'(L)
\end{aligned}
$$

where

$$\beta_1 = e_{31}b(y_1 + y_2) \tag{2.20}$$

$$\beta_2 = \frac{1}{12}b\alpha_1(y_2^4 - y_1^4) \tag{2.21}$$

$$\beta_3 = \frac{1}{2}\frac{b\alpha_2(y_1 + y_2)}{h_p} \tag{2.22}$$

$$\beta_4 = \frac{1}{3}\frac{b\alpha_3(y_2^3 - y_1^3)}{h_p} \tag{2.23}$$

2.1.1 Discretized equations

To reduce and simplify the problem, we keep three terms in the discretization (i.e., $n = 3$) and define the state variables

$$\mathbf{X} = \begin{bmatrix} X_1 \\ X_2 \\ X_3 \\ X_4 \\ X_5 \\ X_6 \\ X_7 \end{bmatrix} = \begin{bmatrix} q_1 \\ \dot{q}_1 \\ q_2 \\ \dot{q}_2 \\ q_3 \\ \dot{q}_3 \\ V \end{bmatrix} \tag{2.24}$$

In terms of these state variables, we express the reduced-order model as

$$\dot{\mathbf{X}} = B\mathbf{X} + F\cos(\Omega t)\tilde{\Lambda} + \tilde{\mathbf{N}}(\mathbf{X}) \tag{2.25}$$

where F=$\Omega^2 Y_0$,

$$B = \begin{bmatrix} 0 & 1 & 0 & 0 & 0 & 0 & 0 \\ -\tilde{\omega}_1^2 & 0 & 0 & 0 & 0 & 0 & \frac{\lambda_1}{M_{11}} \\ 0 & 0 & 0 & 1 & 0 & 0 & 0 \\ 0 & 0 & -\tilde{\omega}_2^2 & 0 & 0 & 0 & \frac{\lambda_2}{M_{22}} \\ 0 & 0 & 0 & 0 & 0 & 1 & 0 \\ 0 & 0 & 0 & 0 & -\tilde{\omega}_3^2 & 0 & \frac{\lambda_3}{M_{33}} \\ 0 & -\frac{\chi_1}{C_p} & 0 & -\frac{\chi_2}{C_p} & 0 & -\frac{\chi_3}{C_p} & -\frac{1}{RC_p} \end{bmatrix}$$

$$\tilde{\Lambda} = \begin{bmatrix} 0 \\ \tilde{\Lambda}_1 \\ 0 \\ \tilde{\Lambda}_2 \\ 0 \\ \tilde{\Lambda}_3 \\ 0 \end{bmatrix} \text{ and } \tilde{\mathbf{N}} = \begin{bmatrix} 0 \\ \tilde{N}_2 \\ 0 \\ \tilde{N}_4 \\ 0 \\ \tilde{N}_6 \\ \tilde{N}_7 \end{bmatrix}$$

Here, the $\tilde{\omega}_i$ are the structural natural frequencies and the $\tilde{N}_i$ are nonlinear functions of the X_i.

Letting G be the matrix whose columns are the eigenvectors of the matrix B corresponding to its eigenvalues $\pm j\omega_1 - \mu_1$, $\pm j\omega_2 - \mu_2$, $\pm j\omega_3 - \mu_3$, and $-\mu_7$, we define a new vector $\mathbf{Y}$ such that $\mathbf{X} = G\mathbf{Y}$ and rewrite equation (2.25) as

$$G\dot{\mathbf{Y}} = BG\mathbf{Y} + F\tilde{\Lambda}\cos(\Omega t) + \tilde{\mathbf{N}}(G\mathbf{Y}) \tag{2.26}$$

Multiplying equation (2.26) from the left with the inverse G^{-1} of G, we obtain

$$\dot{\mathbf{Y}} = J\mathbf{Y} + F\Lambda\cos(\Omega t) + \mathbf{N}(\mathbf{Y}) \tag{2.27}$$

where $\Lambda = G^{-1}\tilde{\Lambda}$ and $J = G^{-1}BG$ is a diagonal matrix whose elements are the eigenvalues $\pm j\omega_1 - \mu_1$, $\pm j\omega_2 - \mu_2$, $\pm j\omega_3 - \mu_3$, and $-\mu_7$ of B. We note that $Y_2 = \overline{Y_1}$, $Y_4 = \overline{Y_3}$, and $Y_6 = \overline{Y_5}$ and hence equation (2.27) can be rewritten in component form as

$$\dot{Y}_1 = j\omega_1 Y_1 - \mu_1 Y_1 + F\Lambda_1\cos(\Omega t) + Q_1(\mathbf{Y},\mathbf{Y}) + C_1(\mathbf{Y},\mathbf{Y},\mathbf{Y}) \tag{2.28}$$

$$\dot{Y}_3 = j\omega_2 Y_3 - \mu_2 Y_3 + F\Lambda_3\cos(\Omega t) + Q_3(\mathbf{Y},\mathbf{Y}) + C_3(\mathbf{Y},\mathbf{Y},\mathbf{Y}) \tag{2.29}$$

$$\dot{Y}_5 = j\omega_3 Y_5 - \mu_3 Y_5 + F\Lambda_5\cos(\Omega t) + Q_5(\mathbf{Y},\mathbf{Y}) + C_5(\mathbf{Y},\mathbf{Y},\mathbf{Y}) \tag{2.30}$$

$$\dot{Y}_7 = -\mu_7 Y_7 + F\Lambda_7\cos(\Omega t) + Q_7(\mathbf{Y},\mathbf{Y}) + C_7(\mathbf{Y},\mathbf{Y},\mathbf{Y}) \tag{2.31}$$

where the $Q_i(\mathbf{Y},\mathbf{Y})$ are bilinear functions of the components of $\mathbf{Y}$; the $C_i(\mathbf{Y},\mathbf{Y},\mathbf{Y})$ are tri-linear functions of the components of $\mathbf{Y}$; the ω_i are, respectively, the first three global natural frequencies (i.e. taking into account the piezoelectric effect) and the μ_i are the damping coefficients due to the piezoelectric coupling and the electrical resistance.

2.2 Analysis

We use the method of multiple scales (192; 193) to obtain a second-order approximate solution of the system response to a primary resonance of the first global mode (i.e., $\Omega \approx \omega_1$). To this end, we introduce a nondimensional bookkeeping parameter ϵ and scale F as $\epsilon^2 F$, the Q_i as ϵQ_i, the C_i as $\epsilon^2 C_i$, and the damping coefficients μ_i as $\epsilon^2\mu_i$, except μ_7, which is scaled to be

$O(1)$. Furthermore, we expand the Y_i as

$$Y_1 = Y_{11}(T_0, T_1, T_2) + \epsilon Y_{12}(T_0, T_1, T_2) + \epsilon^2 Y_{13}(T_0, T_1, T_2) + O(\epsilon^3) \tag{2.32}$$

$$Y_3 = Y_{31}(T_0, T_1, T_2) + \epsilon Y_{32}(T_0, T_1, T_2) + \epsilon^2 Y_{33}(T_0, T_1, T_2) + O(\epsilon^3) \tag{2.33}$$

$$Y_5 = Y_{51}(T_0, T_1, T_2) + \epsilon Y_{52}(T_0, T_1, T_2) + \epsilon^2 Y_{53}(T_0, T_1, T_2) + O(\epsilon^3) \tag{2.34}$$

$$Y_7 = Y_{71}(T_0, T_1, T_2) + \epsilon Y_{72}(T_0, T_1, T_2) + \epsilon^2 Y_{73}(T_0, T_1, T_2) + O(\epsilon^3) \tag{2.35}$$

where $T_n = \epsilon^n t$. The time derivative can be expressed in terms of the T_i as

$$\frac{d}{dt} = \frac{\partial}{\partial T_0} + \epsilon \frac{\partial}{\partial T_1} + \epsilon^2 \frac{\partial}{\partial T_2} + ... = d_0 + \epsilon d_1 + \epsilon^2 d_2 + ... \tag{2.36}$$

We express the nearness of the excitation frequency to the frequency of the first global mode using the detuning parameter σ defined as

$$\Omega = \omega_1 + \epsilon^2 \sigma \tag{2.37}$$

Substituting equations (2.32)-(2.37) into equations (2.28)-(2.31), using the aforementioned scalings, and equating coefficients of like powers of ϵ, we obtain four equations for the Y_{mn}. In the absence of internal resonances involving the first mode, the Y_{m1} for $m \neq 1$ decay with time. Consequently, $Y_{m1} = 0$ for $m \neq 1$. Furthermore, there is no dependence on T_1 because secular terms appear at $O(\epsilon^2)$. Therefore, the equations at different orders reduce to

Order ϵ^0

$$d_0 Y_{11} = j\omega_1 Y_{11} \tag{2.38}$$

Order ϵ

$$d_0 Y_{12} = j\omega_1 Y_{12} + q_{11} Y_{11}^2 + q_{12} Y_{11} \overline{Y}_{11} + q_{13} \overline{Y}_{11}^2 \tag{2.39}$$

$$d_0 Y_{32} = j\omega_2 Y_{32} + q_{31} Y_{11}^2 + q_{32} Y_{11} \overline{Y}_{11} + q_{33} \overline{Y}_{11}^2 \tag{2.40}$$

$$d_0 Y_{52} = j\omega_3 Y_{52} + q_{51} Y_{11}^2 + q_{52} Y_{11} \overline{Y}_{11} + q_{53} \overline{Y}_{11}^2 \tag{2.41}$$

$$d_0 Y_{72} = -\mu_7 Y_{72} + q_{71} Y_{11}^2 + q_{72} Y_{11} \overline{Y}_{11} + q_{73} \overline{Y}_{11}^2 \tag{2.42}$$

Order ϵ^2

$$\begin{aligned} d_0 Y_{13} = j\omega_1 Y_{13} - d_2 Y_{11} - \mu_1 Y_{11} + 2q_{11} Y_{11} Y_{12} + q_{12} Y_{11} \overline{Y}_{12} \\ + q_{12} \overline{Y}_{11} Y_{12} + 2q_{13} \overline{Y}_{11} \overline{Y}_{12} + q_{14} Y_{11} Y_{32} + q_{15} \overline{Y}_{11} Y_{32} + q_{16} Y_{11} Y_{52} + q_{17} \overline{Y}_{11} Y_{52} \\ + q_{18} Y_{11} Y_{72} + q_{19} \overline{Y}_{11} Y_{72} + \tilde{q}_{14} Y_{11} \overline{Y}_{32} + \tilde{q}_{15} \overline{Y}_{11} \overline{Y}_{32} + \tilde{q}_{16} Y_{11} \overline{Y}_{52} \\ + \tilde{q}_{17} \overline{Y}_{11} \overline{Y}_{52} + c_{11} Y_{11}^3 + c_{12} Y_{11}^2 \overline{Y}_{11} + c_{13} Y_{11} \overline{Y}_{11}^2 \\ + c_{14} \overline{Y}_{11}^3 + F\Lambda_1 \cos(\Omega t) + NST \end{aligned} \tag{2.43}$$

where NST stands for terms that do not produce secular terms.

The solution of equation (2.38) can be expressed as

$$Y_{11} = A(T_2) e^{j\omega_1 T_0} \tag{2.44}$$

Substituting equation (2.44) into equations (2.39)-(2.42) and solving the resulting equations, we obtain

$$Y_{12} = \frac{-jq_{11}}{\omega_1} A^2 e^{2j\omega_1 T_0} + \frac{jq_{12}}{\omega_1} A\overline{A} + \frac{jq_{13}}{3\omega_1} \overline{A}^2 e^{-2j\omega_1 T_0} \tag{2.45}$$

$$Y_{32} = \frac{jq_{31}}{\omega_2 - 2\omega_1} A^2 e^{2j\omega_1 T_0} + \frac{jq_{32}}{\omega_2} A\overline{A} + \frac{jq_{33}}{\omega_2 + 2\omega_1} \overline{A}^2 e^{-2j\omega_1 T_0} \tag{2.46}$$

$$Y_{52} = \frac{jq_{51}}{\omega_3 - 2\omega_1} A^2 e^{2j\omega_1 T_0} + \frac{jq_{52}}{\omega_3} A\overline{A} + \frac{jq_{53}}{\omega_3 + 2\omega_1} \overline{A}^2 e^{-2j\omega_1 T_0} \tag{2.47}$$

$$Y_{72} = \frac{q_{71}}{2j\omega_1 + \mu_7} A^2 e^{2j\omega_1 T_0} + \frac{q_{72}}{\mu_7} A\overline{A} + \frac{q_{73}}{-2j\omega_1 + \mu_7} \overline{A}^2 e^{-2j\omega_1 T_0} \tag{2.48}$$

Substituting equations (2.37) and (2.44-2.48) into equation (2.43), and eliminating the terms that lead to secular terms, we obtain the complex-valued modulation equation

$$d_2 A = -\mu_1 A + \alpha_e A^2 \overline{A} + \frac{1}{2} F\Lambda_1 e^{j\sigma T_2} \tag{2.49}$$

where

$$\begin{aligned} \alpha_e = c_{12} + \frac{jq_{12}q_{11}}{\omega_1} - \frac{jq_{12}\overline{q}_{12}}{\omega_1} - \frac{2jq_{13}\overline{q}_{13}}{3\omega_1} + \frac{jq_{14}q_{32}}{\omega_2} + \frac{jq_{15}q_{31}}{\omega_2 - 2\omega_1} \\ + \frac{jq_{16}q_{52}}{\omega_3} + \frac{jq_{17}q_{51}}{\omega_3 - 2\omega_1} + \frac{q_{18}q_{72}}{\mu_7} + \frac{q_{19}q_{71}}{2j\omega_1 + \mu_7} - \frac{j\tilde{q}_{14}\overline{q}_{32}}{\omega_2} - \frac{j\tilde{q}_{15}\overline{q}_{33}}{\omega_2 + 2\omega_1} \\ - \frac{j\tilde{q}_{16}\overline{q}_{52}}{\omega_3} - \frac{j\tilde{q}_{17}\overline{q}_{53}}{\omega_3 + 2\omega_1} \end{aligned} \tag{2.50}$$

Writing A in the polar form $A = \frac{1}{2} a(T_2) e^{j\eta(T_2)}$, we rewrite equation (2.49) as

$$a' + aj\eta' = -\mu_1 a + \frac{1}{4} \alpha_e a^3 + F\Lambda_1 e^{j(\sigma T_2 - \eta)} \tag{2.51}$$

Separating the real and imaginary parts in equation (2.51) yields the real-valued modulation equations

$$a' = -\mu_1 a + \frac{1}{4} Re(\alpha_e) a^3 + F|\Lambda_1| \cos(\sigma T_2 + \theta_1 - \eta) \tag{2.52}$$

$$a\eta' = \frac{1}{4} Im(\alpha_e) a^3 + F|\Lambda_1| \sin(\sigma T_2 + \theta_1 - \eta) \tag{2.53}$$

where $\theta_1 = \arctan(\frac{Im(\Lambda_1)}{Re(\Lambda_1)})$ and Re and Im stand for the real and imaginary parts, respectively. In equation (2.52), we adjust μ_1 to include all linear structural and electrical damping. These damping coefficients are usually estimated from experimental results.

The non-autonomous system of equations (2.52) and (2.53) can be transformed into an autonomous system by introducing the transformation

$$\beta = \sigma T_2 + \theta_1 - \eta \tag{2.54}$$

Then,

$$\eta = \sigma T_2 + \theta_1 - \beta \tag{2.55}$$

and

$$\eta' = \sigma - \beta' \tag{2.56}$$

Substituting equations (2.54-2.56) into equations (2.52) and (2.53), we obtain the autonomous system

$$a' = -\mu_1 a + \frac{1}{4} Re(\alpha_e) a^3 + \frac{1}{2} F|\Lambda_1| \cos\beta \tag{2.57}$$

$$a\beta' = \sigma a - \frac{1}{4} Im(\alpha_e) a^3 - \frac{1}{2} F|\Lambda_1| \sin\beta \tag{2.58}$$

Solving equations (2.57) and (2.58), we can determine the Y_{mn} and then determine expressions for the deflection, voltage, and harvested power. To determine the steady-state response, we set the time derivatives in equations (2.57) and (2.58) equal to zero. Then, squaring and adding the resulting equations yields the frequency-response equation

$$[\mu_1 - \frac{1}{4} Re(\alpha_e) a^2]^2 a^2 + [\sigma - \frac{1}{4} Im(\alpha_e) a^2]^2 a^2 = F^2 |\Lambda_1|^2 \tag{2.59}$$

Then, the phase can be expressed as

$$\tan\beta = \frac{4\sigma - Im(\alpha_e) a^2}{4\mu_1 - Re(\alpha_e) a^2} \tag{2.60}$$

Expressing A in the polar form and using equations (2.54-2.56), we rewrite equation (2.44) as

$$Y_{11} = \frac{1}{2} a e^{j(\Omega t + \theta_1 - \beta)} \tag{2.61}$$

Then,

$$Y_1 = \frac{1}{2} a e^{j(\Omega t + \theta_1 - \beta)} - \frac{j q_{11}}{4\omega_1} a^2 e^{j(2\Omega t + 2\theta_1 - 2\beta)} + \frac{j q_{12}}{4\omega_1} a^2 + \frac{j q_{13}}{12\omega_1} a^2 e^{-j(2\Omega t + 2\theta_1 - 2\beta)} \tag{2.62}$$

$$Y_{32} = \frac{j q_{31}}{4(\omega_2 - 2\omega_1)} a^2 e^{j(2\Omega t + 2\theta_1 - 2\beta)} + \frac{j q_{32}}{4\omega_2} a^2 + \frac{j q_{33}}{4(\omega_2 + 2\omega_1)} a^2 e^{-j(2\Omega t + 2\theta_1 - 2\beta)} \tag{2.63}$$

$$Y_{52} = \frac{j q_{51}}{4(\omega_3 - 2\omega_1)} a^2 e^{j(2\Omega t + 2\theta_1 - 2\beta)} + \frac{j q_{52}}{4\omega_3} a^2 + \frac{j q_{53}}{4(\omega_3 + 2\omega_1)} a^2 e^{-j(2\Omega t + 2\theta_1 - 2\beta)} \tag{2.64}$$

$$Y_{72} = \frac{q_{71}}{4(2j\omega_1 + \mu_7)} a^2 e^{j(2\Omega t + 2\theta_1 - 2\beta)} + \frac{q_{72}}{4\mu_7} a^2 + \frac{q_{73}}{4(-2j\omega_1 + \mu_7)} a^2 e^{-j(2\Omega t + 2\theta_1 - 2\beta)} \tag{2.65}$$

Then, using the fact that $\mathbf{X} = G\mathbf{Y}$, we can easily determine analytical expressions for the displacement, voltage, and harvested power. Then, to the second approximation, the voltage can be expressed as

$$V(t) = X_7(t) = a|G_{71}| \cos(\Omega t + \gamma) + \Gamma_0 a^2 + \Gamma_2 a^2 \cos(2\Omega t + 2\gamma) \tag{2.66}$$

where γ, Γ_0, and Γ_2 are known functions of the harvester parameters. Hence, to the second approximation, the harvested power is given by

$$P = \frac{< V^2 >}{R} = \frac{a^2 |G_{71}|^2}{2R} \tag{2.67}$$

2.3 Restriction on the Nonlinear Piezoelectric Coefficients

For the free-vibration configuration ($F = 0N$), it follows from equations (2.57) and (2.58) that the steady-state response amplitude a is given by

$$(-\mu_1 + \frac{1}{4}Re(\alpha_e)a^2)a = 0 \tag{2.68}$$

Equation (2.68) has the following three equilibrium solutions:

$$a = 0 \text{ and } a = \pm\sqrt{\frac{4\mu_1}{Re(\alpha_e)}}$$

where $a = 0$ is the trivial solution. The other solutions are nontrivial. For this simple case in which the cantilever beam is not excited, the amplitude response must be zero. In other words, self-excited oscillations should not exist. Therefore, to obtain a physical response, the nontrivial solutions have to be complex-valued. Consequently, $Re(\alpha_e)$, which depends on the nonlinear piezoelectric coefficients and hence the piezoelectric material, must be negative.

The sign of the imaginary part $Im(\alpha_e)$ of the effective nonlinearity determines the softening/hardening behavior of this harvester. In fact, if $Im(\alpha_e) > 0$, the system has a hardening behavior. On the other hand, if $Im(\alpha_e) < 0$, the system has a softening behavior.

Guyomar et al. (183) identified the nonlinear piezoelectric coefficients of "hard" PZT (P189 from Quartz and Silice company) based on a mass-spring system. The identified properties are presented in Table 2.2 (183; 194; 195). In Table 2.3, we show the real and imaginary parts of the effective nonlinearity. We note that, for all considered number of modes in the approximation, the real and imaginary parts of the effective nonlinearity are always negative. These results are consistent with our analysis and indicate that the behavior of the system is softening.

Table 2.2: Properties of the P189 ceramic

E_p	93.8×10^9 (N/m^2)
ρ_p	7650 (kg/m^3)
e_{31}	-10.13 (C/m^2)
$\in_{33}^s$	9.08×10^{-9} (F/m)
α_1	-3.376×10^{13} Pa
α_2	6×10^{-5} $N.V^{-2}$
α_3	-2.8×10^4 $C.m^{-2}$
α_4	2.05×10^{-13} $C.V^{-2}$

Table 2.3: Real and imaginary parts of the effective nonlinearity

Number of modes	$Re(\alpha_e)$	$Im(\alpha_e)$
$n = 1$	-0.000418	-0.00331
$n = 2$	-0.000438	-0.00321
$n = 3$	-0.000441	-0.00320
$n = 4$	-0.000441	-0.00320

2.4 Results

To accurately predict the performance of this harvester in the presence of quadratic and cubic nonlinearities, we first investigate the required number of modes in the Galerkin approach. Then, we show the effects of the nonlinear piezoelectric coefficients (α_1, α_2, α_3, and α_4) and excitation amplitude F on the voltage output. Using a combination of the analytical solution and experiments, one can identify the nonlinear piezoelectric coefficients. In all of the results, we made sure that $Re(\alpha_e) < 0$. Moreover, in all of the following figures, solid lines indicate stable solutions and dashed lines indicate unstable solutions.

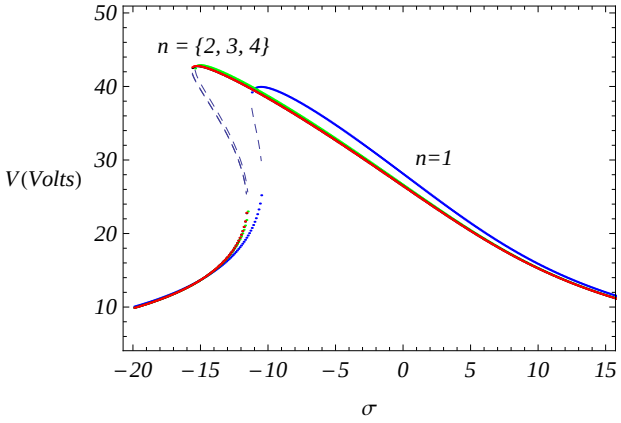

(a) $\alpha_1 = -5 \times 10^{14} Pa, \alpha_2 = \alpha_3 = \alpha_4 = 0$

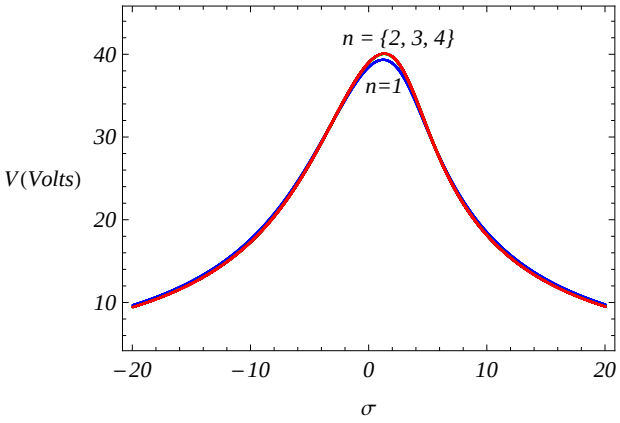

(b) $\alpha_3 = -10^5 C.m^{-2}, \alpha_1 = \alpha_2 = \alpha_4 = 0$

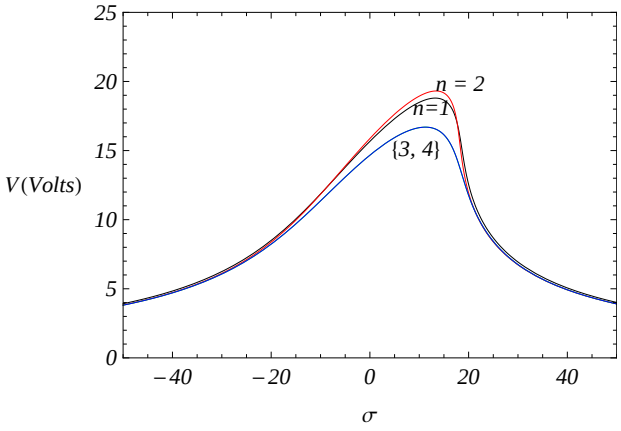

(c) $\alpha_1 = -5 \times 10^{14} Pa, \alpha_2 = 10^{-4} N.V^{-2}, \alpha_3 = -5 \times 10^5 C.m^{-2}, \alpha_4 = 0$

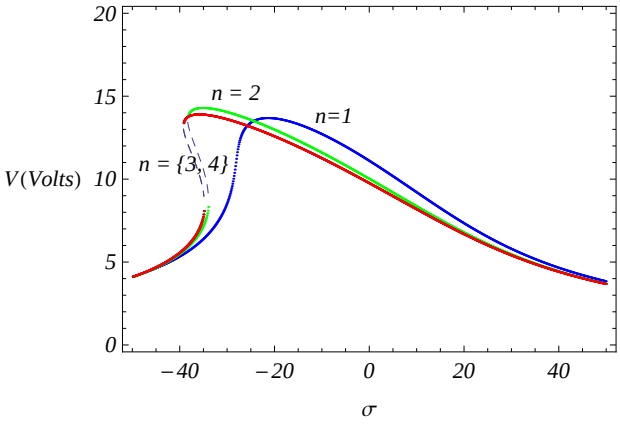

(d) $\alpha_1 = -3 \times 10^{15} Pa, \alpha_2 = 10^{-4} N.V^{-2}, \alpha_3 = -5 \times 10^5 C.m^{-2}, \alpha_4 = 2 \times 10^{-13} C.V^{-2}$

Figure 2.3: Variation of the voltage output with σ for different values of n when $R = 10^5 \Omega$ and $F = 2m/s^2$.

2.4.1 Required modes in the Galerkin discretization

Figures 2.2 (a-d) show the impact of varying the number of modes used in the Galerkin discretization by considering various configurations through changing the nonlinear piezoelectric coefficients and keeping the real part of the effective nonlinearity negative. Clearly, a one-mode approximation yields erroneous results for all configurations. The use of a one-mode approximation can lead to misleading conclusions, as shown in Figure 2.2-d; it does not predict multi-valued responses, unlike the two-, three-, and four-mode approximations. Moreover, two modes yield inaccurate generated voltage and hence energy, as shown in Figures 2.2-c and 2.2-d. Consequently, we use three modes in the approximation.

For the harvester under consideration, whose properties are shown in Table 2.1, the real and imaginary parts of the effective nonlinearity calculated using three modes are given by

$$\begin{aligned} Re(\alpha_e) = 1.6545\times10^{-6} - 1.3199\times10^{-33}\alpha_1^2 + 4.782\times10^{-15}\alpha_1\alpha_2 - 884394\alpha_2^2 \\ -9.549\times10^{-23}\alpha_1\alpha_3 + 0.000841\alpha_2\alpha_3 - 1.1283\times10^{-13}\alpha_3^2 + 0.000026\alpha_1\alpha_4 \\ +9.258\times10^{14}\alpha_2\alpha_4 - 438103\alpha_3\alpha_4 - 2.3037\times10^{23}\alpha_4^2 \end{aligned} \tag{2.69}$$

$$\begin{aligned} Im(\alpha_e) = 0.00001 - 1.3371\times10^{-31}\alpha_1^2 - 7.463\times10^{-15}\alpha_1\alpha_2 + 613361\alpha_2^2 \\ +2.3613\times10^{-22}\alpha_1\alpha_3 - 0.001\alpha_2\alpha_3 + 3.163\times10^{-13}\alpha_3^2 - 0.0000189\alpha_1\alpha_4 \\ -3.338\times10^{14}\alpha_2\alpha_4 + 354520\alpha_3\alpha_4 - 1.3622\times10^{21}\alpha_4^2 \end{aligned} \tag{2.70}$$

Inspecting the expression of $Re(\alpha_e)$, we note that it is mandatory to include the quadratic piezoelectric nonlinearities to obtain negative $Re(\alpha_e)$. Therefore, this study demonstrates that all nonlinearities should be taken into account.

2.4.2 Effect of the nonlinear piezoelectric coefficients on the system outputs

In this section, the effects of the nonlinear piezoelectric coefficients on the generated voltage is investigated by keeping the electrical load resistance and the excitation amplitude constants.

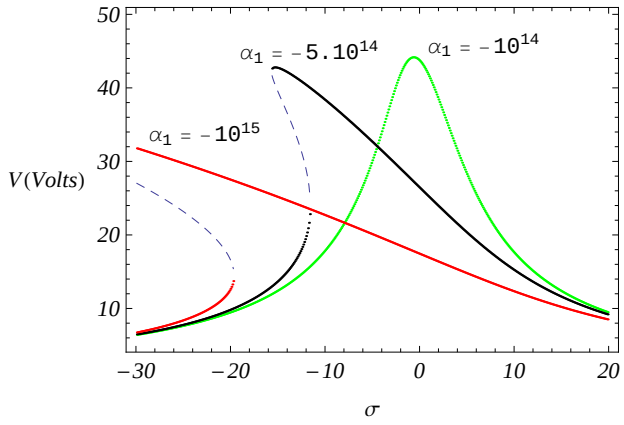

(a) $\alpha_2 = \alpha_3 = \alpha_4 = 0$

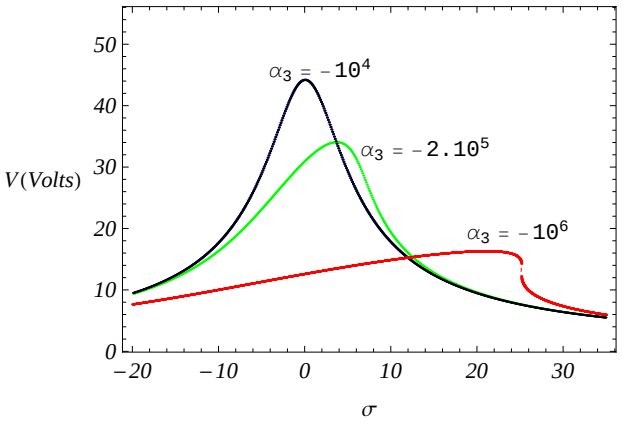

(b) $\alpha_1 = \alpha_2 = \alpha_4 = 0$

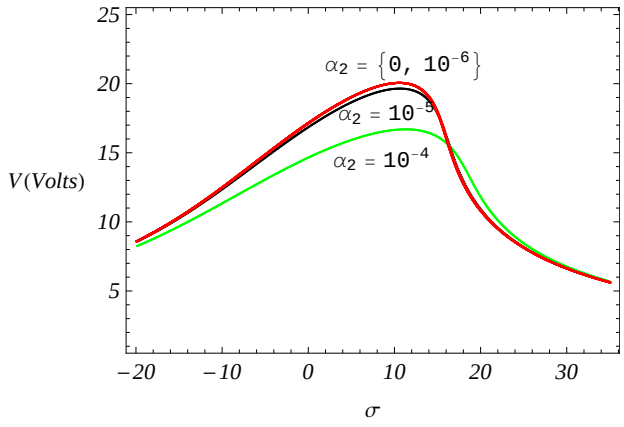

(c) $\alpha_1 = -5 \times 10^{14} Pa, \alpha_3 = -5 \times 10^5 C.m^{-2}, \alpha_4 = 0$

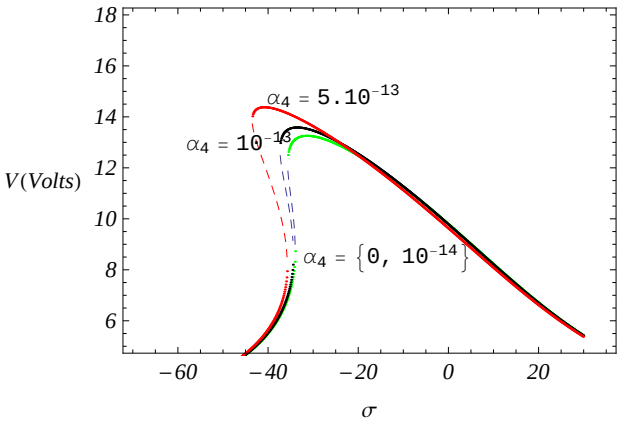

(d) $\alpha_1 = -3 \times 10^{15} Pa, \alpha_2 = 10^{-4} N.V^{-2}, \alpha_3 = -5 \times 10^5 C.m^{-2}$

Figure 2.4: Variation of the voltage output with the detuning σ for different configurations of nonlinear piezoelectric coefficients when $R = 10^5 \Omega$, $F = 2m/s^2$, $n = 3$.

Figure 2.3 (a-d) shows the influence of the nonlinear piezoelectric coefficients. Figure 2.3-a shows the influence of varying α_1 keeping the other coefficients zero. In this case,

$$Re(\alpha_e) = 1.6545 \times 10^{-6} - 1.3199 \times 10^{-33}\alpha_1^2$$

$$Im(\alpha_e) = 0.00001 - 1.3371 \times 10^{-31}\alpha_1^2$$

Hence, for negative $Re(\alpha_e)$, α_1 should be less than $-3.5404 \times 10^{13} Pa$. Clearly, the smaller the value of α_1 is, the larger $|Re(\alpha_e)|$ is, and hence the smaller the peak amplitude is. Furthermore, for these values, $Im(\alpha_e) < 0$. Furthermore, the smaller the value of α_1 is, the larger $|Im(\alpha_e)|$ is, and hence the softening behavior of the system is enhanced.

Figure 2.3-b shows the influence of varying α_3 keeping the other coefficients zero. In this case,

$$Re(\alpha_e) = 1.6545 \times 10^{-6} - 1.1283 \times 10^{-13}\alpha_3^2$$

$$Im(\alpha_e) = 0.00001 + 3.163 \times 10^{-13}\alpha_3^2$$

Hence, for negative $Re(\alpha_e)$, α_3 should be less than $-3.823 \times 10^3 C.m^{-2}$. Clearly, the smaller the value of α_3 is , the larger $|Re(\alpha_e)|$ is, and hence the smaller the peak amplitude is. Moreover, $Im(\alpha_e)$ is always positive and hence the system behavior is always hardening. Moreover, the smaller the value of α_3 is, the larger $Im(\alpha_e)$ is, and hence the hardening behavior of the system is enhanced.

Figure 2.3-c shows the influence of varying α_2 when $\alpha_1 = -5 \times 10^{14} Pa$, $\alpha_3 = -5 \times 10^5 C.m^{-2}$, and $\alpha_4 = 0$. In this case,

$$Re(\alpha_e) = -0.05249 - 423.156\alpha_2 - 884394\alpha_2^2$$

$$Im(\alpha_e) = 0.1045 + 507.537\alpha_2 + 613361\alpha_2^2$$

Hence, for negative $Re(\alpha_e)$, α_2 should be positive. Clearly, the larger the value of α_2 is, the larger $|Re(\alpha_e)|$ is, and hence the smaller the peak amplitude is. Moreover, $Im(\alpha_e)$ is always positive and hence the system behavior is always hardening. Furthermore, the larger the value of α_2 is, the larger $Im(\alpha_e)$ is, and hence the hardening behavior of the system is enhanced.

Figure 2.3-d shows the influence of varying α_4 when $\alpha_1 = -3\times10^{15}Pa$, $\alpha_2 = 10^{-4}N.V^{-2}$, and $\alpha_3 = -5\times10^{5}C.m^{-2}$. In this case,

$$Re(\alpha_e) = -0.2357 + 2.337\times10^{11}\alpha_4 - 2.303\times10^{23}\alpha_4^2$$

$$Im(\alpha_e) = -0.713 - 1.539\times10^{11}\alpha_4 - 1.362\times10^{23}\alpha_4^2$$

Hence, for negative $Re(\alpha_e)$, α_4 must be less than $5.072\times10^{-13}C.V^{-2}$. Clearly, the smaller the value of α_4 is, the larger $|Re(\alpha_e)|$ is, and hence the smaller the peak amplitude is. Moreover, $Im(\alpha_e)$ is always negative and hence the system behavior is always softening. Furthermore, the larger the value of α_4 is, the larger $Im(\alpha_e)$ is, and hence the softening behavior of the system is enhanced.

2.4.3 Impact of the excitation amplitude and frequency on the harvester

Unlike parametrically excited cantilever beams, which start to oscillate when the excitation amplitude exceeds a critical value, directly excited beams always oscillate even for small values of the excitation amplitude. Hence, direct excitations produce power for all excitation frequencies and amplitudes, as shown in Figures 2.4 and 2.5.

For a linear system, the frequency-response curves are symmetric and the variation of the generated voltage with the forcing excitation is linear for any considered detuning and hence frequency. Figure 2.4-a shows variation of the generated voltage with the detuning for various values of the excitation amplitude when the first nonlinear piezoelectric coefficient ($\alpha_1 = -5\times10^{14}Pa$) and the other coefficients are zero. In this case, the harvester behavior is softening. We note that increasing the excitation amplitude leads to a significant softening behavior and an increase in the voltage. Figure 2.4-b shows variation of the voltage output with the excitation amplitude for different values of the detuning. Clearly, the harvester exhibits multi-valued responses for negative detuning as a consequence of the nonlinearity being of the softening type.

In Figure 2.5, we show frequency-response and force-response curves generated when $\alpha_3 = -2\times10^{5}C.m^{-2}$ and the other coefficients are zero. In this case, the harvester has a hardening behavior. Figure 2.5-a shows that an increase in the excitation amplitude leads to

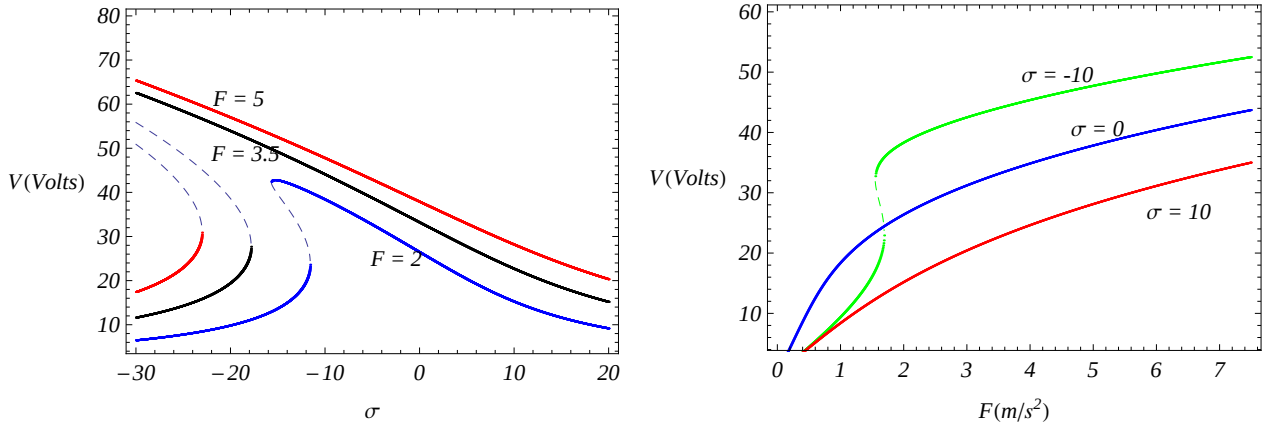

(a) (b)

Figure 2.5: Variation of the voltage output (a) with the detuning σ for different values of $F(m/s^2)$ and (b) with F for various values of the detuning σ when $R = 10^5\Omega$, $n = 3$, $\alpha_1 = -5 \times 10^{14} Pa$, and $\alpha_2 = \alpha_3 = \alpha_4 = 0$.

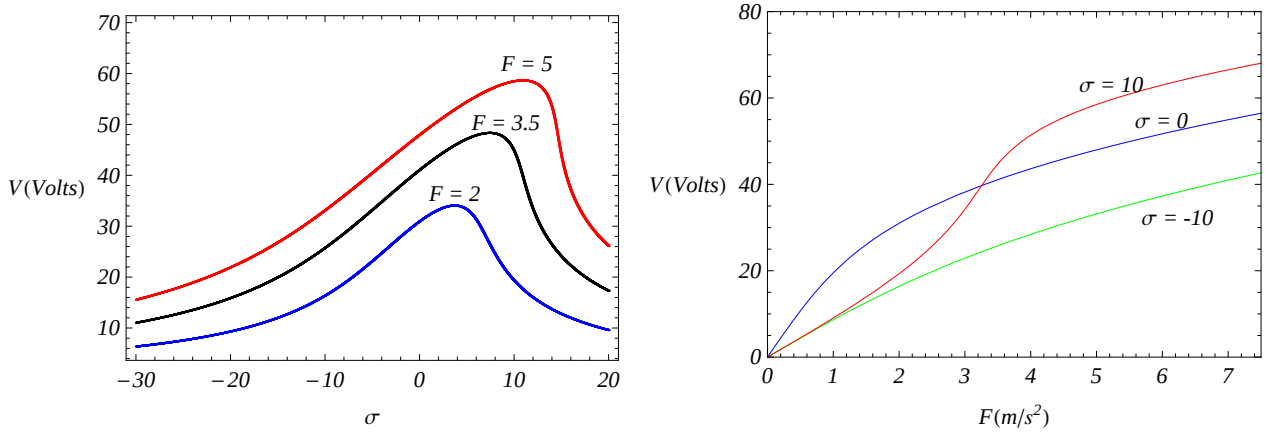

(a) (b)

Figure 2.6: Variation of the voltage output (a) with the detuning σ for different values of $F(m/s^2)$ and (b) with F for various values of the detuning σ when $R = 10^5\Omega$, $n = 3$, $\alpha_3 = -2 \times 10^5 C.m^{-2}$, and $\alpha_1 = \alpha_2 = \alpha_4 = 0$.

an increase in the generated voltage as well as an increase in the bending of the frequency-response curves to the right. Figure 2.5-b shows that the force-response is multi-valued for positive detuning and that the response is almost linear for large negative detuning.

2.5 Conclusions

A global nonlinear distributed-parameter model is presented for piezoelectric energy harvesting under direct excitation. The modeling of the cantilever beam is based on the nonlinear Euler-Bernoulli theory. Geometric, inertia, piezoelectric nonlinearities are accounted for in the analysis. A reduced-order model is derived based on the extended Hamilton principle and the Gauss law. The method of multiple scales is then used to derive analytical expressions for the steady-state beam deflection, output voltage, and harvested power near the first global resonance. The results show that one- or two-mode approximations in the Galerkin approach are not sufficient to accurately predict the performance of the harvester. Furthermore, the nonlinear piezoelectric coefficients have an important impact on the harvester behavior in terms of hardening or softening. Depending on the values of the second and fourth nonlinear piezoelectric coefficients, the generated voltage can be increased or decreased, unlike their effects on a parametrically excited cantilever beam. The choice of the nonlinear piezoelectric coefficients can lead to the appearance or disappearance of unstable branches. The excitation amplitude also affects very much the behavior of the system in terms of bending the frequency-response curves. These results show that a nonlinear distributed-parameter model, which includes as a minimum the first three modes, is required for the design of energy harvesting devices.

Chapter 3

Global Nonlinear Distributed-Parameter Model of Parametrically Excited Piezoelectric Energy Harvesters

Most of the energy harvesting studies have focused on directly excited piezoelectric energy harvesters. On the other hand, in practical situations where direct excitations are not feasible or may not be applicable, a different excitation phenomenon may provide a better option. Of particular interest is the principal parametric resonance (80; 181; 196–198) whereby the excitation frequency is near twice one of the natural frequencies of the system. In the literature of piezoelectric energy harvesting under parametric excitation, there is only one study (79) in which the dynamics of the system were investigated using a lumped-parameter model. The authors used only the first mode and did not account for piezoelectric effects on the beam response or for quadratic and cubic nonlinear piezoelectric coupling.

The aim of this chapter is to examine how oscillations produced by a principal parametric resonance can be exploited to harvest energy using a distributed-parameter model that accounts for linear and nonlinear piezoelectric effects. For that, we develop a global nonlinear distributed-parameter model for a piezoelectric energy harvester under parametric excita-

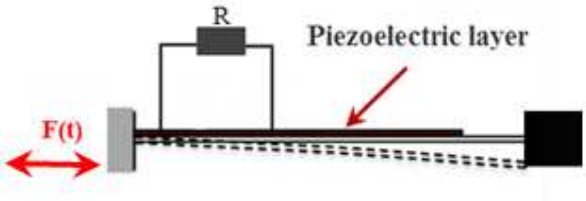

Figure 3.1: Schematic of a parametrically excited multi-layered cantilever beam with a tip mass used for energy harvesting.

tion. The harvester consists of a unimorph piezoelectric cantilever beam with a tip mass. The derived model accounts for geometric, inertia, piezoelectric, and fluid drag nonlinearities. A reduced-order model is derived by using the Euler-Lagrange principle and Gauss law and implementing a Galerkin discretization. The method of multiple scales is used to obtain analytical expressions for the tip deflection, output voltage, and harvested power near the first principal parametric resonance. The effects of the nonlinear piezoelectric coefficients, the quadratic damping, and the excitation amplitude on the output voltage and harvested electrical power are quantified.

3.1 Problem Formulation

We consider the problem of harvesting energy from a parametrically excited unimorph cantilever beam with a tip mass M. As shown in Figure 3.1, the beam is composed of steel and piezoelectric layers. The piezoelectric layer is bounded by two in-plane electrodes of negligible thickness connected to a load resistance R. The geometric and physical properties of the harvester are given in Table 3.1.

3.1.1 Governing equations

Including the geometric, inertia, and piezoelectric nonlinearities of the harvester as presented in Chapter 2, we model the beam as a nonlinear Euler-Bernoulli beam of length L, width b, and height h, which comprises the thickness of the steel layer h_s and the thickness of

Table 3.1: Physical and geometric properties of the unimorph cantilever beam

E_s	Steel Young's modulus (N/m^2)	193×10^9
E_p	Piezo Young's modulus (N/m^2)	66×10^9
ρ_s	Steel density (kg/m^3)	8027
ρ_p	Piezo density (kg/m^3)	7800
L	Length of the beam (mm)	304.8
b	Width of the beam (mm)	31.75
h_s	Steel layer thickness (mm)	0.51
h_p	Piezo layer thickness (mm)	0.3
M	Tip mass (g)	30.1
e_{31}	Piezoelectric coupling coefficient (C/m^2)	-12.54
$\in_{33}^s$	Piezoelectric permittivity (F/m)	1.328×10^{-8}

the piezoelectric layer h_p. In the previous chapter, we derived a global nonlinear distributed-parameter model of a directly excited cantilever beam based on a general form of the Galerkin discretization $v(x,t) = \sum_{i=1}^{n} \phi_i(x) q_i(t)$, where $v(x,t)$ is the local displacement along the y-axis, the $\phi_i(x)$ are the mode shapes of a cantilever beam with a tip mass, and the $q_i(t)$ are modal coordinates. In this chapter, we add the forcing term for a parametric excitation and eliminate the direct forcing term. Consequently, the effect of the virtual work W is added in the Lagrangian principle.

The virtual work is due to damping and the parametric excitation and its variation is expressed as (181; 197; 198)

$$\delta W = -\int_0^L m\Big([v''(x-L)+v']F\cos\Omega t + c_1\dot{v} + c_2\dot{v}|\dot{v}|\Big)\delta v dx + Mv'_L F\cos\Omega t \delta v_L \tag{3.1}$$

where Ω is the excitation frequency and F is the amplitude of the excitation acceleration. Because the damping coefficients are usually not known and are estimated by matching theoretical and experimental results, we account for the linear and nonlinear damping in the reduced–order model.

Using the Lagrangian $\ell = T - \Pi$ of the system, carrying out the spatial integration, and

using the extended Hamilton principle

$$\frac{d}{dt}\frac{\partial \ell}{\partial \dot{q}_i} - \frac{\partial \ell}{\partial q_i} = \frac{\delta W}{\delta q_i}\ , \ i = 1, 2, \cdots, n \tag{3.2}$$

up to cubic terms, we obtain the reduced-order model

$$\begin{aligned}\sum_{j=1}^{n} M_{ij}\ddot{q}_j + \sum_{j=1}^{n} B_{ij}q_j - \lambda_i V(t) - \sum_{j,k=1}^{n} D_{ijk}q_j q_k + \sum_{j,k,l=1}^{n} E_{ijkl}q_j q_k q_l - \theta_i V^2(t) \\ + \sum_{j,k,l=1}^{n} F_{ijkl}(q_j q_k \ddot{q}_l + q_j \dot{q}_k \dot{q}_l) - \sum_{j,k=1}^{n} K_{ijk}q_j q_k V(t) + \sum_{j=1}^{n} N_{ij}q_j V(t) = \frac{\delta W}{\delta q_i} = \sum_{j=1}^{n} Fe_{ij}q_j \cos(\Omega t)\end{aligned} \tag{3.3}$$

and

$$\begin{aligned}\sum_{i=1}^{n} \chi_i \dot{q}_i + \sum_{i,j,k=1}^{n} L_{ijk}q_i q_j \dot{q}_k + \frac{\in_{33}^{s} bL}{h_p}\dot{V}(t) - \sum_{i,j=1}^{n} U_{ij}q_i \dot{q}_j - \frac{\alpha_4 bL}{h_p^2}V(t)\dot{V}(t) + \sum_{i=1}^{n} k_i q_i \dot{V}(t) \\ + \sum_{i=1}^{n} \sigma_i \dot{q}_i V(t) + \frac{V}{R} = 0\end{aligned} \tag{3.4}$$

where

$$
\begin{aligned}
M_{ij} &= m\int_0^L \phi_i(x)\phi_j(x)dx + M\phi_i(L)\phi_j(L) + I_1\phi_i'(L)\phi_j'(L)\\
B_{ij} &= E_{y_3}\int_0^L \phi_i''(x)\phi_j''(x)dx\\
\lambda_i &= \tfrac{1}{2}\beta_1\phi_i'(L)\\
D_{ijk} &= \tfrac{3}{2}\beta_2\int_0^L \phi_i''(x)\phi_j''(x)\phi_k''(x)dx\\
E_{ijkl} &= E_{y_3}\int_0^L (\phi_i''(x)\phi_j''(x)\phi_k'(x)\phi_l'(x) + \phi_i'(x)\phi_j'(x)\phi_k''(x)\phi_l''(x))dx\\
F_{ijkl} &= m\int_0^L (\int_0^x \phi_i'\phi_j'ds)(\int_0^x \phi_k'\phi_l'ds)dx + M(\int_0^L \phi_i'\phi_j'dx)(\int_0^L \phi_k'\phi_l'dx)\\
K_{ijk} &= \tfrac{1}{4}\beta_1\int_0^L (\phi_i'(x)\phi_j'(x)\phi_k''(x) + \phi_i'(x)\phi_j''(x)\phi_k'(x) + \phi_i''(x)\phi_j'(x)\phi_k'(x))dx\\
\theta_i &= \tfrac{1}{2}\beta_3\phi_i'(L)\\
N_{ij} &= \beta_4\int_0^L \phi_i''(x)\phi_j''(x)dx\\
\chi_i &= e_{31}bh_p\phi_i'(L)\\
L_{ijk} &= e_{31}bh_p\int_0^L (\tfrac{1}{2}\phi_i'(x)\phi_j'(x)\phi_k''(x) + \phi_i'(x)\phi_j''(x)\phi_k'(x))dx\\
U_{ij} &= b\alpha_3(y_2^2 - y_1^2)\int_0^L \phi_i''(x)\phi_j''(x)dx\\
k_i &= b\alpha_2\phi_i'(L)\\
\sigma_i &= b\alpha_2\phi_i'(L)\\
Fe_{ij} &= -(mF\int_0^L [(x-L)\phi_i(x)\phi_j''(x) + \phi_i(x)\phi_j'(x)]dx + MF\phi_i(L)\phi_j'(L))
\end{aligned}
$$

and

$$
\begin{aligned}
\beta_1 &= e_{31}b(y_1 + y_2)\\
\beta_2 &= \frac{1}{12}b\alpha_1(y_2^4 - y_1^4)\\
\beta_3 &= \frac{b\alpha_2(y_1 + y_2)}{2h_p}\\
\beta_4 &= \frac{b\alpha_3(y_2^3 - y_1^3)}{3h_p}
\end{aligned}
$$

3.1.2 Normalized problem

To simplify the problem, we keep three terms in the discretization (i.e., $n = 3$) and define the state variables

$$\mathbf{X} = \begin{bmatrix} X_1 \\ X_2 \\ X_3 \\ X_4 \\ X_5 \\ X_6 \\ X_7 \end{bmatrix} = \begin{bmatrix} q_1 \\ \dot{q}_1 \\ q_2 \\ \dot{q}_2 \\ q_3 \\ \dot{q}_3 \\ V \end{bmatrix} \tag{3.5}$$

In terms of these state variable, we express the reduced-order model as

$$\dot{\mathbf{X}} = B\mathbf{X} + F\cos(\Omega t)\tilde{\Lambda}\mathbf{X} + \tilde{\mathbf{N}}(\mathbf{X}) \tag{3.6}$$

where

$$B = \begin{bmatrix} 0 & 1 & 0 & 0 & 0 & 0 & 0 \\ -\tilde{\omega}_1^2 & 0 & 0 & 0 & 0 & 0 & \frac{\lambda_1}{M_{11}} \\ 0 & 0 & 0 & 1 & 0 & 0 & 0 \\ 0 & 0 & -\tilde{\omega}_2^2 & 0 & 0 & 0 & \frac{\lambda_2}{M_{22}} \\ 0 & 0 & 0 & 0 & 0 & 1 & 0 \\ 0 & 0 & 0 & 0 & -\tilde{\omega}_3^2 & 0 & \frac{\lambda_3}{M_{33}} \\ 0 & -\frac{\chi_1}{C_p} & 0 & -\frac{\chi_2}{C_p} & 0 & -\frac{\chi_3}{C_p} & -\frac{1}{RC_p} \end{bmatrix}$$

$$\tilde{\Lambda} = \begin{bmatrix} 0 & 0 & 0 & 0 & 0 & 0 & 0 \\ \tilde{\Lambda}_{11} & 0 & \tilde{\Lambda}_{12} & 0 & \tilde{\Lambda}_{13} & 0 & 0 \\ 0 & 0 & 0 & 0 & 0 & 0 & 0 \\ \tilde{\Lambda}_{21} & 0 & \tilde{\Lambda}_{22} & 0 & \tilde{\Lambda}_{23} & 0 & 0 \\ 0 & 0 & 0 & 0 & 0 & 0 & 0 \\ \tilde{\Lambda}_{31} & 0 & \tilde{\Lambda}_{32} & 0 & \tilde{\Lambda}_{33} & 0 & 0 \\ 0 & 0 & 0 & 0 & 0 & 0 & 0 \end{bmatrix}$$

$$\tilde{\mathbf{N}} = \begin{bmatrix} 0 \\ \tilde{N}_2 \\ 0 \\ \tilde{N}_4 \\ 0 \\ \tilde{N}_6 \\ \tilde{N}_7 \end{bmatrix}$$

the $\tilde{\omega}_i$ are the structural natural frequencies, and the $\tilde{N}_i$ are nonlinear functions of the X_i. Letting G be the matrix whose columns are the eigenvectors of the matrix corresponding to the eigenvalues $\pm j\omega_1 - \mu_1$, $\pm j\omega_2 - \mu_2$, $\pm j\omega_3 - \mu_3$, and $-\mu_7$ of B, we define a new vector $\mathbf{Y}$ such that $\mathbf{X} = G\mathbf{Y}$ and rewrite equation (3.6) as

$$G\dot{\mathbf{Y}} = BG\mathbf{Y} + F\tilde{\Lambda}\cos(\Omega t)G\mathbf{Y} + \tilde{\mathbf{N}}(G\mathbf{Y}) \tag{3.7}$$

Multiplying equation (3.7) from the left by the inverse G^{-1} of G, we obtain

$$\dot{\mathbf{Y}} = J\mathbf{Y} + F\Lambda\mathbf{Y}\cos(\Omega t) + \mathbf{N}(\mathbf{Y}) \tag{3.8}$$

where $\Lambda = G^{-1}\tilde{\Lambda}G$ and $J = G^{-1}BG$ is a diagonal matrix whose elements are the eigenvalues $\pm j\omega_1 - \mu_1$, $\pm j\omega_2 - \mu_2$, $\pm j\omega_3 - \mu_3$, and $-\mu_7$ of B. We note that $Y_2 = \overline{Y_1}$, $Y_4 = \overline{Y_3}$, and $Y_6 = \overline{Y_5}$ and hence equation (3.8) can be written in component form as

$$\dot{Y}_1 = j\omega_1 Y_1 - \mu_1 Y_1 + F\sum_1^7 \Lambda_{1i} Y_i \cos(\Omega t) + Q_1(\mathbf{Y},\mathbf{Y}) + C_1(\mathbf{Y},\mathbf{Y},\mathbf{Y}) \tag{3.9}$$

$$\dot{Y}_3 = j\omega_2 Y_3 - \mu_2 Y_3 + F\sum_1^7 \Lambda_{3i} Y_i \cos(\Omega t) + Q_3(\mathbf{Y},\mathbf{Y}) + C_3(\mathbf{Y},\mathbf{Y},\mathbf{Y}) \tag{3.10}$$

$$\dot{Y}_5 = j\omega_3 Y_5 - \mu_3 Y_5 + F\sum_1^7 \Lambda_{5i} Y_i \cos(\Omega t) + Q_5(\mathbf{Y},\mathbf{Y}) + C_5(\mathbf{Y},\mathbf{Y},\mathbf{Y}) \tag{3.11}$$

$$\dot{Y}_7 = -\mu_7 Y_7 + F\sum_1^7 \Lambda_{7i} Y_i \cos(\Omega t) + Q_7(\mathbf{Y},\mathbf{Y}) + C_7(\mathbf{Y},\mathbf{Y},\mathbf{Y}) \tag{3.12}$$

where the $Q_i(\mathbf{Y},\mathbf{Y})$ are bilinear functions of the components of $\mathbf{Y}$; the $C_i(\mathbf{Y},\mathbf{Y},\mathbf{Y})$ are trilinear functions of the components of $\mathbf{Y}$. The ω_i are the first three global natural frequencies that take into account the piezoelectric effect. The μ_i are damping coefficients due to the

piezoelectric coupling and electrical resistance. The damping coefficients are adjusted to include all other forms of linear damping. Moreover, we add terms in the modulation equations that account for nonlinear aerodynamic damping.

3.2 Multiple Scales Analysis

To determine a second-order approximate solution of the system response to a principal parametric resonance of the first global mode (i.e., $\Omega \approx 2\omega_1$), we use the method of multiple scales (192; 193). To this end, we introduce a small nondimensional parameter ϵ as a bookkeeping parameter and scale F as $\epsilon^2 F$, the Q_i as ϵQ_i, the C_i as $\epsilon^2 C_i$, and the damping coefficients μ_i as $\epsilon^2 \mu_i$ except μ_7, which is scaled to be $O(1)$. Moreover, we expand the Y_i as

$$Y_1 = Y_{11}(T_0, T_1, T_2) + \epsilon Y_{12}(T_0, T_1, T_2) + \epsilon^2 Y_{13}(T_0, T_1, T_2) + O(\epsilon^3) \tag{3.13}$$

$$Y_3 = Y_{31}(T_0, T_1, T_2) + \epsilon Y_{32}(T_0, T_1, T_2) + \epsilon^2 Y_{33}(T_0, T_1, T_2) + O(\epsilon^3) \tag{3.14}$$

$$Y_5 = Y_{51}(T_0, T_1, T_2) + \epsilon Y_{52}(T_0, T_1, T_2) + \epsilon^2 Y_{53}(T_0, T_1, T_2) + O(\epsilon^3) \tag{3.15}$$

$$Y_7 = Y_{71}(T_0, T_1, T_2) + \epsilon Y_{72}(T_0, T_1, T_2) + \epsilon^2 Y_{73}(T_0, T_1, T_2) + O(\epsilon^3) \tag{3.16}$$

where $T_n = \epsilon^n t$. In terms of the T_i, the time derivative can be expressed as

$$\frac{d}{dt} = \frac{\partial}{\partial T_0} + \epsilon \frac{\partial}{\partial T_1} + \epsilon^2 \frac{\partial}{\partial T_2} + \cdots = d_0 + \epsilon d_1 + \epsilon^2 d_2 + \cdots \tag{3.17}$$

Next, we express the nearness of the principal parametric resonance using the detuning parameter σ as

$$\Omega = 2\omega_1 + \epsilon^2 \sigma \tag{3.18}$$

Substituting equations (3.13)-(3.18) into equations (3.9)-(3.12), using the scalings, and equating coefficients of like powers of ϵ, we obtain three problems for the Y_{mn}. We note that in the absence of direct excitation of the higher modes and in the absence of internal resonances involving the first mode, the Y_{m1} for $m \neq 1$ decay with time and hence we let $Y_{m1} = 0$ for $m \neq 1$. Moreover, we note that secular terms appear at $O(\epsilon^2)$ and hence there is no dependence on T_1. Consequently, the problems at different orders reduce to

Order ϵ^0

$$d_0 Y_{11} = j\omega_1 Y_{11} \tag{3.19}$$

Order ϵ

$$d_0 Y_{12} = j\omega_1 Y_{12} + q_{11} Y_{11}^2 + q_{12} Y_{11} \overline{Y}_{11} + q_{13} \overline{Y}_{11}^2 \tag{3.20}$$

$$d_0 Y_{32} = j\omega_2 Y_{32} + q_{31} Y_{11}^2 + q_{32} Y_{11} \overline{Y}_{11} + q_{33} \overline{Y}_{11}^2 \tag{3.21}$$

$$d_0 Y_{52} = j\omega_3 Y_{52} + q_{51} Y_{11}^2 + q_{52} Y_{11} \overline{Y}_{11} + q_{53} \overline{Y}_{11}^2 \tag{3.22}$$

$$d_0 Y_{72} = -\mu_7 Y_{72} + q_{71} Y_{11}^2 + q_{72} Y_{11} \overline{Y}_{11} + q_{73} \overline{Y}_{11}^2 \tag{3.23}$$

Order ϵ^2

$$\begin{aligned} d_0 Y_{13} = j\omega_1 Y_{13} - d_2 Y_{11} - \mu_1 Y_{11} + 2q_{11} Y_{11} Y_{12} + q_{12} Y_{11} \overline{Y}_{12} + q_{12} \overline{Y}_{11} Y_{12} \\ +2q_{13} \overline{Y}_{11} \overline{Y}_{12} + q_{14} Y_{11} Y_{32} + q_{15} \overline{Y}_{11} Y_{32} + q_{16} Y_{11} Y_{52} + q_{17} \overline{Y}_{11} Y_{52} \\ +q_{18} Y_{11} Y_{72} + q_{19} \overline{Y}_{11} Y_{72} + \tilde{q}_{14} Y_{11} \overline{Y}_{32} + \tilde{q}_{15} \overline{Y}_{11} \overline{Y}_{32} + \tilde{q}_{16} Y_{11} \overline{Y}_{52} \\ +\tilde{q}_{17} \overline{Y}_{11} \overline{Y}_{52} + c_{11} Y_{11}^3 + c_{12} Y_{11}^2 \overline{Y}_{11} + c_{13} Y_{11} \overline{Y}_{11}^2 \\ +c_{14} \overline{Y}_{11}^3 + F\Lambda_{12} \overline{Y}_{11} \cos(\Omega t) + NST \end{aligned} \tag{3.24}$$

where NST stands for terms that do not produce secular terms.

The solution of equation (3.19) can be expressed as

$$Y_{11} = A(T_2) e^{j\omega_1 T_0} \tag{3.25}$$

Substituting equation (3.25) into equations (3.20)-(3.23) and solving the resulting equations, we obtain

$$Y_{12} = \frac{-jq_{11}}{\omega_1} A^2 e^{2j\omega_1 T_0} + \frac{jq_{12}}{\omega_1} A\overline{A} + \frac{jq_{13}}{3\omega_1} \overline{A}^2 e^{-2j\omega_1 T_0} \tag{3.26}$$

$$Y_{32} = \frac{jq_{31}}{\omega_2 - 2\omega_1} A^2 e^{2j\omega_1 T_0} + \frac{jq_{32}}{\omega_2} A\overline{A} + \frac{jq_{33}}{\omega_2 + 2\omega_1} \overline{A}^2 e^{-2j\omega_1 T_0} \tag{3.27}$$

$$Y_{52} = \frac{jq_{51}}{\omega_3 - 2\omega_1} A^2 e^{2j\omega_1 T_0} + \frac{jq_{52}}{\omega_3} A\overline{A} + \frac{jq_{53}}{\omega_3 + 2\omega_1} \overline{A}^2 e^{-2j\omega_1 T_0} \tag{3.28}$$

$$Y_{72} = \frac{q_{71}}{2j\omega_1 + \mu_7} A^2 e^{2j\omega_1 T_0} + \frac{q_{72}}{\mu_7} A\overline{A} + \frac{q_{73}}{-2j\omega_1 + \mu_7} \overline{A}^2 e^{-2j\omega_1 T_0} \tag{3.29}$$

Substituting equations (3.18) and (3.25-3.29) into equation (3.24) and eliminating the terms that lead to secular terms, we obtain the complex-valued modulation equation

$$d_2 A = -\mu_1 A + \alpha_e A^2 \overline{A} + \frac{1}{2} F\Lambda_{12} \overline{A} e^{j\sigma T_2} \tag{3.30}$$

where

$$\alpha_e = c_{12} + \frac{jq_{12}q_{11}}{\omega_1} - \frac{jq_{12}\overline{q}_{12}}{\omega_1} - \frac{2jq_{13}\overline{q}_{13}}{3\omega_1} + \frac{jq_{14}q_{32}}{\omega_2} + \frac{jq_{15}q_{31}}{\omega_2 - 2\omega_1} + \frac{jq_{16}q_{52}}{\omega_3} + \frac{jq_{17}q_{51}}{\omega_3 - 2\omega_1} + \frac{q_{18}q_{72}}{\mu_7} + \frac{q_{19}q_{71}}{2j\omega_1 + \mu_7} - \frac{j\tilde{q}_{14}\overline{q}_{32}}{\omega_2} - \frac{j\tilde{q}_{15}\overline{q}_{33}}{\omega_2 + 2\omega_1} - \frac{j\tilde{q}_{16}\overline{q}_{52}}{\omega_3} - \frac{j\tilde{q}_{17}\overline{q}_{53}}{\omega_3 + 2\omega_1} \tag{3.31}$$

Expressing A in the polar form $A = \frac{1}{2}a(T_2)e^{j\eta(T_2)}$, we rewrite equation (3.30) as

$$a' + aj\eta' = -\mu_1 a + \frac{1}{4}\alpha_e a^3 + \frac{1}{2}aF\Lambda_{12}e^{j\sigma T_2 - 2\eta} \tag{3.32}$$

Separating real and imaginary parts in equation (3.32) yields

$$a' = -\mu_1 a + \frac{1}{4}\mathrm{Re}(\alpha_e)a^3 + \frac{1}{2}aF|\Lambda_{12}|\cos(\sigma T_2 + \theta_1 - 2\eta) \tag{3.33}$$

$$a\eta' = \frac{1}{4}\mathrm{Im}(\alpha_e)a^3 + \frac{1}{2}aF|\Lambda_{12}|\sin(\sigma T_2 + \theta_1 - 2\eta) \tag{3.34}$$

where $\Lambda_{12} = |\Lambda_{12}|e^{i\theta_1}$ and Re and Im stand for the real and imaginary parts, respectively. In equation (3.33), we adjust μ_1 to include all linear structural and electrical damping and we add the nonlinear damping term $\frac{4}{3\pi}\mu_2 a^2$, reflecting aerodynamic damping. These damping coefficients are usually estimated from experimental results. Thus, equation (3.33) becomes

$$a' = -\mu_1 a - \frac{4}{3\pi}\mu_2 a^2 + \frac{1}{4}\mathrm{Re}(\alpha_e)a^3 + \frac{1}{2}aF|\Lambda_{12}|\cos(\sigma T_2 + \theta_1 - 2\eta) \tag{3.35}$$

The preceding non-autonomous system of equations can be transformed to an autonomous system by introducing the following transformation:

$$\beta = \sigma T_2 + \theta_1 - 2\eta \tag{3.36}$$

Then,

$$\eta = \frac{1}{2}(\sigma T_2 + \theta_1 - \beta) \tag{3.37}$$

and

$$\eta' = \frac{1}{2}(\sigma - \beta') \tag{3.38}$$

Substituting equations (3.36)-(3.38) into equations (3.34) and (3.35), we obtain the autonomous modulation equations

$$a' = -\mu_1 a - \frac{4}{3\pi}\mu_2 a^2 + \frac{1}{4}\mathrm{Re}(\alpha_e)a^3 + \frac{1}{2}aF|\Lambda_{12}|\cos\beta \tag{3.39}$$

$$\frac{1}{2}a\beta' = \frac{1}{2}\sigma a - \frac{1}{4}\mathrm{Im}(\alpha_e)a^3 - \frac{1}{2}aF|\Lambda_{12}|\sin\beta \tag{3.40}$$

By solving the modulation equations, we can determine the Y_{mn} and then the deflection, output voltage, and harvested power. To determine the steady-state responses, we set the time derivatives in these equations equal to zero. Then, we square and add the resulting equations to obtain the frequency-response equation

$$\left[\mu_1 + \frac{4}{3\pi}\mu_2 a - \frac{1}{4}\mathrm{Re}(\alpha_e)a^2\right]^2 a^2 + \left[\frac{1}{2}\sigma - \frac{1}{4}\mathrm{Im}(\alpha_e)a^2\right]^2 a^2 = \frac{1}{4}a^2F^2|\Lambda_{12}|^2 \tag{3.41}$$

Then,

$$\tan\beta = \frac{\frac{1}{2}\sigma - \frac{1}{4}\mathrm{Im}(\alpha_e)a^2}{\mu_1 + \frac{4}{3\pi}\mu_2 a - \frac{1}{4}\mathrm{Re}(\alpha_e)a^2} \tag{3.42}$$

Solving the preceding equations, we rewrite Y_{11} as follows:

$$Y_{11} = \frac{1}{2}ae^{\frac{1}{2}j(\Omega t + \theta_1 - \beta)} \tag{3.43}$$

After obtaining the expression of Y_{11} and using $\mathbf{X} = G\mathbf{Y}$, we can easily determine expressions for the generated voltage ($V(t) = X_7(t)$) and tip deflection

$$v(L,t) = \phi_1(L)X_1(t) + \phi_2(L)X_3(t) + \phi_3(L)X_5(t)$$

The maximum voltage output and harvested power are then given by

$$V = a\sqrt{G[7,1]_r^2 + G[7,1]_i^2} \tag{3.44}$$

$$P = \frac{V^2}{R} \tag{3.45}$$

where $(.)_r$ and $(.)_i$ denote the real part and imaginary part, respectively.

3.3 Effective Nonlinearity Conditions

Considering the free vibration case ($F = 0N$), we rewrite the autonomous modulation equations as

$$a' = -\mu_1 a - \frac{4}{3\pi}\mu_2 a^2 + \frac{1}{4}\mathrm{Re}(\alpha_e)a^3 \tag{3.46}$$

$$\frac{1}{2}a\beta' = \frac{1}{2}\sigma a - \frac{1}{4}\mathrm{Im}(\alpha_e)a^3 \tag{3.47}$$

whose equilibrium solutions are given by

$$(-\mu_1 - \frac{4}{3\pi}\mu_2 a + \frac{1}{4}\mathrm{Re}(\alpha_e)a^2)a = 0$$

This equation has three solutions. One of them is the trivial solution ($a = 0$) and the others can be real or complex-valued depending on the value of $Re(\alpha_e)$. The expression of the effective nonlinearity (α_e) includes contributions of all nonlinearities (piezoelectric, inertia, geometric). For the free-vibration configuration, the nontrivial solutions have to be complex-valued to obtain physical response. Hence,

$$\mathrm{Re}(\alpha_e) < 0$$

In addition, the imaginary part of the effective nonlinearity describes the softening/hardening behavior. In fact, if $Im(\alpha_e) > 0$, the system has a hardening behavior. On the other hand, if $Im(\alpha_e) < 0$, the system has a softening behavior. For our studied configuration, the real and imaginary parts of this effective nonlinearity are given by:

$$\begin{aligned} Re(\alpha_e) = 2.6466 \times 10^{-6} + 6.8137 \times 10^{-35}\alpha_1^2 - 1.3745 \times 10^{-15}\alpha_1\alpha_2 - 35844.8\alpha_2^2 \\ -2.7176 \times 10^{-23}\alpha_1\alpha_3 + 0.00012 \times \alpha_2\alpha_3 - 1.0717 \times 10^{-13}\alpha_3^2 + 1.6882 \times 10^{-6}\alpha_1\alpha_4 \\ +2.6257 \times 10^{13}\alpha_2\alpha_4 - 41859.5\alpha_3\alpha_4 - 4.2274 \times 10^{21}\alpha_4^2 \end{aligned} \tag{3.48}$$

$$\begin{aligned} Im(\alpha_e) = 0.000026 - 6.2095 \times 10^{-32}\alpha_1^2 - 2.7809 \times 10^{-16}\alpha_1\alpha_2 + 5899.93 \times \alpha_2^2 \\ +3.4798 \times 10^{-23}\alpha_1\alpha_3 - 0.000089\alpha_2\alpha_3 + 1.6937 \times 10^{-13}\alpha_3^2 - 2.9312 \times 10^{-7}\alpha_1\alpha_4 \\ +4.1643 \times 10^{12}\alpha_2\alpha_4 + 24605.1\alpha_3\alpha_4 - 3.5072 \times 10^{21}\alpha_4^2 \end{aligned} \tag{3.49}$$

3.4 Results

We first investigate the required number of modes in the Galerkin discretization to accurately predict the performance of this energy harvester. Then, we identify the impact of the nonlinear piezoelectric coefficients (α_1, α_2, α_3, and α_4), quadratic damping coefficient, and excitation amplitude on the voltage output and harvested power. In all of the following figures, the solid lines indicate stable solutions and dashed lines indicate unstable solutions.

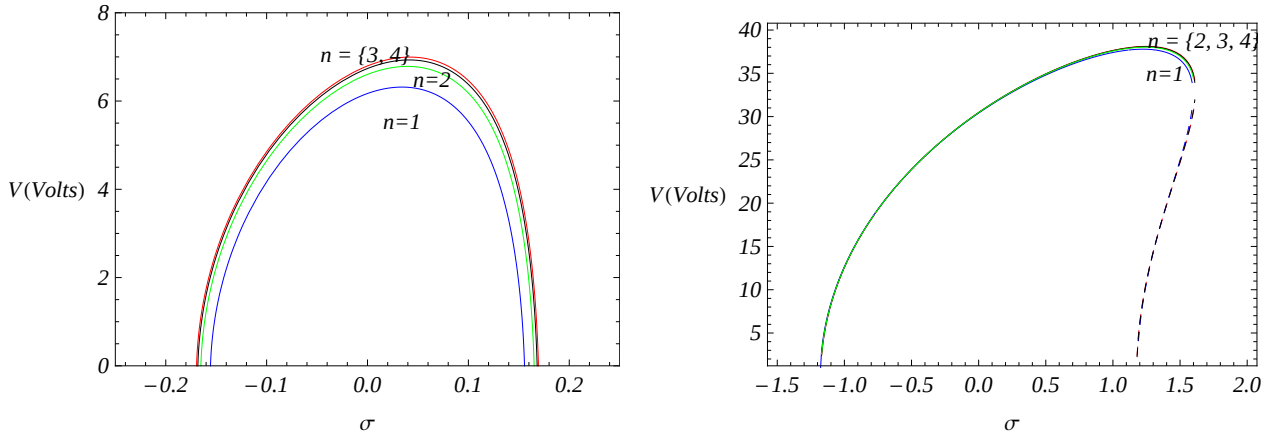

(a) $F = 4m/s^2$ (b) $F = 10m/s^2$

Figure 3.2: Variation of the voltage output with the detuning σ for different values of n when $R = 10^5\Omega$, $\mu_2 = 0.0005m^{-1}$, $\alpha_1 = \alpha_2 = \alpha_4 = 0$, $\alpha_3 = -10^5 C.m^{-2}$.

3.4.1 Required number of modes in the Galerkin discretization

Predicted values of the voltage output as a function of the detuning parameter, σ, for two different values of the excitation amplitude F are presented in Figure 3.3. In addition to the geometric and inertia nonlinearities, only the effect of the third nonlinear coefficient (α_3) is considered. The results show that the output voltage converges as the number of global modes is increased. Clearly, taking into consideration one mode is not sufficient as it underpredicts the voltage output.

The effects of including the coupling between the nonlinear piezoelectric coefficients resulting from the nonlinear stress-strain relations, nonlinear voltage effects, and the nonlinear coupling between the strain and voltage on the voltage output are presented in Figures 3.3 and 3.4. In all cases, the same value of quadratic damping and the two different cases of the excitation amplitude are considered. The results also show that, in all cases, one needs to consider at least three modes to correctly predict the output voltage. Furthermore, an increase in the excitation amplitude could yield unstable responses and show softening or hardening characteristics depending on the considered nonlinear piezoelectric coefficients.

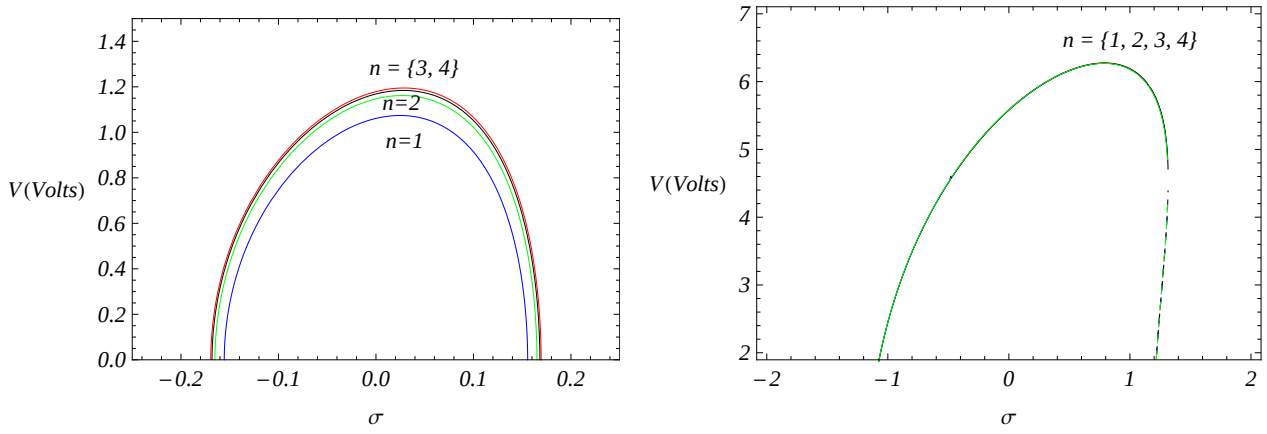

(a) $F = 4m/s^2$ (b) $F = 10m/s^2$

Figure 3.3: Variation of the voltage output with the detuning σ for different values of n when $R = 10^5\Omega$, $\mu_2 = 0.0005m^{-1}$, $\alpha_1 = -5\times10^{14}Pa, \alpha_2 = 10^{-4}N.V^{-2}, \alpha_3 = -5\times10^5 C.m^{-2}, \alpha_4 = 0$.

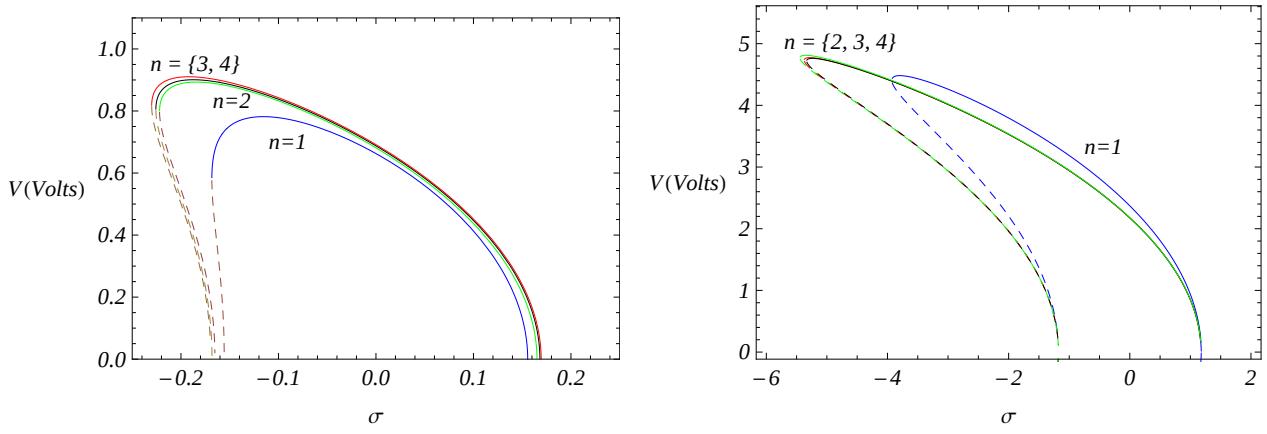

(a) $F = 4m/s^2$ (b) $F = 10m/s^2$

Figure 3.4: Variation of the voltage output with the detuning σ for different values of n when $R = 10^5\Omega$, $\mu_2 = 0.0005m^{-1}$, $\alpha_1 = -3\times10^{15}Pa, \alpha_2 = 10^{-4}N.V^{-2}, \alpha_3 = -5\times10^5 C.m^{-2}, \alpha_4 = 2\times10^{-13}C.V^{-2}$.

The nonlinear piezoelectric coefficients used in Figure 3.3 resulted in a hardening behavior, whereas those used in Figure 3.4 resulted in a softening behavior.

3.4.2 Effect of the nonlinear piezoelectric coefficients on the harvester outputs

Next, we investigate the effect of variations in the nonlinear piezoelectric coefficients on the output voltage; the nonlinear coefficients satisfy the condition in equation (3.49). In all results, three modes are considered and the load resistance, quadratic damping coefficient, and forcing amplitude are kept constant. It follows from equation (3.48) that these coefficients affect the real part of the effective nonlinearity and hence it follows from equation (3.46) that they strongly affect the amplitude of the limit cycle. Moreover, it follows from equation (3.49) that these coefficients affect the imaginary part of the effective nonlinearity and hence it follows from equation (3.47) that they determine whether the harvester behavior is hardening or softening. We start with varying α_1 and keeping the other parameters the same as in Figure 3.3. Figure 3.5-a shows that this coefficient (α_1) has a significant impact on the generated voltage. Increasing this value, the system's response changes from hardening to softening as shown in Figure 3.5-a. Furthermore, the generated voltage decreases with increasing α_1. We note also that the frequency range in which the trivial solution is unstable is independent of the first nonlinear piezoelectric coefficient.

The influence of the second nonlinear piezoelectric coefficient (α_2) on the output voltage is presented in Figure 3.5-b. This coefficient has a significant effect when its value is larger than $10^{-6}N.V^{-2}$. Clearly, its role is similar to that of damping. Above this critical value, the amplitude of the generated voltage decreases.

The curves plotted in Figure 3.5-c show the effect of the third nonlinear coefficient (α_3) on the harvester's behavior. Its influence is similar to that of α_2 in that it works as a damping term. However, the increase of this coefficient is followed by a significant hardening behavior.

Changing the value of the fourth nonlinear piezoelectric coefficient (α_4) on the configuration presented in Figure 3.4, the generated voltage as well as the softening behavior become more significant as the value of (α_4) is increased. Similar to the other coefficients, α_4 influences the system only when its value exceeds a critical level, namely, $10^{-14}C.V^{-2}$.

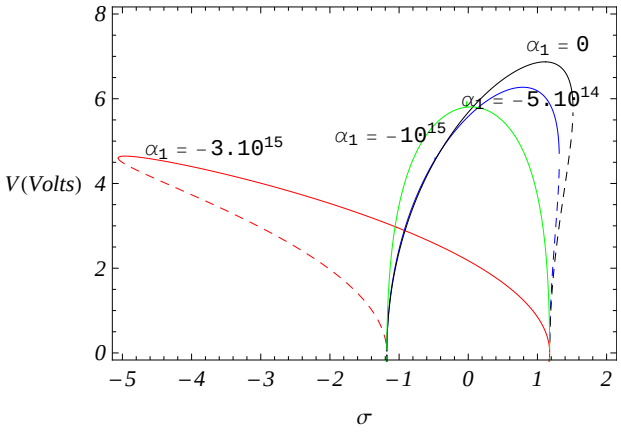

(a) $\alpha_2 = 10^{-4} N.V^{-2}, \alpha_3 = -5 \times 10^5 C.m^{-2}, \alpha_4 = 0$

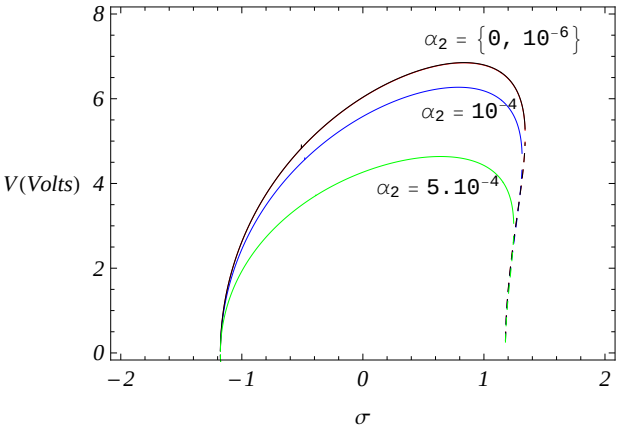

(b) $\alpha_1 = -5 \times 10^{14} Pa, \alpha_3 = -5 \times 10^5 C.m^{-2}, \alpha_4 = 0$

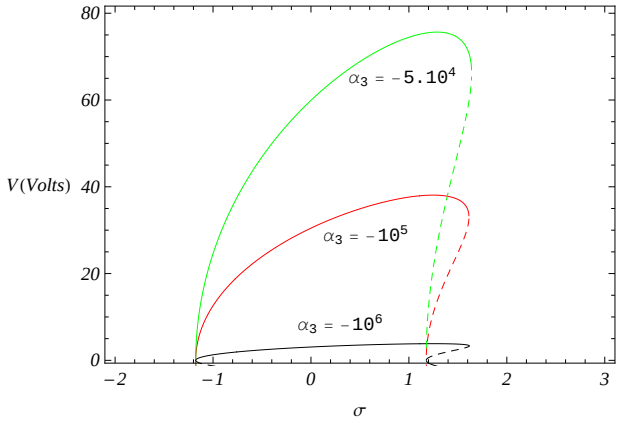

(c) $\alpha_1 = \alpha_2 = \alpha_4 = 0$

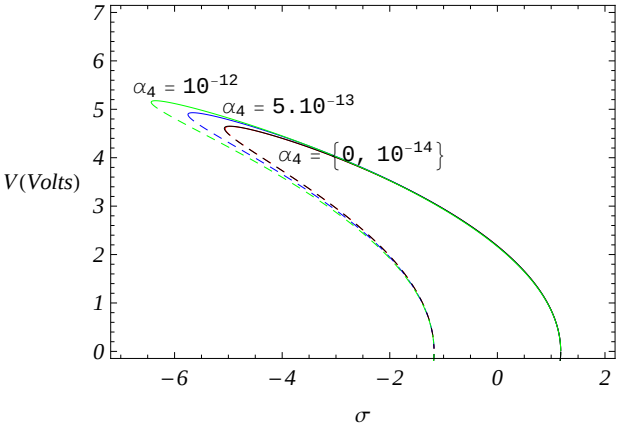

(d) $\alpha_1 = -3 \times 10^{15} Pa, \alpha_2 = 10^{-4} N.V^{-2}, \alpha_3 = -5 \times 10^5 C.m^{-2}$

Figure 3.5: Variation of the voltage output with the detuning σ for different configurations of nonlinear piezoelectric coefficients when $R = 10^5 \Omega$, $\mu_2 = 0.0005$, $F = 10m/s^2$, $n = 3$.

These results show that nonlinearities of the stress-strain relation, voltage, or its coupling with the strain impact the system's behavior and response in different manners. We note also that the effect of these nonlinear piezoelectric coefficients do not affect the frequency range in which the trivial solution is unstable.

3.4.3 Effects of the quadratic damping coefficient and excitation amplitude on the system outputs

Next, we investigate the effects of the quadratic damping coefficient as well as the excitation amplitude on the harvester's response. Figure 3.6 shows how variations in the quadratic damping influence the amplitude and characteristics of the generated voltage for two different cases of the forcing excitation amplitude. As expected, increasing μ_2 decreases the amplitude of the generated voltage. Furthermore, we note that the impact of this quadratic damping is more effective when the forcing amplitude is small. It should be noted that variations in μ_2 do not affect the frequency band in which the trivial solution is unstable.

When the beam is directly excited near its global natural frequency, the beam always oscillates, irrespective of how small the excitation amplitude is. In contrast, when the beam is parametrically excited, there is a critical value for the excitation amplitude for oscillations to occur. This means the system has nontrivial solutions only when the excitation amplitude is larger than this critical value. For the configuration investigated here, and as shown in Figures 3.7 and 3.8, the critical value of the forcing amplitude is approximately $3.8m/s^2$ and $6m/s^2$, respectively. The critical forcing value depends on the linear damping coefficient and the excitation frequency. In fact, the frequency band in which the trivial solution is unstable increases as the forcing amplitude increases. Furthermore, the quadratic damping does not affect the critical value of the excitation. For small μ_2, and depending on the excitation frequency, there is an overhang associated with a subcritical pitchfork bifurcation of the trivial solution, as shown in Figure 3.8 when $\sigma = 0.6$. For the same values of μ_2, the bifurcation is supercritical when the detuning is zero ($\sigma = 0$), as shown in Figure 3.7. This bifurcation leads to a jump from the trivial solution to nontrivial solutions when the excitation amplitude increases. Moreover, as increasing μ_2, the bifurcation changes from a subcritical pitchfork bifurcation to a transcritical bifurcation.

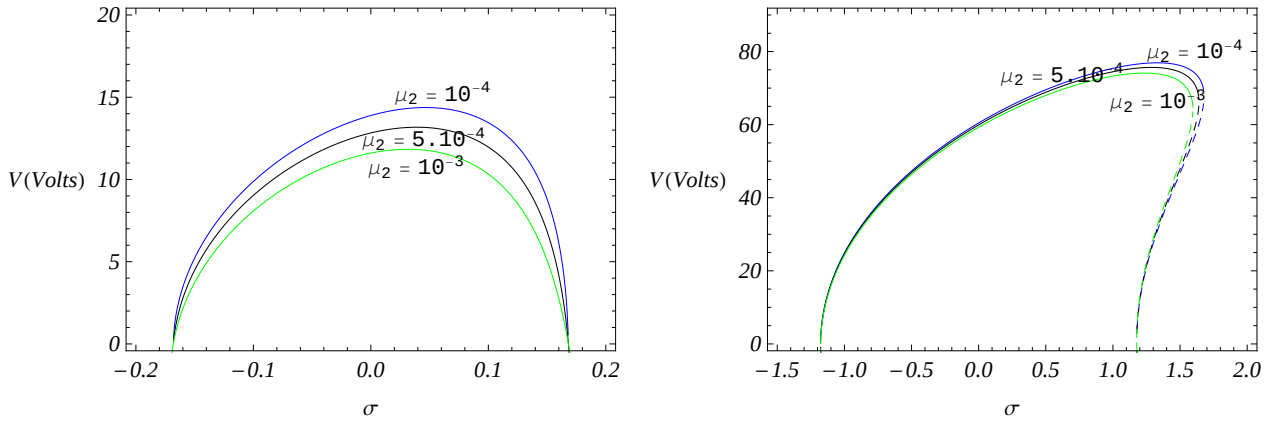

(a) $F = 4m/s^2$ (b) $F = 10m/s^2$

Figure 3.6: Variation of the voltage output with the detuning σ for different values of $\mu_2(m^{-1})$ when $R = 10^5\Omega$, $n = 3$, and $\alpha_1 = \alpha_2 = \alpha_4 = 0$, $\alpha_3 = -5 \times 10^4 C.m^{-2}$.

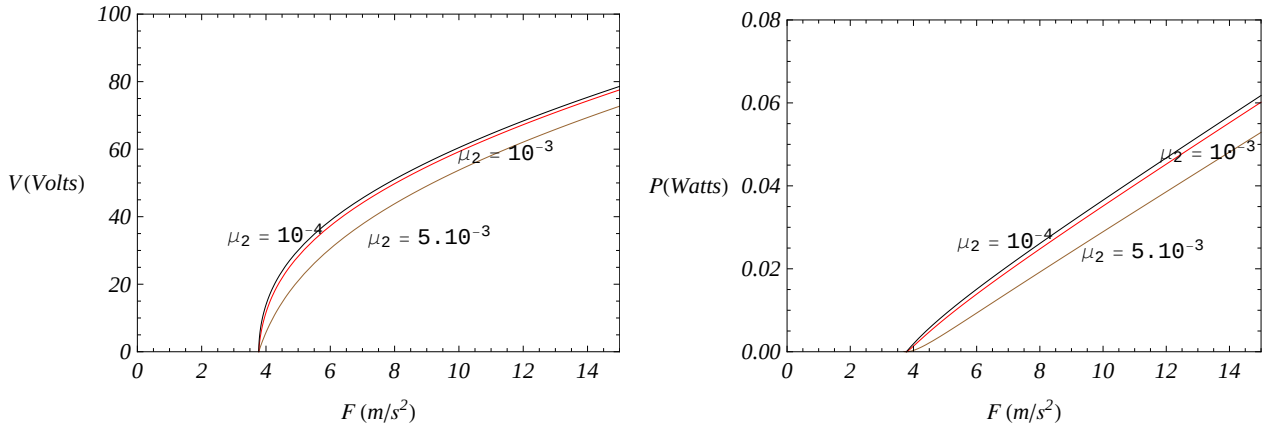

(a) (b)

Figure 3.7: Variation of the voltage output (a) and harvested power (b) with $F(m/s^2)$ for different values of $\mu_2(m^{-1})$ when $R = 10^5\Omega$, $\sigma = 0$, $n = 3$, $\alpha_1 = \alpha_2 = \alpha_4 = 0$, and $\alpha_3 = -5 \times 10^4 C.m^{-2}$.

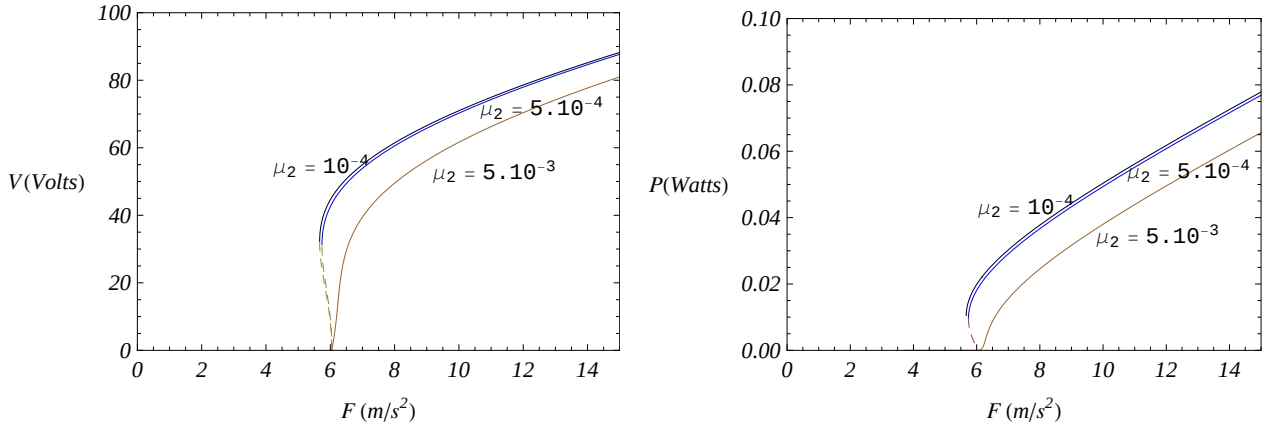

(a) (b)

Figure 3.8: Variation of the voltage output (a) and harvested power (b) with $F(m/s^2)$ for different values of $\mu_2(m^{-1})$ when $R = 10^5\Omega$, $\sigma = 0.6$, $n = 3$, $\alpha_1 = \alpha_2 = \alpha_4 = 0$, and $\alpha_3 = -5 \times 10^4 C.m^{-2}$.

3.5 Conclusions

We have developed and presented an innovative nonlinear distributed-parameter model and analysis for energy harvesting under parametric excitation of a cantilever beam with a tip mass. This model accounts for geometric, inertia, piezoelectric, and fluid drag nonlinearities. A reduced-order model is developed based on a Galerkin discretization of the governing equations derived by using the extended Hamilton principle and the Gauss law. The method of multiple scales is then implemented to determine analytical expressions for the tip deflection, output voltage, and harvested power near the first principal parametric resonance. The results show that a one-mode approximation in the Galerkin procedure is not sufficient to ascertain the performance of the harvester. A parametric study is then performed to investigate the effects of all nonlinear piezoelectric coefficients, quadratic damping, and excitation amplitude on the harvester's response. The results show that the nonlinear stress-strain piezoelectric coefficients significantly impact the magnitude of the harvester response and its behavior in terms of softening or hardening. The results also show that, depending on the excitation

frequency, an overhang associated with a subcritical pitchfork bifurcation for small quadratic damping might occur. These results show that a nonlinear distributed-parameter model that takes into consideration the first three modes is better suited than a lumped-parameter model for the design of energy harvesters and for validation through system identification of experimental setups.

Part II

Modeling, Design and Enhancement of Wing-based Piezoelectric Energy Harvesters from Aeroelastic Vibrations

Chapter 4

Modeling and Nonlinear Analysis of Piezoaeroelastic Energy Harvesters

Most studies in the field of wing-based piezoaeroelastic energy harvesting have stressed the linear characteristics of the piezoaeroelastic system with particular attention paid to the effect of some parameters on the flutter speed. Yet, the risks and potential of energy harvesting from aeroelastic vibrations can be best evaluated by assessing its nonlinear responses, such as limit-cycle oscillations, which can be controlled to yield a finite-amplitude power output and to eliminate unwanted responses. These aspects can best be evaluated by performing nonlinear analysis of any proposed piezoaeroelatsic system.

In the analysis of aeoelastic systems, the interest usually lies in their response near or at the onset of a bifurcation point. In this region and depending on the magnitudes and types of nonlinearities, the bifurcation can be of the supercritical or subcritical type. For the purpose of energy harvesting, it is important to generate energy at low wind speeds and, as such, to decrease the flutter speed. Furthermore, it is important to attain limit-cycle oscillations at low freestream velocities while avoiding subcritical Hopf bifurcation, which can lead to catastrophic failures.

The objective of this chapter is to investigate the performance of a piezoaeroelastic energy harvester composed of a rigid airfoil supported by nonlinear torsional and flexural springs in the pitch and plunge motions, respectively, with a piezoelectric coupling attached to the

plunge degree of freedom. We derive the normal form of the dynamics of the harvester near the Hopf bifurcation to determine the effects of aerodynamic nonlinearities and nonlinear plunge and pitch coefficients on the harvester behavior near the bifurcation. This nonlinear normal form is also useful to characterize the effects of different parameters on the system's output and ensure that subcritical bifurcations do not occur. Numerical solutions of the coupled equations for two different configurations are then performed to determine the effects of the load resistance and the nonlinear spring coefficients on the pitch and plunge motions, the voltage output, and the harvested power.

4.1 Modeling of the Piezoaeroelastic System

We consider a piezoaeroelastic system consisting of a rigid wing having two degrees of freedom, as shown in Figure 4.1. The wing can translate vertically (plunge motion) and rotate about the elastic axis (pitch motion). We add a piezoelectric coupling to the plunge degree of freedom and include a load resistance in the electrical field. The governing equations are expressed as (134)

$$m_T\ddot{h} + m_W x_\alpha b\ddot{\alpha} + c_h\dot{h} + k_h(h)h - \theta V = -L \tag{4.1}$$

$$m_W x_\alpha b\ddot{h} + I_\alpha\ddot{\alpha} + c_\alpha\dot{\alpha} + k_\alpha(\alpha)\alpha = M \tag{4.2}$$

$$C_p\dot{V} + \frac{V}{R} + \chi\dot{h} = 0 \tag{4.3}$$

where h is the plunge deflection, α is the pitch angle, m_T is the total mass of the wing with its support structure, m_W is the wing mass alone, I_α is the mass moment of inertia about the elastic axis, b is the half chord length, x_α is the nondimensional distance between the center of mass and the elastic axis, c_h and c_α are, respectively, the plunge and pitch structural damping coefficients, L and M are the aerodynamic lift and moment about the elastic axis, R is the load resistance, V is the voltage across this load resistance, C_p is the capacitance of the piezoelectric layer, θ and χ are electromechanical coupling terms, and k_h and k_α are the structural stiffnesses for the plunge and pitch motions, respectively. Here, we represent the

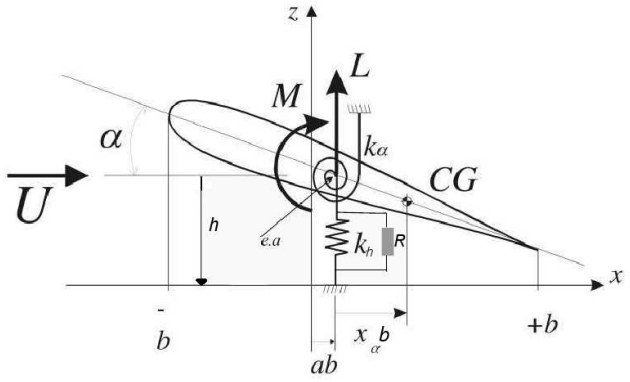

Figure 4.1: Schematic of a piezaeroelastic system under uniform airflow

stiffness for the plunge and pitch motions in polynomial form as

$$k_\alpha(\alpha) = k_{\alpha 0} + k_{\alpha 2}\alpha^2 \tag{4.4}$$

$$k_h(h) = k_{h0} + k_{h2}h^2 \tag{4.5}$$

The aerodynamic loads are evaluated using a quasi-steady approximation with a stall model (82; 199; 200) and are given by

$$L = \rho U^2 b c_{l\alpha}(\alpha_{eff} - c_s\alpha_{eff}^3) \tag{4.6}$$

$$M = \rho U^2 b^2 c_{m\alpha}(\alpha_{eff} - c_s\alpha_{eff}^3) \tag{4.7}$$

where U is the freestream velocity, $c_{l\alpha}$ and $c_{m\alpha}$ are the aerodynamic lift and moment coefficients, and c_s is a nonlinear parameter associated with stall. The effective angle of attack, α_{eff} due to the instantaneous motion of the airfoil is given by (201)

$$\alpha_{eff} = \alpha + \frac{\dot{h}}{U} + (\frac{1}{2} - a)b\frac{\dot{\alpha}}{U}$$

Considering the following state variables:

$$X = \begin{bmatrix} X_1 \\ X_2 \\ X_3 \\ X_4 \\ X_5 \end{bmatrix} = \begin{bmatrix} h \\ \dot{h} \\ \alpha \\ \dot{\alpha} \\ V \end{bmatrix} \tag{4.8}$$

we rewrite the equations of motion as

$$\dot{X}_1 = X_2 \tag{4.9}$$

$$\dot{X}_2 = -\tfrac{I_\alpha k_{h0}}{d} X_1 - (c_1 + d_1 U) X_2 - (k_1 U^2 - \tfrac{m_W x_\alpha b k_{\alpha 0}}{d}) X_3 - (c_2 + d_2 U) X_4 - \theta_1 X_5$$
$$- N_{1\alpha}(X) - N_{1h}(X) + N_{NL1}$$

$$\dot{X}_3 = X_4$$

$$\dot{X}_4 = \tfrac{m_W x_\alpha b k_{h0}}{d} X_1 - (c_3 + d_3 U) X_2 - (k_2 U^2 + \tfrac{k_{\alpha 0} m_T}{d}) X_3 - (c_4 + d_4 U) X_4 - \theta_2 X_5$$
$$- N_{2\alpha}(X) - N_{2h}(X) + N_{NL2}$$

$$\dot{X}_5 = -\tfrac{\chi_1}{C_p} X_2 - \tfrac{1}{R C_p} X_5$$

where

$$d = m_T I_\alpha - (m_w x_\alpha b)^2$$

$$c_1 = [I_\alpha (c_h - \kappa_h)]/d$$

$$d_1 = [I_\alpha \rho b c_{l\alpha} + \rho b^3 m_w x_\alpha c_{m\alpha}]/d$$

$$c_2 = [-m_w x_\alpha b (c_\alpha - \kappa_\alpha)]/d$$

$$d_2 = [I_\alpha \rho b^2 c_{l\alpha} (\tfrac{1}{2} - a) + m_w x_\alpha b^4 \rho c_{m\alpha} (\tfrac{1}{2} - a)]/d$$

$$c_3 = [-m_w x_\alpha b (c_h - \kappa_h)]/d$$

$$d_3 = [-m_w x_\alpha b \rho b c_{l\alpha} - m_T c_{m\alpha} \rho b^2]/d$$

$$c_4 = [m_T (c_\alpha - \kappa_\alpha)]/d$$

$$d_4 = [-m_T b^3 \rho c_{m\alpha} (\tfrac{1}{2} - a) - m_w x_\alpha b^3 \rho c_{l\alpha} (\tfrac{1}{2} - a)]/d$$

$$k_1 = [I_\alpha \rho b c_{l\alpha} + m_w x_\alpha b^3 \rho c_{m\alpha}]/d$$

$$k_2 = -[\rho b^2 c_{l\alpha} m_w x_\alpha + m_T \rho b^2 c_{m\alpha}]/d$$

$$N_{1h} = I_\alpha [k_{h2} X_1^3]/d$$

$$N_{1\alpha} = -m_w x_\alpha b [k_{\alpha 2} X_3^3]/d$$

$$N_{2h} = -m_w x_\alpha b [k_{h2} X_1^3]/d$$

$$N_{2\alpha} = m_T [k_{\alpha 2} X_3^3]/d$$

$$N_{NL1} = [\rho U^2 c_s b (c_{l\alpha} I_\alpha + m_w x_\alpha b^2 c_{m\alpha}) \alpha_{eff}(X)]/d$$

$$N_{NL2} = -[c_s \rho U^2 b^2 (c_{l\alpha} m_w x_\alpha + m_T c_{m\alpha}) \alpha_{eff}(X)]/d$$

In vector form, the equations of motion are expressed as

$$\dot{\mathbf{X}} = B(U)\mathbf{X} + \mathbf{C}(\mathbf{X}, \mathbf{X}, \mathbf{X}) \tag{4.10}$$

where $\mathbf{C}(\mathbf{X},\mathbf{X},\mathbf{X})$ is a cubic vector function of the state variables and

$$B(U)=\begin{bmatrix} 0 & 1 & 0 & 0 & 0 \\ -\frac{I_\alpha k_{h0}}{d} & -(c_1+d_1U) & -(k_1U^2-\frac{m_W x_\alpha b k_{\alpha 0}}{d}) & -(c_2+d_2U) & -\theta_1 \\ 0 & 0 & 0 & 1 & 0 \\ \frac{m_W x_\alpha b k_{h0}}{d} & -(c_3+d_3U) & -(k_2U^2+\frac{k_{\alpha 0} m_T}{d}) & -(c_4+d_4U) & -\theta_2 \\ 0 & -\frac{\chi_1}{C_p} & 0 & 0 & -\frac{1}{RC_p} \end{bmatrix}$$

4.2 Linear Analysis

The matrix $B(U)$ has a set of five eigenvalues λ_i, $i=1,2...,5$. The four first eigenvalues are similar to those of a pure aeroelastic system in the absence of the piezoelectricity effect. The fifth eigenvalue is a result of the electromechanical coupling. This eigenvalue (λ_5) is always real negative as in the case of piezoelectric systems subjected to base excitations. The first four eigenvalues are complex conjugates ($\lambda_2=\overline{\lambda_1}$ and $\lambda_4=\overline{\lambda_3}$). The real parts of these eigenvalues represent the damping coefficients and the positive imaginary parts correspond to the global frequencies of the piezoaeroelastic system. Because λ_5 is always real negative, the stability of the trivial solution, equation (4.10), depends only on the first four eigenvalues. The solution of the linear part is asymptotically stable if the real parts of all λ_i's are negative. On the other hand, if one of the real parts is positive, the solution of the linearized system is unstable. The speed U_f, for which one or more eigenvalues have zero real parts, corresponds to the onset of the instability and is termed the flutter speed.

A piezoaeroelastic energy harvester should be designed to attain limit-cycle oscillations (LCO) at the lowest possible freestream velocity. The choice of the linear coefficients of the springs plays an important role in determining the flutter speed U_f. Figure 4.2-a shows that, by varying the linear torsional spring coefficient, there is a value for which the flutter speed is a minimum. Figure 4.2-b presents similar results for the linear flexural spring coefficient. Clearly, it is possible to choose linear spring coefficients that enable energy harvesting at minimal speeds.

Figure 4.3-a shows that the flutter speed is slightly dependent on the load resistance. This can be noted better in Figure 4.3-b which shows the percentage increase in the flutter speed as function of the load resistance. Two different regions are noted. Up to $10^5\Omega$, the

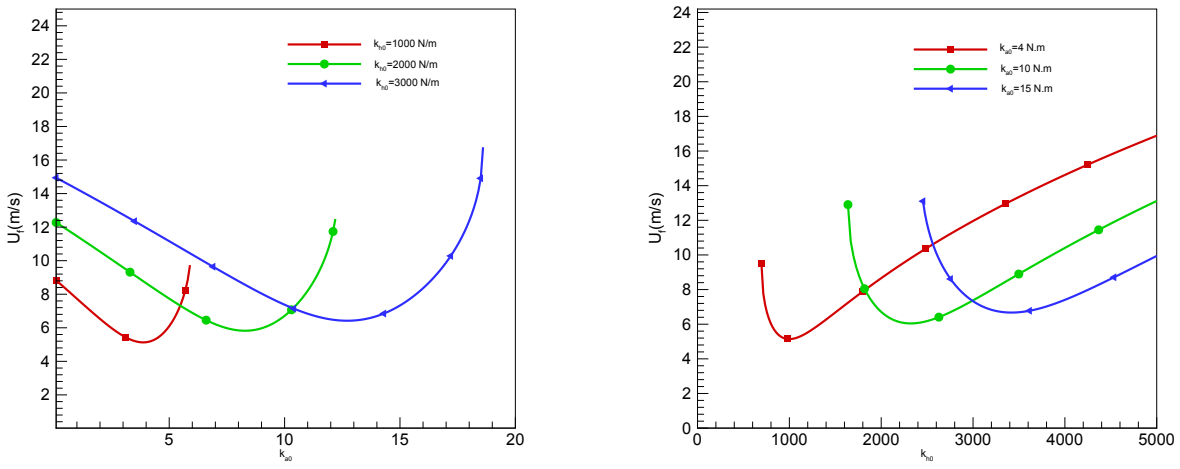

(a) (b)

Figure 4.2: Variations of the flutter speed U_f with (a) the torsional linear spring coefficient $k_{\alpha 0}$ and (b) the plunge linear spring coefficient k_{h0}

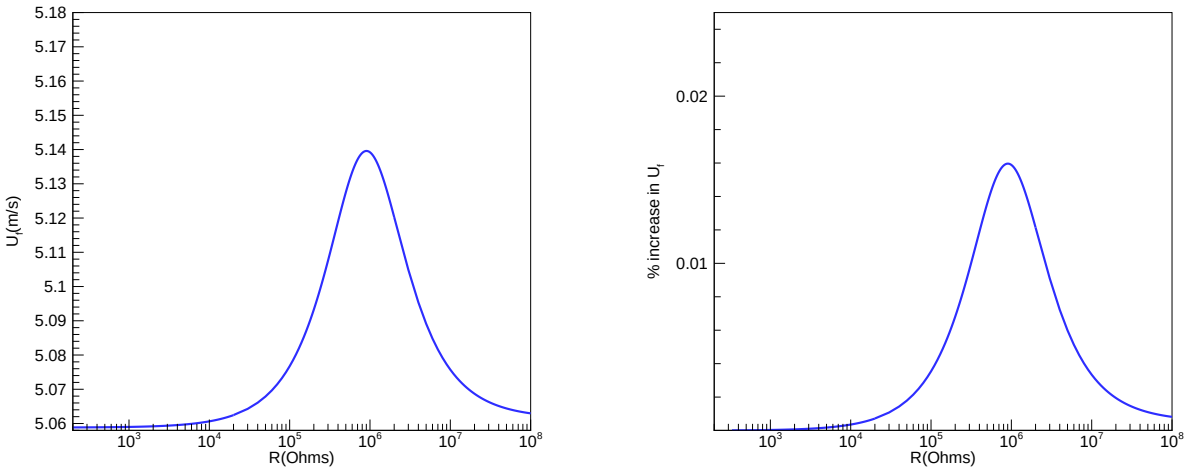

(a) (b)

Figure 4.3: (a) Variations of the flutter speed U_f with the load resistance R and (b) percentage increase in the flutter speed U_f with increasing the load resistance R when $k_{\alpha 0} = 4N.m$ and $k_{h0} = 1000N/m$

flutter speed varies slightly with the load resistance. Between $10^5\Omega$ and $10^7\Omega$, the flutter speed increases more rapidly as the load resistance is increased.

4.3 Nonlinear Analysis

4.3.1 Normal form of Hopf bifurcation

Next, we derive the normal form of the dynamics of the piezoaeroelastic system near the flutter speed U_f. To this end, we add a perturbation term $\sigma_U U_f$ to the flutter speed and hence express the air speed as $U = U_f + \sigma_U U_f$. Then, the matrix $B(U)$ can be expressed as

$$B(U) = B(U_f) + \sigma_U B_1(U_f)$$

where

$$B_1(U_f) = \begin{bmatrix} 0 & 0 & 0 & 0 & 0 \\ 0 & -d_1 U_f & -2k_1 U_f^2 & -d_2 U_f & 0 \\ 0 & 0 & 0 & 0 & 0 \\ 0 & -d_3 U_f & -2k_2 U_f^2 & -d_4 U_f & 0 \\ 0 & 0 & 0 & 0 & 0 \end{bmatrix}$$

We rewrite equation (4.9) as

$$\dot{\mathbf{X}} = B(U_f)\mathbf{X} + \sigma_U B_1(U_f)\mathbf{X} + \mathbf{C}(\mathbf{X}, \mathbf{X}, \mathbf{X}) \tag{4.11}$$

where

$$\mathbf{C}^T = \begin{bmatrix} 0, C_2, 0, C_4, 0 \end{bmatrix}$$

We let G be the matrix whose columns are the eigenvectors of the matrix $B(U_f)$ corresponding to the eigenvalues $\pm j\omega_1 - \mu_1$, $\pm j\omega_2$, and $-\mu_5$, define a new vector $\mathbf{Y}$ such that $\mathbf{X} = G\mathbf{Y}$, and rewrite equation (4.11) as

$$G\dot{\mathbf{Y}} = B(U_f)G\mathbf{Y} + \sigma_U B_1(U_f)G\mathbf{Y} + \mathbf{C}(G\mathbf{Y}, G\mathbf{Y}, G\mathbf{Y}) \tag{4.12}$$

Multiplying equation (4.12) from the left by the inverse G^{-1} of G yields

$$\dot{\mathbf{Y}} = J\mathbf{Y} + \sigma_U K\mathbf{Y} + G^{-1}\mathbf{C}(G\mathbf{Y}, G\mathbf{Y}, G\mathbf{Y}) \tag{4.13}$$

where $J = G^{-1}B(U_f)G$ is a diagonal matrix whose elements are the eigenvalues $\pm j\omega_1 - \mu_1$, $\pm j\omega_2$, and $-\mu_5$ and $K = G^{-1}B_1(U_f)G$. We note that $Y_2 = \overline{Y_1}$, $Y_4 = \overline{Y_3}$, and hence equation (4.13) can be written in a component form as

$$\dot{Y_1} = j\omega_1 Y_1 - \mu_1 Y_1 + \sigma_U \sum_1^5 K_{1i} Y_i + N_1(\mathbf{Y}) \tag{4.14}$$

$$\dot{Y_3} = j\omega_2 Y_3 + \sigma_U \sum_1^5 K_{3i} Y_i + N_3(\mathbf{Y}) \tag{4.15}$$

$$\dot{Y_5} = -\mu_5 Y_5 + \sigma_U \sum_1^5 K_{5i} Y_i + N_5(\mathbf{Y}) \tag{4.16}$$

where the $N_i(\mathbf{Y})$ are tri-linear functions of the components of $\mathbf{Y}$.

According to the Center-Manifold theorem, there exists a center manifold

$$Y_1 = H_1(Y_3, \bar{Y}_3), \;\; \bar{Y}_1 = \bar{H}_1(Y_3, \bar{Y}_3), \;\; Y_5 = H_5(Y_3, \bar{Y}_3)$$

Moreover, the dynamics of the system are similar to those on this center manifold; that is,

$$\begin{aligned} \dot{Y_3} = j\omega_2 Y_3 \quad &+\sigma_U \left(K_{31}H_1 + K_{32}\bar{H}_1 + K_{33}Y_3 + K_{34}\bar{Y}_3 + K_{35}H_5\right) \\ &+N_3(H_1, \bar{H}_1, Y_3, \bar{Y}_3, H_5) \end{aligned} \tag{4.17}$$

Because σ_U is small and N_1 and N_5 are cubic functions of the components of $\mathbf{Y}$, H_1 and H_5 are zero to the third approximation. Therefore, keeping only the resonance terms in equation (4.17)(202), we obtain the complex-valued normal form

$$\dot{Y_3} = j\omega_2 Y_3 + \sigma_U K_{33} Y_3 + \alpha_e Y_3^2 \bar{Y}_3 \tag{4.18}$$

where α_e depends on the cubic nonlinear spring coefficients (k_{α_2} and k_{h2}) as shown in Table 4.1 for the two considered configurations.

Next, we express Y_3 in the polar form

$$Y_3 = \frac{1}{2} a e^{j(\omega_2 t + \gamma)} \tag{4.19}$$

where a is the amplitude of oscillations and γ is its phase. Substituting equation (4.20) into equation (4.18) and separating the real and imaginary parts, we obtain the following

Table 4.1: Parameters of the two considered configurations when $R = 10^6\Omega$ and $c_s = 10.833$

	First configuration	Second configuration
$k_{\alpha 0}$	4	6.833
k_{h0}	1000	2844.4
U_f	5.13	9.18
β_r	0.94 σ_U	4.22 σ_U
β_i	0.75 σ_U	2.89 σ_U
α_{er}	-2.11 10^{-5}- 1.17 10^{-13} k_{h2} - 1.82 10^{-7} $k_{\alpha 2}$	-4.61 10^{-5} - 3.52 10^{-11} k_{h2}+ 9.04 10^{-7} $k_{\alpha 2}$
α_{ei}	-3 10^{-5}+ 4.06 10^{-11} k_{h2} + 5.30 10^{-6} $k_{\alpha 2}$	-4 10^{-5} + 1.25 10^{-11} k_{h2} + 1.55 10^{-6} $k_{\alpha 2}$

real-valued normal form of the Hopf bifurcation:

$$\dot{a} = \beta_r a + \frac{1}{4}\alpha_{er} a^3 \tag{4.20}$$

$$\dot{\gamma} = \beta_i + \frac{1}{4}\alpha_{ei} a^2 \tag{4.21}$$

where $\beta = \sigma_U K_{33}$ and the subscripts r and i denote the real and imaginary parts, respectively.

Equation (4.20) has the three equilibrium solutions:

$$a = 0 \text{ and } a = \pm\sqrt{\frac{-4\beta_r}{\alpha_{er}}}$$

where $a = 0$ is the trivial solution. The other solutions are nontrivial. The origin is asymptotically stable for $\beta_r < 0$ or $\beta_r = 0$ and $\alpha_{er} < 0$, unstable for $\beta_r > 0$ or $\beta_r = 0$ and $\alpha_{er} > 0$. The nontrivial solutions exist when $\beta_r \alpha_{er} < 0$. They are stable (supercritical Hopf bifurcation) for $\beta_r > 0$ and $\alpha_{er} < 0$ and unstable (subcritical Hopf bifurcation) for $\beta_r < 0$ and $\alpha_{er} > 0$.

We consider the two configurations presented in Table 4.1.

4.4 Results and Discussions

4.4.1 Comparison between normal form of Hopf bifurcation and numerical integration

To check the accuracy of the analytical solution derived by the normal form of the Hopf bifurcation, we compare the amplitude of the harvested power, voltage output, pitch, and plunge with values obtained from numerical integration of equations (4.9). Using the normal form, we find that the amplitudes of the LCO for the harvested power (P), voltage output (V), pitch (A_α), and plunge (A_h) are given by:

$$A_h = a\sqrt{G[1,3]_r^2 + G[1,3]_i^2} \tag{4.22}$$

$$A_\alpha = a\sqrt{G[3,3]_r^2 + G[3,3]_i^2} \tag{4.23}$$

$$V = a\sqrt{G[5,3]_r^2 + G[5,3]_i^2} \tag{4.24}$$

$$P = \frac{V^2}{R} \tag{4.25}$$

where $(.)_r$ and $(.)_i$ denote the real part and imaginary part, respectively. Figure 4.4 shows a comparison of these outputs for the second configuration as presented in Table 4.1 when $k_{\alpha_2} = 0N.m$ and $k_{h2} = 67.685N/m$. This configuration yields a supercritical instability ($\alpha_{er} < 0$). The results show good agreement between the amplitudes of LCO near the bifurcation. As expected and because the normal form is applicable only near the onset of the bifurcation, we note a relatively larger disagreement of the outputs as the freestream velocity increases further beyond the flutter speed.

4.4.2 Effect of the nonlinear torsional spring coefficient on the system behavior

The amplitude of the harvested power depends on the cubic nonlinearities of the system which are represented by the parameters c_s, $k_{\alpha 2}$, and k_{h2}. Here, we consider the nonlinear aerodynamic coefficient c_s as constant and set it equal to 10.833 (with stall). As can be deduced from Table 4.1, the sensitivity of the system outputs to variations in the nonlinear torsional spring coefficient is much higher than the sensitivity to variations in the nonlinear flexural spring coefficient. Furthermore and considering the signs of α_{er} and β_r in the same

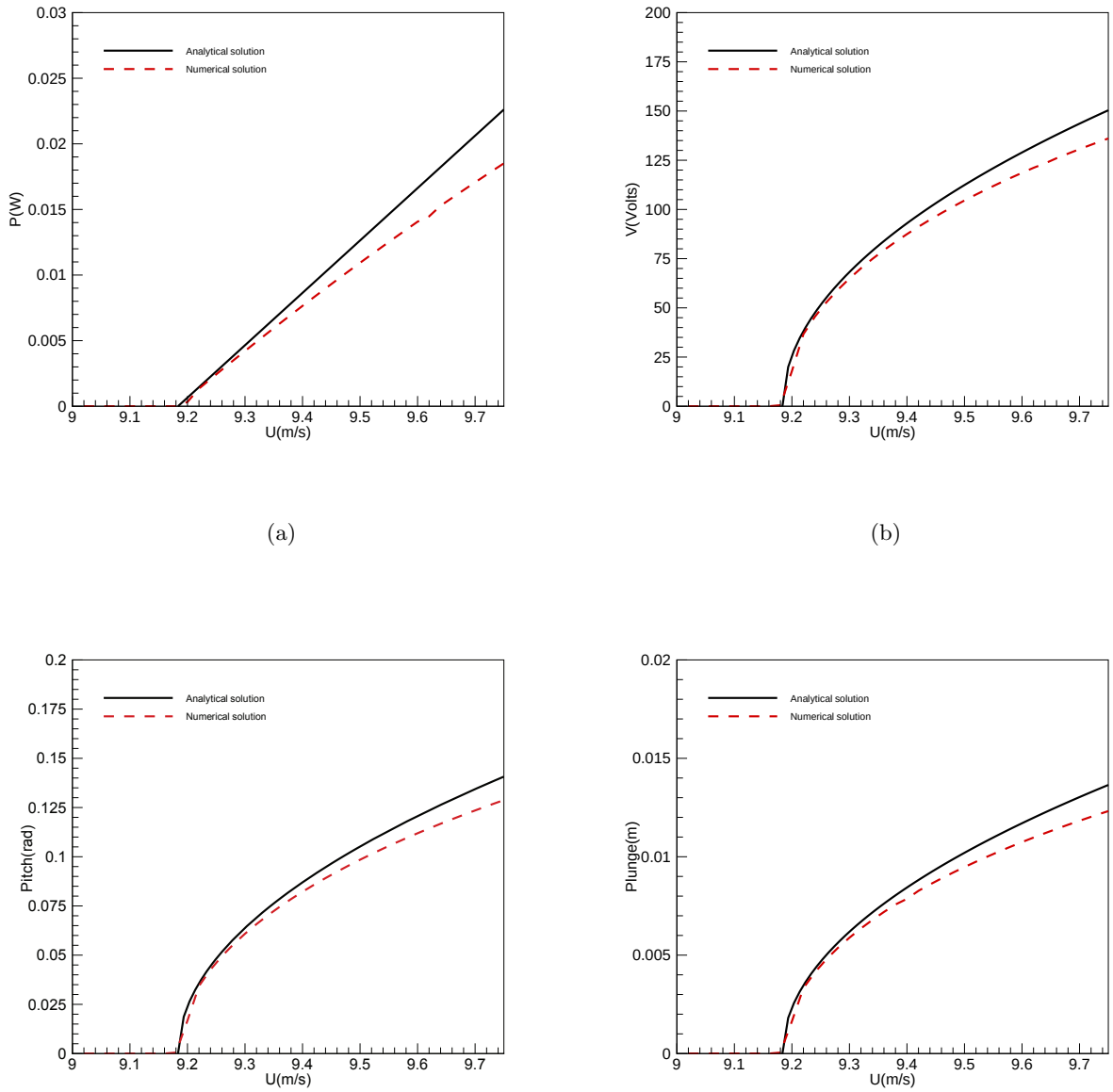

Figure 4.4: Comparison between the analytical prediction using the normal form and numerical integration of the variation of the harvested power (a), voltage output (b), pitch (c), and plunge (d) with the freestream velocity when $R = 10^6\Omega$ and $k_{\alpha_2} = 0N.m$ for the second configuration

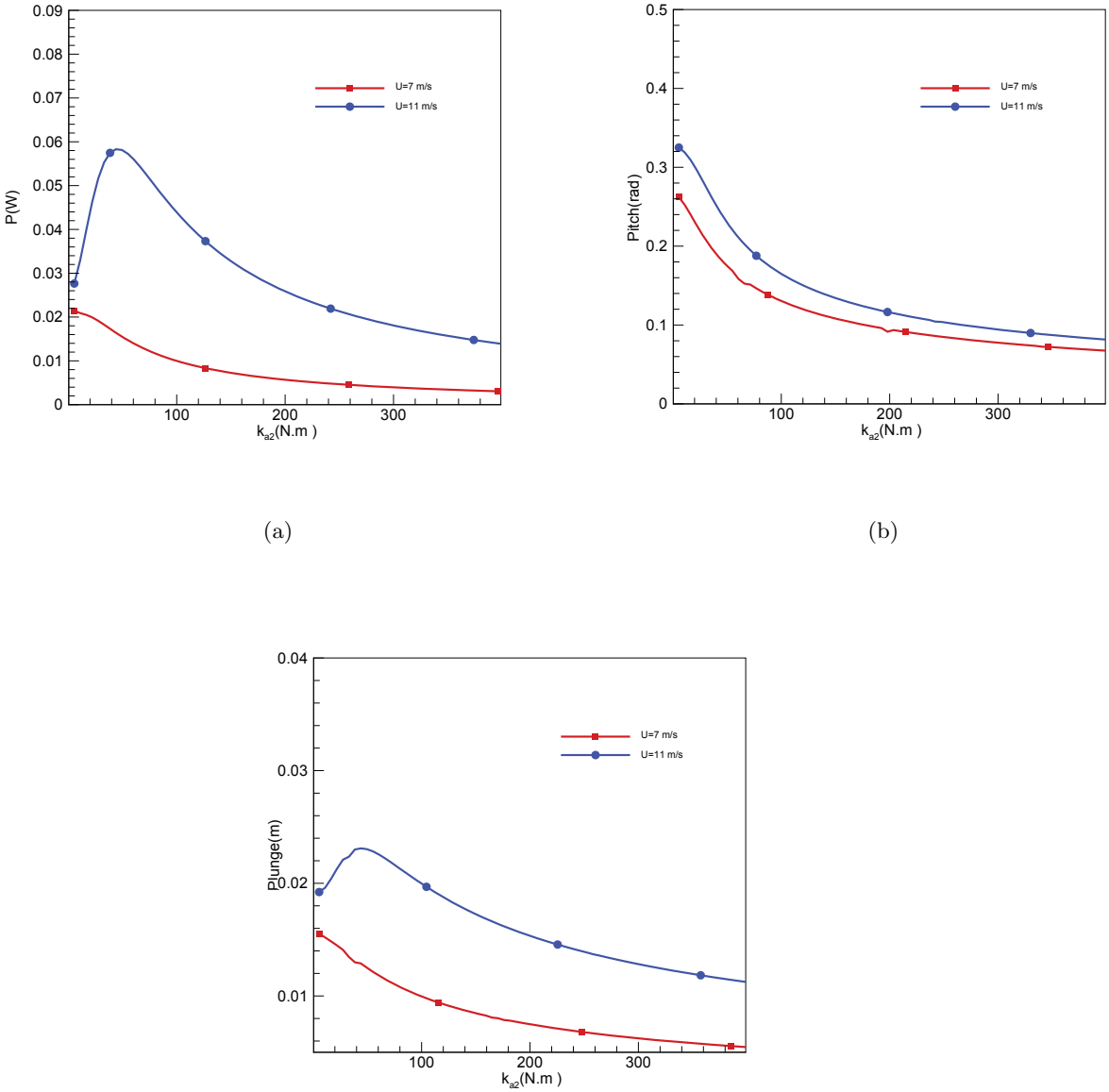

Figure 4.5: Variations of the harvested power (a), pitch (b), and plunge (c) of the first configuration with $k_{\alpha 2}$ for two different values of the freestream velocity when $R = 10^6\Omega$

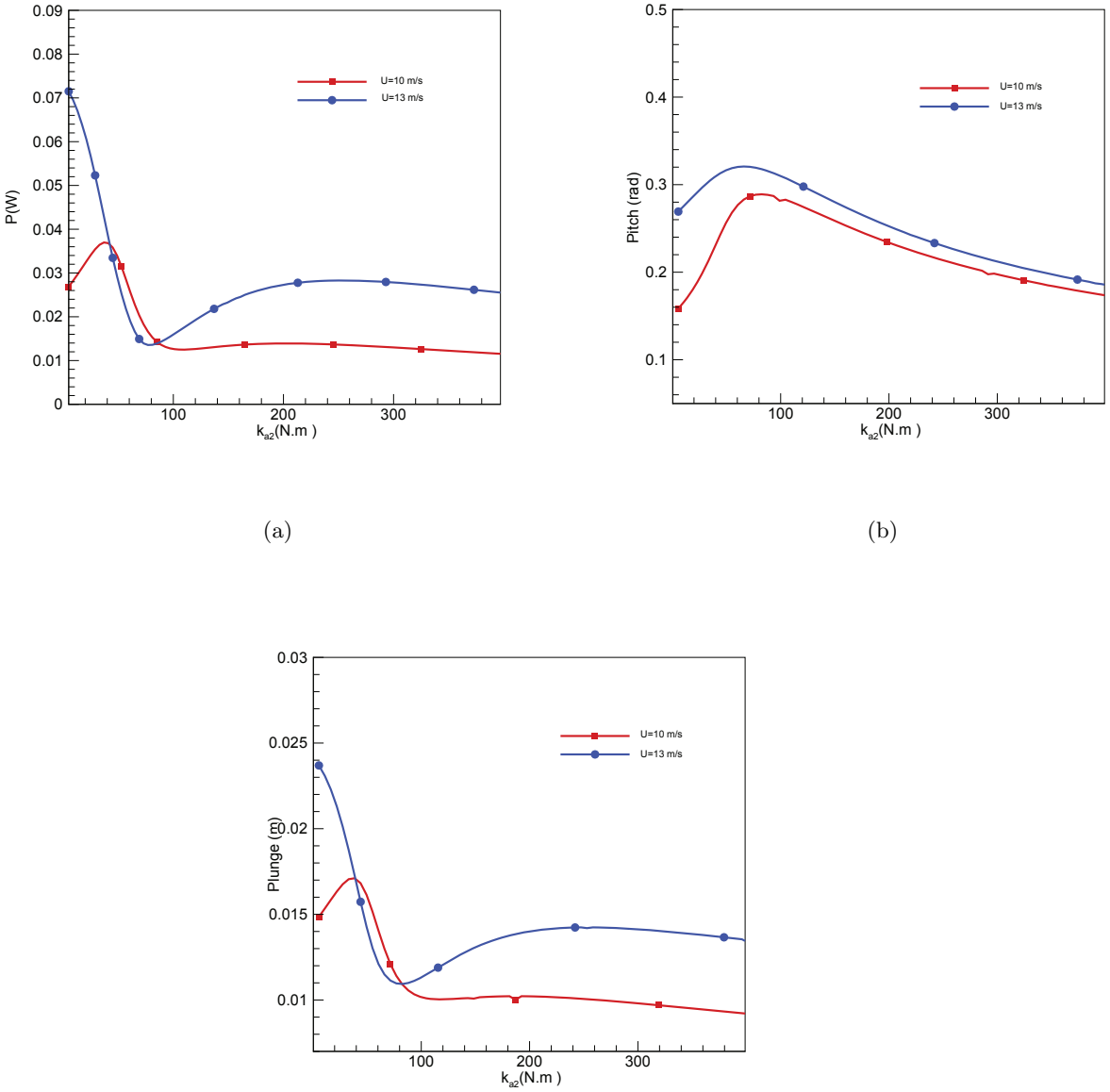

(a) (b)

(c)

Figure 4.6: Variations of the harvested power (a), pitch (b), and plunge (c) of the second configuration with $k_{\alpha 2}$ for two different values of the freestream velocity when $R = 10^6\Omega$

table, it is clear that the first configuration will always yield a supercritical instability. In contrast, variations in $k_{\alpha 2}$ lead to a change in the instability from supercritical to subcritical. As such, the normal form is helpful in deciding which parameters would affect the instability and in what aspect.

In this section, we consider the specific values given in (201) and vary the nonlinear torsional spring coefficient ($k_{\alpha 2}$) for two different values of the linear spring coefficients (k_{α_0} and k_{h0}). We then perform a numerical integration to determine the system outputs at two different freestream velocities near and larger than the flutter speed. The results are plotted in Figures 4.5 and 4.6 for the first and second configurations, respectively. The curves in these figures show the effects of the nonlinear torsional spring coefficient $k_{\alpha 2}$ on the harvested power and pitch and plunge amplitudes for the two configurations. As expected from the normal form, the system's output for the first configuration near the flutter speed is maximum when $k_{\alpha 2} = 0N.m$ because this value minimizes α_{er}. Away from the flutter speed, the maximum values of the plunge motion and harvested power are obtained when $k_{\alpha 2} \approx 50$ N.m. As for the second configuration, the results plotted in Figure 4.6 show that the maximum output near the flutter speed is obtained when $k_{\alpha 2} \approx 50$ N.m. This is also expected because of the difference in the signs of the components contributing to α_{er}, as shown in Table 4.1. Away from the flutter speed, the maximum output power is obtained when $k_{\alpha 2} = 0N.m$. Clearly, the choice of $k_{\alpha 2}$ plays an important role in determining the maximum harvested power.

4.4.3 Effect of the flutter speed and the load resistance on the system outputs

Variations of the system's outputs with the freestream velocity for different values of the electrical load resistance for the first configuration are considered next. Figures 4.7 and 4.8 show these variations for $k_{\alpha 2} = 0N.m$ and $50N.m$. As mentioned before, we always have a supercritical Hopf bifurcation for this configuration. This is again obvious in these figures. The results show that there is an optimal value for the load resistance that yields the highest power. This is similar to observations made in base excitation energy harvesters. In contrast, the voltage output continuously increases when increasing the electrical load resistance. In addition, we note that the harvested power and voltage increase when the freestream velocity

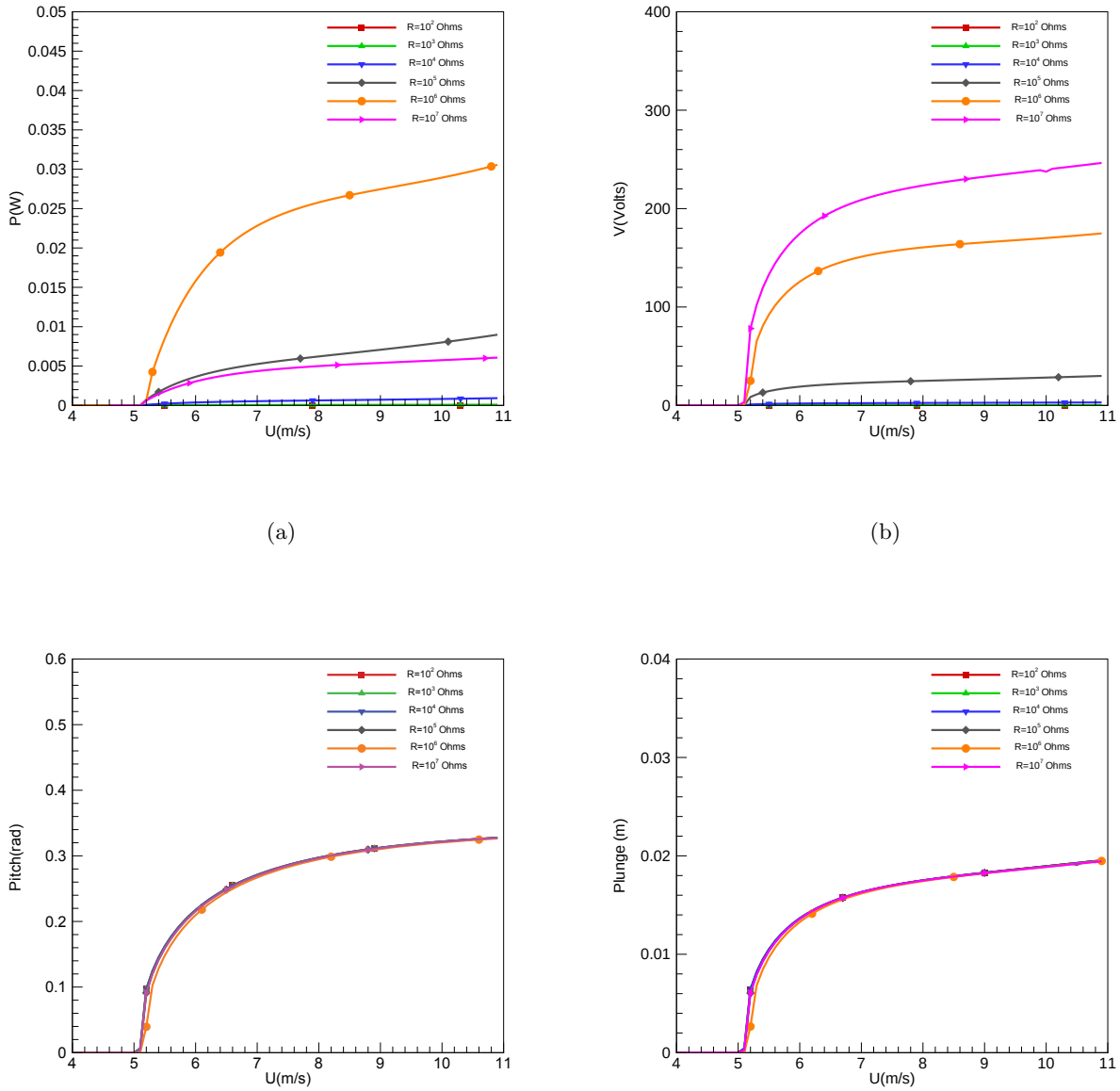

(a) (b)

(c) (d)

Figure 4.7: Variations of the harvested power (a), voltage output (b), pitch (c), and plunge (d) of the first configuration with the freestream velocity for different values of the load resistance when $k_{\alpha 2} = 0 N.m$

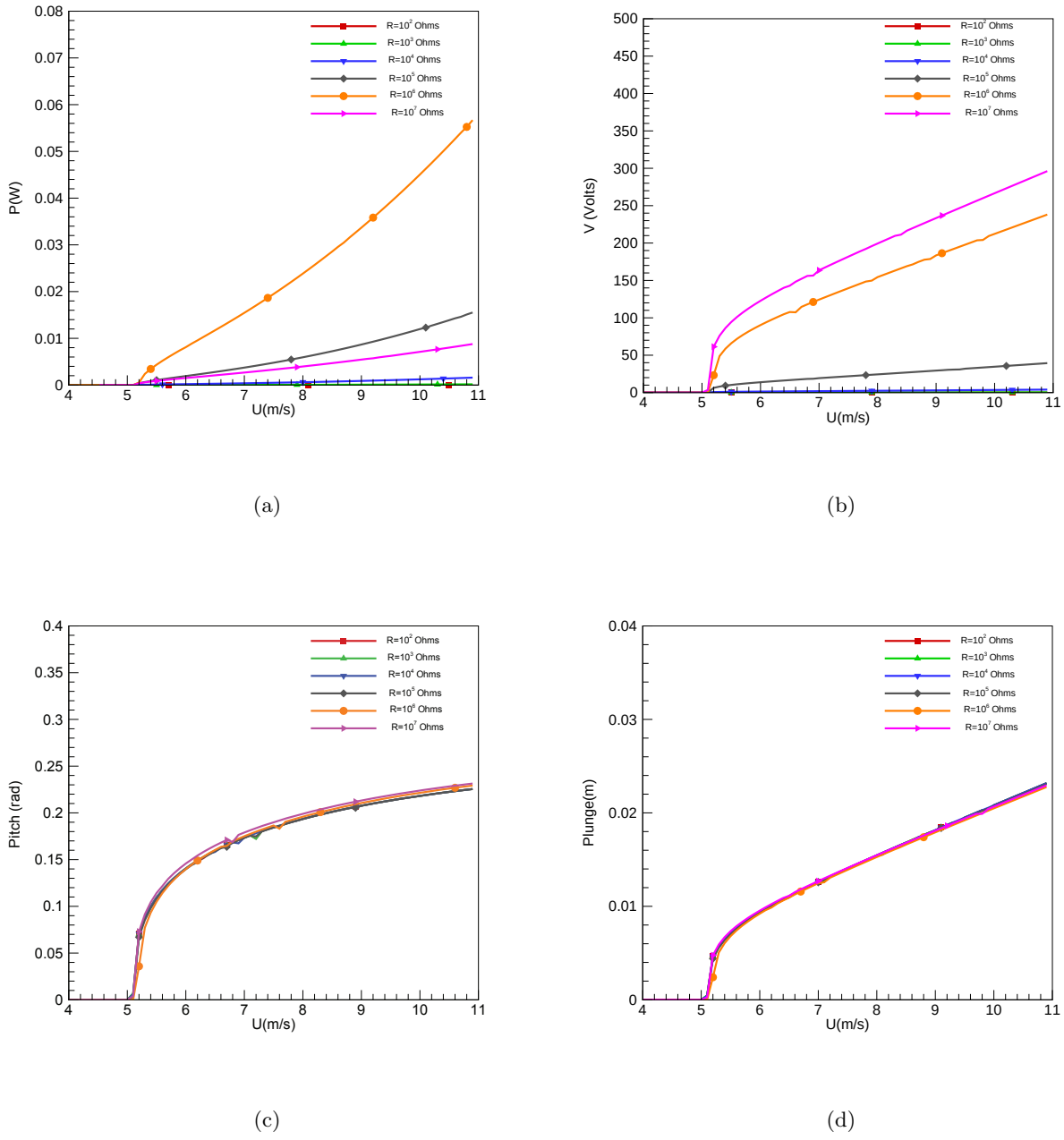

Figure 4.8: Variations of the harvested power (a), voltage output (b), pitch (c), and plunge (d) of the first configuration with the freestream velocity for different values of the load resistance when $k_{\alpha 2} = 50N.m$

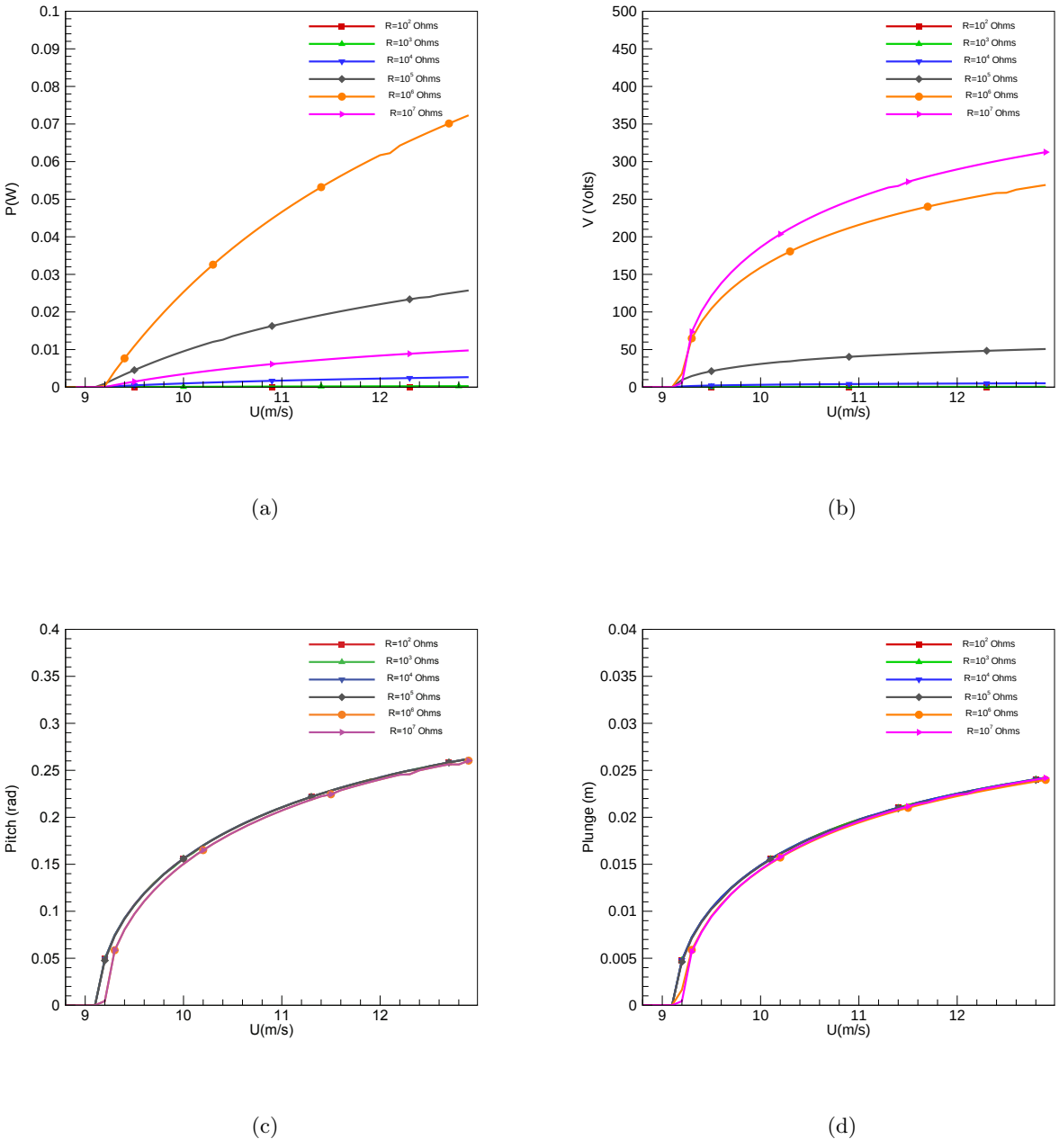

(a) (b)

(c) (d)

Figure 4.9: Variations of the harvested power (a), voltage output (b), pitch (c), and plunge (d) of the second configuration with the freestream velocity for different values of the load resistance when $k_{\alpha 2} = 0 N.m$

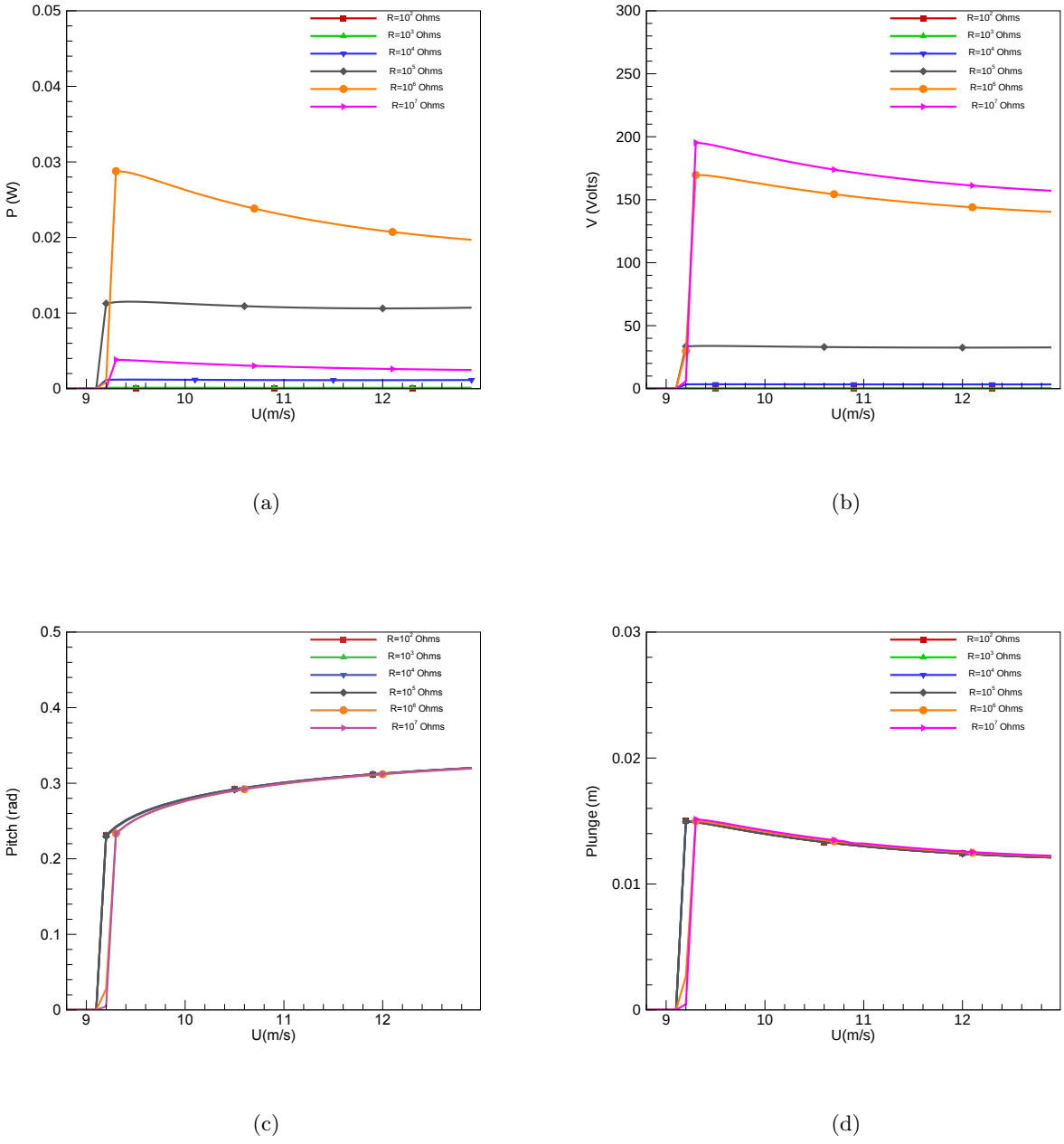

(a) (b)

(c) (d)

Figure 4.10: Variations of the harvested power (a), voltage output (b), pitch (c), and plunge (d) of the second configuration with the freestream velocity for different values of the load resistance when $k_{\alpha 2} = 60N.m$

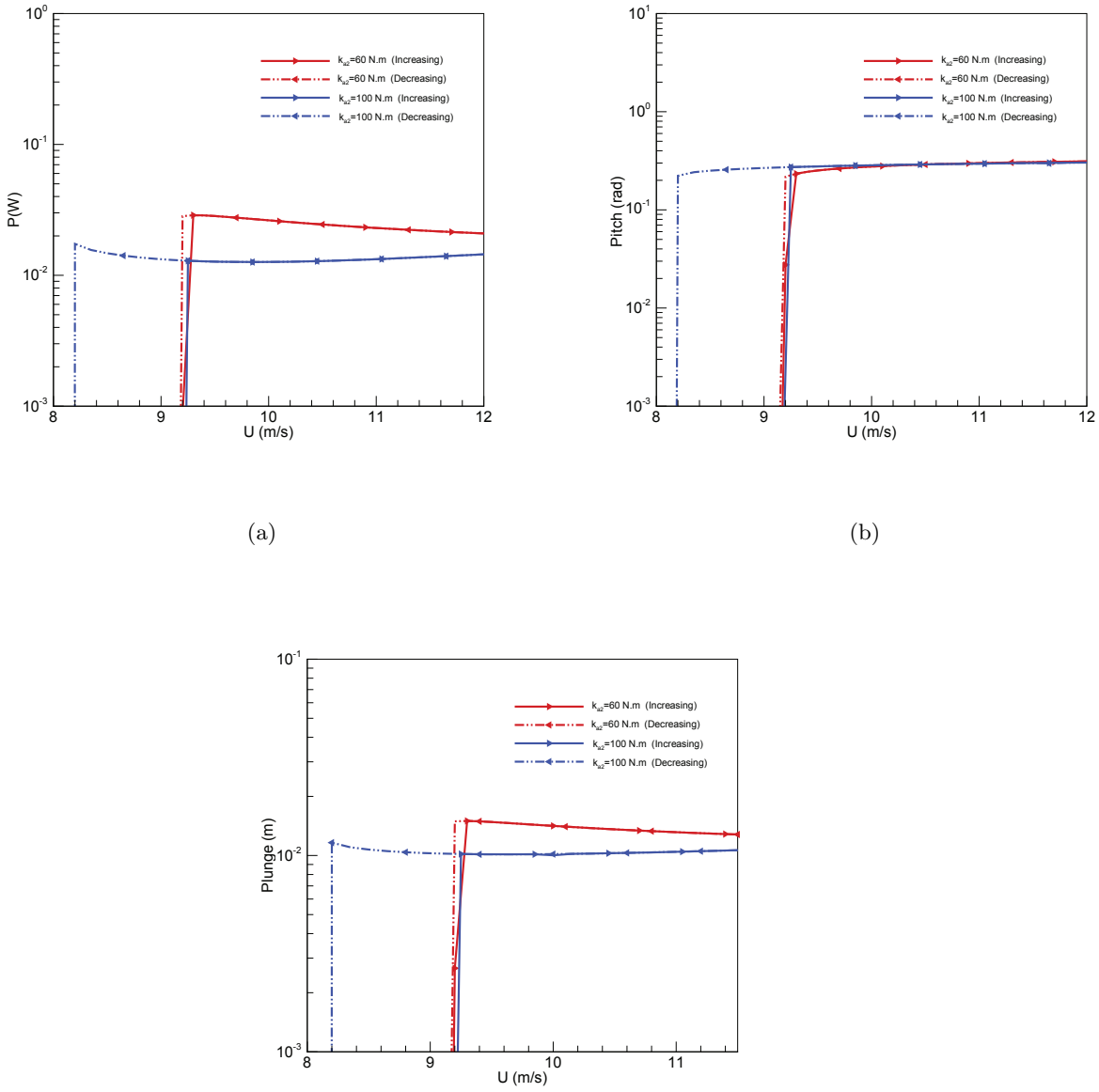

(a)

(b)

(c)

Figure 4.11: Subcritical Hopf bifurcation characteristics of the second configuration for various values of $k_{\alpha 2}$ when $R = 10^6\Omega$

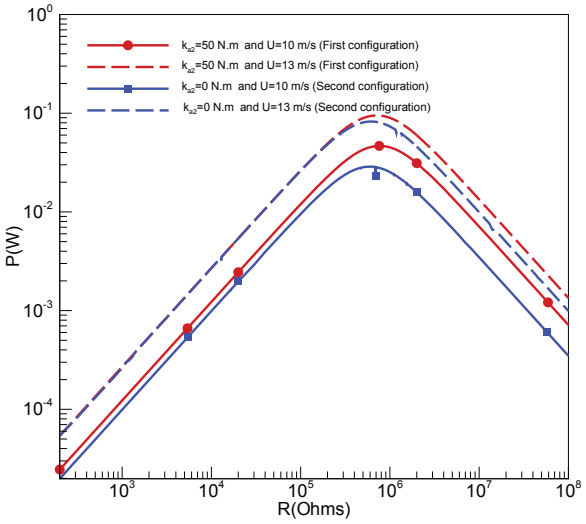

Figure 4.12: Variation of the harvested power with the load resistance for various values of the freestream velocity for both configurations

is increased. The load resistance has a very limited effect on the amplitudes of the pitch and plunge.

Variations in the system's output of the second configuration as a function of the freestream velocity for different values of the load resistance and for two distinct values of $k_{\alpha 2}$, are shown in Figures 4.9 and 4.10. When $k_{\alpha 2}$= 0 $N.m$, the instability is supercritical, as shown in Figure 4.9, and variations in the output response are similar to those of the first configuration. When $k_{\alpha 2}$ is set equal to 60 $N.m$, the instability is subcritical, as shown in Figure 4.10. Variations of the output power and voltage with the load resistance are similar to variations observed in the other configurations. On the other hand, we observe that increasing the freestream velocity causes a reduction in the output voltage, and power, and plunge amplitude.

To further characterize the subcritical behavior of the second configuration, we examine the effects of the nonlinear torsional spring coefficient on its outputs. As shown in Figure 4.11, increasing $k_{\alpha 2}$ to $100N.m$ yields a slight decrease in the harvested power and plunge. Furthermore, it lowers the velocity of the subcritical instability. A comparison of the perfor-

mances of the two configurations under different values for the electrical load resistance and two freestream velocities are shown in Figure 4.12. The plots show that there is an optimal load resistance for which harvested energy is maximum. For both configurations, we note that this value is $\approx 10^6\Omega$. Additionally, for the same freestream velocities, $U = 10m/s$ and $U = 13m/s$, the harvested power of the first configuration is larger than that of the second configuration. This is because the flutter speed of the first configuration is smaller than that of the second configuration.

4.5 Conclusions

In this chapter, an investigation of a piezoaeroelastic energy harvester is conducted using the method of normal form and numerical integration of the governing equations. The analytical and numerical predictions are in good agreement near the bifurcation. The normal form allowed us to ascertain the effects of the linear and nonlinear spring coefficients on the harvested power and generated voltage. It is found that the torsional spring has the most influence and can change the instability from supercritical to subcritical. The effect of the electrical load resistance on the flutter speed and pitch and plunge is negligible. On the other hand, it affects the output voltage and power. More specifically, the output power is maximum for a specific load resistance. In comparison, the voltage increases with increasing the load resistance. Based on these results, we have characterized the subcritical behavior of the harvester and determined optimal values of the load resistance that yield maximum harvested power.

Chapter 5

Design of Piezoaeroelastic Energy Harvesters

As mentioned in the preceding chapter, for the purpose of energy harvesting, it is important to generate energy at low wind speed and hence to decrease the flutter speed. Yet, this reduction should not be accompanied by subcritical Hopf bifurcations, which can damage the aeroelastic system. Therefore, our objective, here, is to design linear spring coefficients as well as linear velocity feedback to produce energy at any desired wind speed. Furthermore, we aim also to design nonlinear spring coefficients that increase the amplitudes of the ensuing limit-cycle oscillations and hence the level of the harvested power through supercritical Hopf bifurcations only.

The design problem is important because the harvester may undergo a secondary Hopf bifurcation at higher wind speeds. At these speeds, complex motions, are usually encountered. As such, it is necessary to evaluate the response characteristics and the level of the generated power at high wind speeds and design nonlinear springs to safely maximize the harvested power. To this end, we design a piezoaeroelastic energy harvester consisting of a rigid airfoil that is constrained to pitch and plunge and supported by linear and nonlinear torsional and flexural springs with a piezoelectric coupling attached to the plunge degree of freedom. We choose the linear springs to produce the minimum flutter speed and then implement a linear velocity feedback to reduce the flutter speed to any desired value and hence produce limit-

cycle oscillations at low wind speeds. Then, we derive the normal form of the Hopf bifurcation (flutter) and use it to choose nonlinear spring coefficients that produce supercritical Hopf bifurcations and increase the amplitudes of the ensuing limit cycles and hence the harvested power.

5.1 Representation of the Piezoaeroelastic System

We consider a harvester consisting of a rigid airfoil that is constrained to pitch and plunge, and supported by linear and nonlinear torsional and flexural springs with a piezoelectric coupling attached to the plunge degree of freedom.

For a given airfoil section, the flutter speed depends principally on the linear aerodynamic loads, the linear spring stiffnesses, and the damping coefficients. One can design the stiffnesses k_{h0} and $k_{\alpha 0}$ to optimize the minimum flutter speed. However, that is not necessary because one can design linear velocity feedback, which, in principle, could be used to reduce the flutter speed to any desired small value. To this end, we introduce the terms $-\kappa_h \dot{h}$ and $-\kappa_\alpha \dot{\alpha}$ into the governing equations of the piezoaeroelastic energy harvester and choose the gains κ_h and κ_α to control the flutter speed. This control can be implemented by sensing the velocities of both of the pitch and plunge (e.g., in the beam to which the piezoelectric harvester is attached). These signals are then fed to circuits whose outputs are amplified and sent to actuators. These actuators are then used to force the two motions, as shown in Figure 5.1, where K_1 and K_2 are used to represent the amplifiers for the pitch and plunge, respectively.

The equations of motion of this piezoaeroelastic energy harvester are then written as

$$m_T \ddot{h} + m_W x_\alpha b \ddot{\alpha} + (c_h - \kappa_h)\dot{h} + (k_{h0} + k_{h2} h^2) h - \theta V = -L \tag{5.1}$$

$$m_W x_\alpha b \ddot{h} + I_\alpha \ddot{\alpha} + (c_\alpha - \kappa_\alpha)\dot{\alpha} + (k_{\alpha 0} + k_{\alpha 2} \alpha^2)\alpha = M \tag{5.2}$$

$$C_p \dot{V} + \frac{V}{R} + \chi \dot{h} = 0 \tag{5.3}$$

where m_T is the total mass of the wing including its support structure; m_W is the wing mass alone; I_α is the mass moment of inertia about the elastic axis; b is the half chord length;

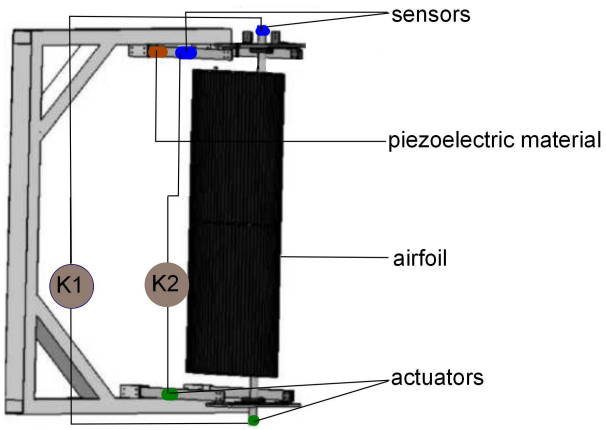

Figure 5.1: Sketch of the linear velocity feedback control

bx_α is the distance between the center of mass and the elastic axis; c_h and c_α are, respectively, the plunge and pitch structural damping coefficients; L and M are the aerodynamic lift and moment about the elastic axis; R is the load resistance; V is the voltage across this load resistance; C_p is the capacitance of the piezoelectric layer; θ and χ are electromechanical coupling terms; k_{h0} and $k_{\alpha 0}$ are the linear structural stiffnesses for the plunge and pitch degrees of freedom, respectively; and k_{h2} and $k_{\alpha 2}$ are, respectively, the nonlinear structural stiffnesses for the plunge and pitch degrees of freedom.

As in the preceding chapter, the aerodynamic loads are evaluated using a quasi-steady approximation with a stall model and written as

$$L = \rho U^2 b c_{l\alpha}(\alpha_{eff} - c_s \alpha_{eff}^3) \tag{5.4}$$

$$M = \rho U^2 b^2 c_{m\alpha}(\alpha_{eff} - c_s \alpha_{eff}^3) \tag{5.5}$$

where U is the freestream velocity, $c_{l\alpha}$ and $c_{m\alpha}$ are the aerodynamic lift and moment coefficients, and c_s is a nonlinear parameter associated with stall. The effective angle of attack due to the instantaneous motion of the airfoil is given by

$$\alpha_{eff} = \alpha + \frac{\dot{h}}{U} + (\frac{1}{2} - a) b \frac{\dot{\alpha}}{U}$$

We define the following state variables:

$$X = \begin{bmatrix} X_1 \\ X_2 \\ X_3 \\ X_4 \\ X_5 \end{bmatrix} = \begin{bmatrix} h \\ \dot{h} \\ \alpha \\ \dot{\alpha} \\ V \end{bmatrix} \tag{5.6}$$

and rewrite the equations of motion as

$$\dot{X}_1 = X_2 \tag{5.7}$$

$$\dot{X}_2 = -\frac{I_\alpha k_{h0}}{d} X_1 - (c_1 + d_1 U) X_2 - (k_1 U^2 - \frac{m_W x_\alpha b k_{\alpha 0}}{d}) X_3 - (c_2 + d_2 U) X_4 - \theta_1 X_5$$
$$-N_{1\alpha}(X) - N_{1h}(X) + N_{NL1}$$

$$\dot{X}_3 = X_4$$

$$\dot{X}_4 = \frac{m_W x_\alpha b k_{h0}}{d} X_1 - (c_3 + d_3 U) X_2 - (k_2 U^2 + \frac{k_{\alpha 0} m_T}{d}) X_3 - (c_4 + d_4 U) X_4 - \theta_2 X_5$$
$$-N_{2\alpha}(X) - N_{2h}(X) + N_{NL2}$$

$$\dot{X}_5 = -\frac{\chi_1}{C_p} X_2 - \frac{1}{R C_p} X_5$$

where

$$d = m_T I_\alpha - (m_w x_\alpha b)^2$$

$$c_1 = [I_\alpha (c_h - \kappa_h)]/d$$

$$d_1 = [I_\alpha \rho b c_{l\alpha} + \rho b^3 m_w x_\alpha c_{m\alpha}]/d$$

$$c_2 = [-m_w x_\alpha b (c_\alpha - \kappa_\alpha)]/d$$

$$d_2 = [I_\alpha \rho b^2 c_{l\alpha} (\tfrac{1}{2} - a) + m_w x_\alpha b^4 \rho c_{m\alpha} (\tfrac{1}{2} - a)]/d$$

$$c_3 = [-m_w x_\alpha b (c_h - \kappa_h)]/d$$

$$d_3 = [-m_w x_\alpha b \rho b c_{l\alpha} - m_T c_{m\alpha} \rho b^2]/d$$

$$c_4 = [m_T (c_\alpha - \kappa_\alpha)]/d$$

$$d_4 = [-m_T b^3 \rho c_{m\alpha} (\tfrac{1}{2} - a) - m_w x_\alpha b^3 \rho c_{l\alpha} (\tfrac{1}{2} - a)]/d$$

$$k_1 = [I_\alpha \rho b c_{l\alpha} + m_w x_\alpha b^3 \rho c_{m\alpha}]/d$$

$$k_2 = -[\rho b^2 c_{l\alpha} m_w x_\alpha + m_T \rho b^2 c_{m\alpha}]/d$$

$$N_{1h} = I_\alpha [k_{h2} X_1^3]/d$$

$$N_{1\alpha} = -m_w x_\alpha b [k_{\alpha 2} X_3^3]/d$$

$$N_{2h} = -m_w x_\alpha b [k_{h2} X_1^3]/d$$

$$N_{2\alpha} = m_T [k_{\alpha 2} X_3^3]/d$$

$$N_{NL1} = [\rho U^2 c_s b (c_{l\alpha} I_\alpha + m_w x_\alpha b^2 c_{m\alpha}) \alpha_{eff}(X)]/d$$

$$N_{NL2} = -[c_s \rho U^2 b^2 (c_{l\alpha} m_w x_\alpha + m_T c_{m\alpha}) \alpha_{eff}(X)]/d$$

In vector form, the equations of motion are expressed as

$$\dot{\mathbf{X}} = B(U)\mathbf{X} + \mathbf{C}(\mathbf{X}, \mathbf{X}, \mathbf{X}) \tag{5.8}$$

where $\mathbf{C}(\mathbf{X},\mathbf{X},\mathbf{X})$ is a cubic vector function of the state variables and

$$B(U)=\begin{bmatrix} 0 & 1 & 0 & 0 & 0 \\ -\frac{I_\alpha k_{h0}}{d} & -(c_1+d_1U) & -(k_1U^2-\frac{m_W x_\alpha b k_{\alpha 0}}{d}) & -(c_2+d_2U) & -\theta_1 \\ 0 & 0 & 0 & 1 & 0 \\ \frac{m_W x_\alpha b k_{h0}}{d} & -(c_3+d_3U) & -(k_2U^2+\frac{k_{\alpha 0} m_T}{d}) & -(c_4+d_4U) & -\theta_2 \\ 0 & -\frac{\chi_1}{C_p} & 0 & 0 & -\frac{1}{RC_p} \end{bmatrix}$$

The matrix $B(U)$ has a set of five eigenvalues λ_i, $i=1,2...,5$, which determine the stability of the trivial solution of equation (5.8). We arrange these eigenvalues so that the first four are complex conjugates ($\lambda_2=\overline{\lambda_1}$ and $\lambda_4=\overline{\lambda_3}$). In the absence of the piezoelectricity effect, these eigenvalues are the same as those of the aeroelastic system. The fifth eigenvalue, which is always negative, is a result of the electromechanical coupling. If the real parts of all of the eigenvalues are negative, the trivial solution is asymptotically stable. On the other hand, if one of the real parts is positive, the trivial solution is unstable. In addition, the real parts of these eigenvalues represent the global damping and the positive imaginary parts correspond to the global frequencies of the piezoaeroelastic system. The speed for which one or more eigenvalues have zero real parts, corresponds to the onset of linear instability and is termed the flutter speed U_f.

5.2 Design of Flutter Speed

Our objective is to design piezoaeroelastic systems that can attain limit-cycle oscillations and hence harvest energy at the lowest wind speeds. To this end, we need to design aeroelastic harvesters that flutter at low wind speeds. The flutter speed depends on the effective damping, which is a combination of structural damping (which is positive) and aerodynamic damping (which is negative). The trivial equilibrium configuration is stable or unstable (i.e., flutter occurs) depending on whether the effective damping is positive or negative. The aerodynamic damping depends on the linear coefficients of the springs and the wind speed. For a desired flutter speed, we investigate next the design of the linear spring coefficients and a linear velocity feedback.

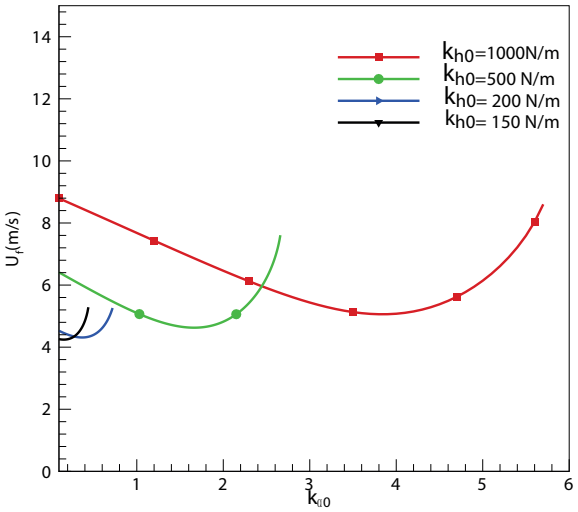

Figure 5.2: Variation of the flutter speed with the linear spring coefficients when $R = 10^5\Omega$

5.2.1 Design of linear spring coefficients

In the preceding chapter, we demonstrated that the choice of the linear spring coefficients plays an important role in determining the flutter speed. In addition, we showed that these coefficients can be optimized to minimize the flutter speed. In this chapter, we consider four configurations that are based on the parameters presented by Strganac et al. (201) and allow for variations in the linear spring coefficients. Table 5.1 shows the optimized coefficients and the corresponding flutter speeds for these configurations as determined from Figure 5.2. We note that decreasing the linear coefficient of the flexural spring leads to a decrease in the optimum linear coefficient of the torsional spring and in the flutter speed.

We note that these configurations are not optimal for energy harvesting because of the relatively high structural damping. Therefore, one would design aeroelastic harvesters with as small as possible structural damping and hence a small flutter speed. To lower the flutter speed further, we investigate next the use of linear velocity feedback control.

Table 5.1: Parameters of the four considered configurations

	First configuration	Second configuration	Third configuration	Fourth configuration
$k_{\alpha 0}(N.m)$	3.75	1.65	0.35	0.16
$k_{h0}(N/m)$	1000	500	200	150
$U_f(m/s)$	5.07	4.62	4.31	4.24

Table 5.2: Flutter speed of the first configuration for different feedback gains

	Configuration 5	Configuration 6	Configuration 7
κ_h	29.63	29.13	28.59
κ_α	0	0.01	0.02
$U_f(m/s)$	0.025	0.026	0.0017

5.2.2 Linear velocity feedback control

To reduce the flutter speed further, one needs to reduce the damping. For a given system with set structural damping, one can reduce the flutter speed to any desired small value by using linear velocity feedback control. This can be achieved through a feedback that is proportional to the plunge velocity, the pitch velocity, or both. In Figure 5.3, we show representative results in which we consider pitch gains of 0, 0.01, and 0.02 and vary the plunge gain for the first, second, and third configurations of Table 5.1. Figure 5.3-a shows that the gains, in the first configuration, can be chosen to reduce the flutter speed to any desired value. In Table 5.2, we show the flutter speed that can be attained using the first configuration with different gains. We refer to these configurations, which include the velocity feedback controllers and gains, as configurations 5, 6, and 7. Further assessment of the effects of these gains on the overall (including nonlinear) performance of the piezoaeroelastic system is presented below.

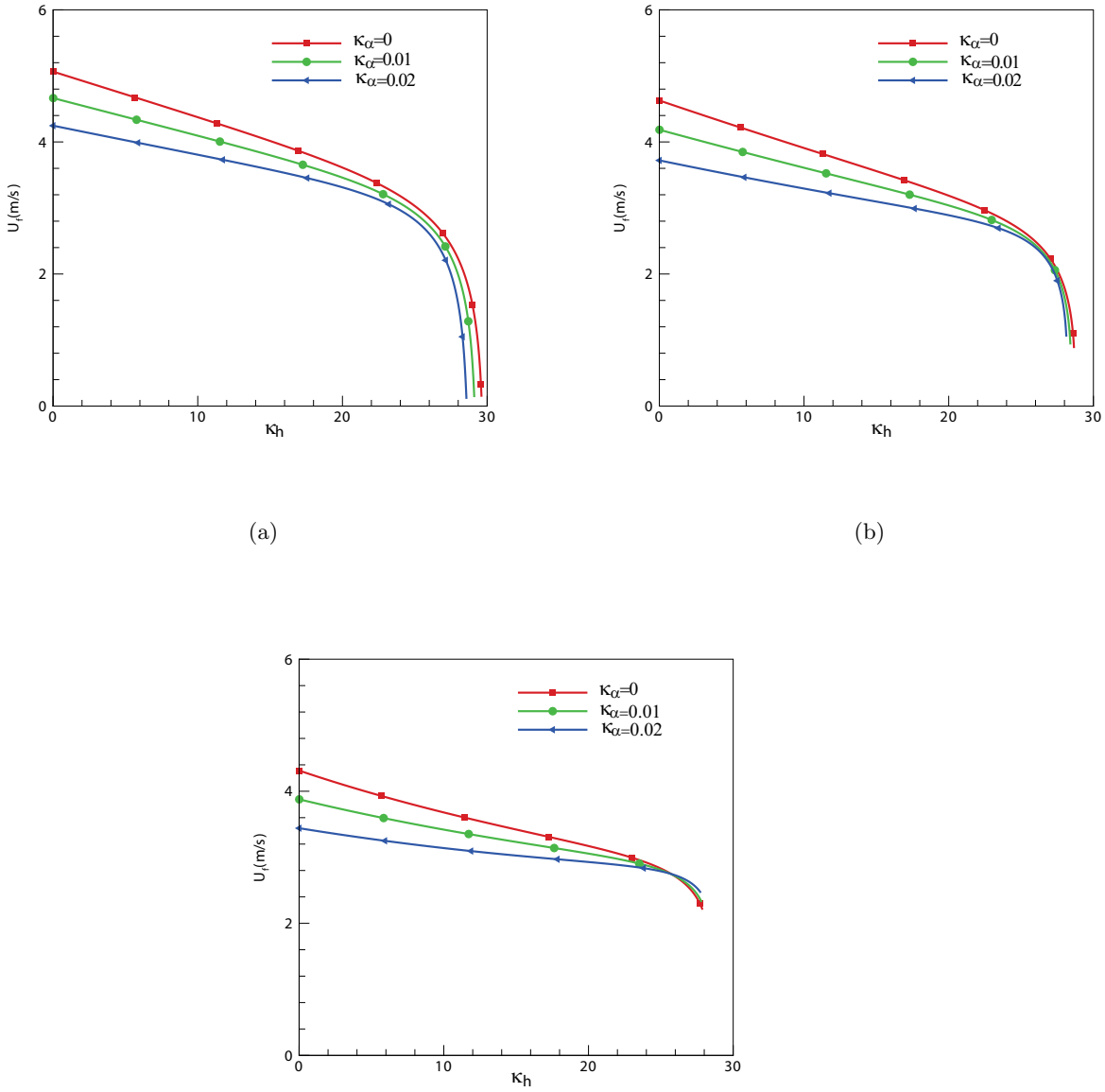

(a)

(b)

(c)

Figure 5.3: Variation of the flutter speed with the feedback gains when $R = 10^5\Omega$ for (a) first configuration, (b) second configuration, and (c) third configuration

5.3 Design of Nonlinear Spring Coefficients

Optimization of the output of the energy harvester can best be determined by increasing the amplitudes of its limit-cycle oscillations and maintaining safe bifurcations. For this purpose, one needs to perform a detailed nonlinear analysis that can be used to characterize the system's stability. As such, we derive next the normal form of the dynamics of the harvester near the flutter onset to assess the impact of the different nonlinearities on the system stability for configurations 5, 6, and 7.

5.3.1 Normal form of the Hopf bifurcation

As demonstrated in the preceding chapter, the Center-Manifold theorem is used to derive the normal form of the Hopf bifurcation. Based on the same strategy, we obtain the following real-valued normal form of the Hopf bifurcation:

$$\dot{r} = \beta_r r + \frac{1}{4} N_{er} r^3 \tag{5.9}$$

$$\dot{\gamma} = \beta_i + \frac{1}{4} N_{ei} r^2 \tag{5.10}$$

where the subscripts r and i denote the real and imaginary parts, respectively.

Equation (5.9) has the following three equilibrium solutions:

$$r = 0 \text{ and } r = \pm\sqrt{\frac{-4\beta_r}{N_{er}}}$$

where $r = 0$ is the trivial solution. The other two solutions are nontrivial. The origin is (a) asymptotically stable for $\beta_r < 0$ or $\beta_r = 0$ and $N_{er} < 0$ and (b) unstable for $\beta_r > 0$ or $\beta_r = 0$ and $N_{er} > 0$. The nontrivial solutions exist when $\beta_r N_{er} < 0$. They are stable (supercritical Hopf bifurcation) for $\beta_r > 0$ and $N_{er} < 0$ and unstable (subcritical Hopf bifurcation) for $\beta_r < 0$ and $N_{er} > 0$. Therefore to decrease the flutter speed, one needs to make sure that the real part of β is positive by choosing the feedback gains. In addition, to eliminate subcritical instabilities, one needs to make sure that the real part of N_e is negative, and to increase the amplitudes of the ensuing limit cycles, one needs to decrease $\mid N_{er} \mid$ by properly choosing the nonlinear spring coefficients.

The expressions of the real part of β and N_e depend on the controlled configuration. For the configurations in Table 5.2, the expressions of the real parts of β and N_e when $R = 10^5\Omega$ are

$$\beta_r = 1.52 \times 10^{-4}\sigma_U \tag{5.11}$$
$$N_{er} = -4.05 \times 10^{-6}c_s + 6.02 \times 10^{-10}k_{h2} - 8.86 \times 10^{-6}k_{\alpha 2}$$

for configuration 5,

$$\beta_r = 1.61 \times 10^{-4}\sigma_U \tag{5.12}$$
$$N_{er} = -2.85 \times 10^{-6}c_s + 4.50 \times 10^{-10}k_{h2} - 6.80 \times 10^{-6}k_{\alpha 2}$$

for configuration 6, and

$$\beta_r = 1.67 \times 10^{-4}\sigma_U \tag{5.13}$$
$$N_{er} = -3.23 \times 10^{-5}c_s + 2.85 \times 10^{-10}k_{h2} - 4.40 \times 10^{-6}k_{\alpha 2}$$

for configuration 7.

We note that, because c_s is positive, its contribution to N_{er} is always negative. The contributions of the nonlinear plunge and pitch springs to N_{er} have opposite effects and could be either positive or negative depending on whether the springs are hard or soft. In all configurations, N_{er} would be always negative, yielding supercritical bifurcations, when the plunge spring is soft and the pitch spring is hard.

5.3.2 System performance

It follows from equations (5.11)-(5.13) that N_{er} and hence the harvester response is more sensitive to the nonlinear pitch spring coefficient k_{α_2} than to the nonlinear plunge spring coefficient k_{h_2}. Moreover, for a given airfoil, the nonlinear aerodynamic contribution is fixed.

Therefore, in the design problem, we set $c_s = 10.833$ and $k_{h_2} = 0$ and investigate the influence of k_{α_2} on the generated power. It follows from equations (5.11)-(5.13) that N_{er} is negative and hence the bifurcation is supercritical as long as k_{α_2} is greater than the critical values -4.943, -4.529, and -79.318 for configurations 5, 6, and 7, respectively. While these values guarantee supercritical bifurcations, they would lead to large motions that may not be applicable or usable. As such, we consider only positive values of k_{α_2}, thereby guaranteeing supercritical Hopf bifurcations. In particular, we consider the following three positive values: $k_{\alpha_2} = 10, 30, \text{and } 50 N.m$.

In Figure 5.4, we show variations of the harvester output with the wind speed as obtained by numerically integrating the full coupled governing equations for configuration 7. The harvested power was calculated from the voltage according to

$$p = \frac{< V^2 >}{R}$$

where $< V^2 >$ is the mean of V^2. As predicted by the normal form, the Hopf bifurcation is supercritical and hence the limit cycles are born above the flutter speed. Moreover, the larger k_{α_2} is, the smaller the pitch, plunge, voltage output, and harvested power are. Consequently, it is desirable to use hard pitch springs with small nonlinear coefficients. We note that the outputs initially increase as the wind speed increases above the flutter speed, as predicted by the normal form. However, this increase is not expected to continue indefinitely. Rather, the outputs, including the generated power, achieve maxima and begin to decrease. Furthermore, the limit-cycle response may loose stability as the wind speed increases away from the flutter speed via a secondary supercritical Hopf bifurcation, leading to either a periodic motion with large period or a quasiperiodic motion.

To examine the system response at speeds much higher than the flutter speed, we show in Figures 5.5 and 5.6 time variations of the voltage output and harvested power at $U = 2.5m/s$ and $U = 3.5m/s$, respectively, for the same configuration when $k_{\alpha 2} = 10N.m$ and $R = 10^5\Omega$. Clearly, the motions undergo various bifurcations, culminating in chaos. We note, however, that these complex motions are accompanied with a reduction in the harvested power. The average power generated for $U = 2.5m/s$ is 0.0031 W and that generated for $U = 3.5m/s$ is 0.0019 W, are significantly lower than 0.0037 W that is generated at the lower speed

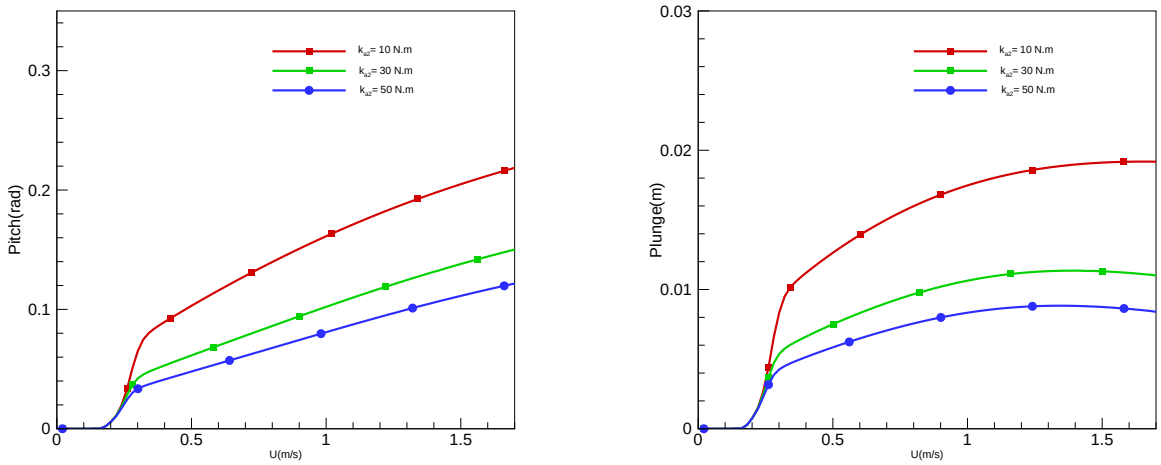

(a)

(b)

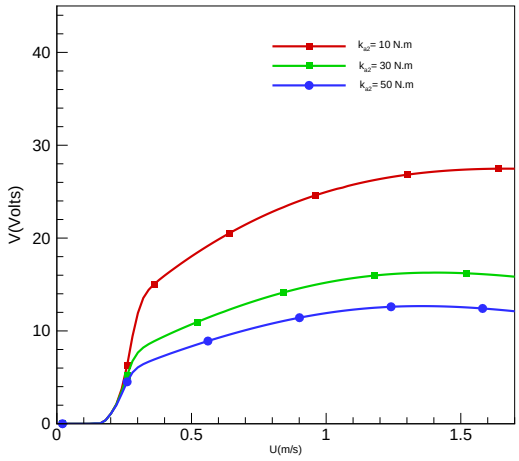

(c)

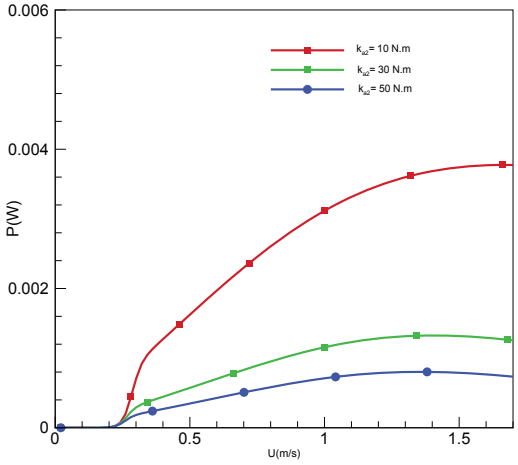

(d)

Figure 5.4: Variation of the (a) pitch, (b) plunge, (c) voltage output, and (d) harvested power with the wind speed for configuration 7 and three values of $k_{\alpha 2}$ when $R = 10^5\Omega$

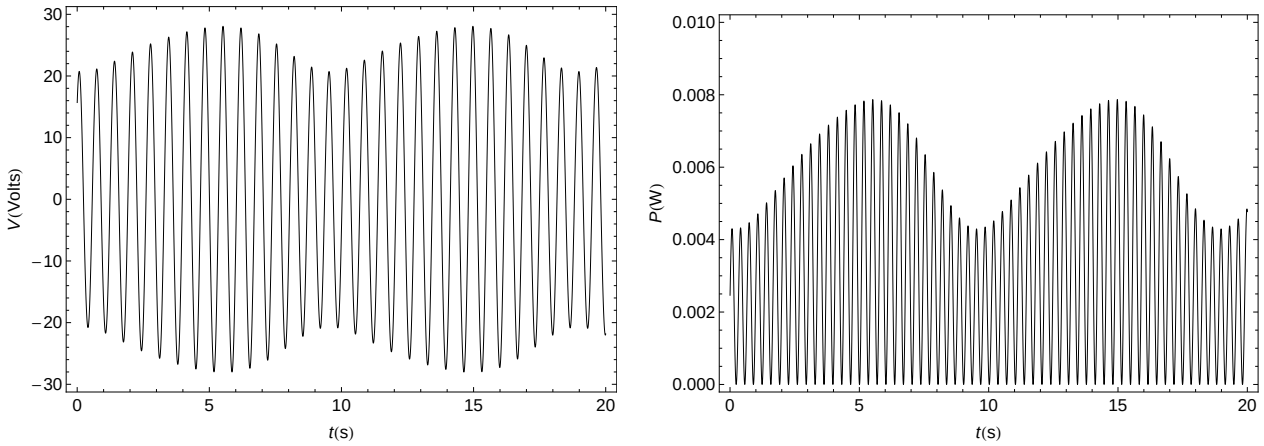

(a) (b)

Figure 5.5: Variation of the (a) voltage output and (b) harvested power when $U = 2.5m/s$ for configuration 7 when $k_{\alpha 2} = 10N.m$ and $R = 10^5\Omega$

$U = 1.7m/s$, as presented in Figure 5.8. To overcome this adverse effect and increase the generated power at higher wind speeds, we adjust the controller gains to increase the flutter speed and hence push the complex motions to higher speeds. In Table 5.3, we show variations of the flutter speed and wind speed for the onset of the secondary Hopf bifurcation with the controller gain $\kappa_\alpha = 0$ when $k_{\alpha 2} = 10N.m$. As expected, the onset speed of the secondary Hopf bifurcation increases by adjusting the controller gain to increase the flutter speed. Figure 5.7 shows that the power that can be generated using this adaptation at higher wind speeds is larger than the power that can be generated for the same flutter speed.

5.4 Conclusions

We have considered design aspects and performance improvement of piezoaeroelastic energy harvesters at low wind speeds. The harvester consists of a pitching and plunging rigid wing supported by linear and nonlinear flexural and torsional springs with a piezoelectric patch attached to the plunge degree of freedom. The aeroelastic system is designed with small structural damping. Then, we choose linear spring coefficients and introduce linear veloc-

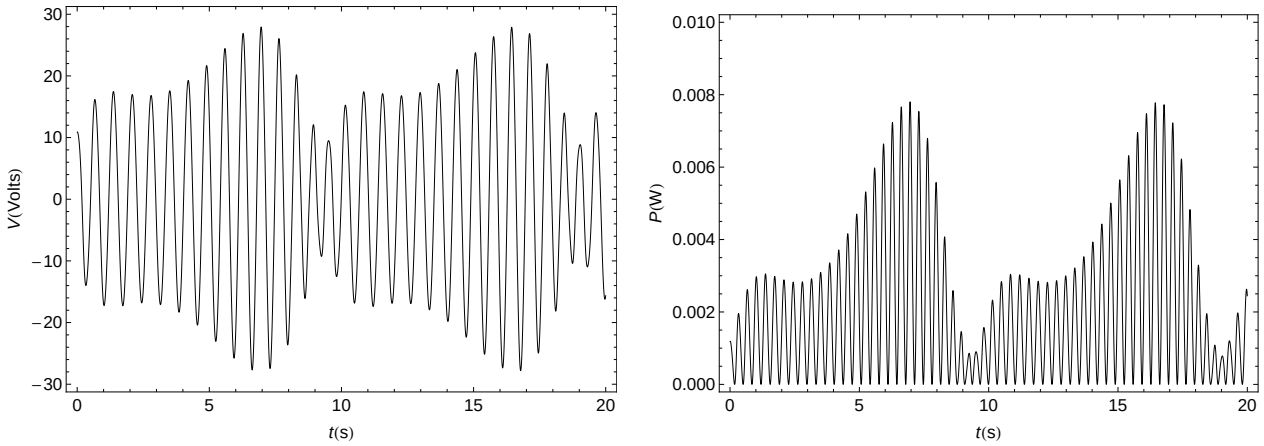

(a) (b)

Figure 5.6: Variation of the (a) voltage output and (b) harvested power when $U = 3.5m/s$ for configuration 7 when $k_{\alpha 2} = 10N.m$ and $R = 10^5\Omega$

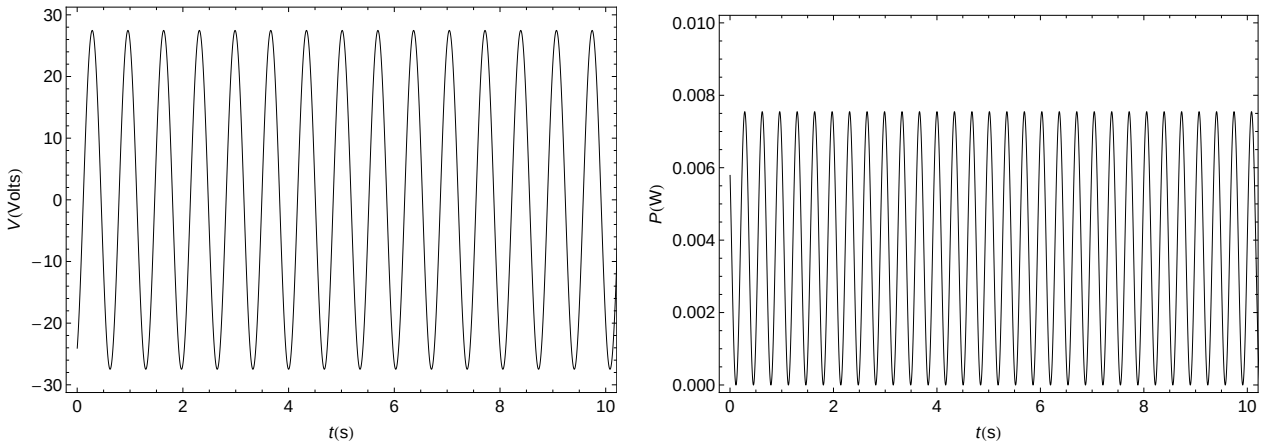

(a) (b)

Figure 5.7: Variation of the (a) voltage output and (b) harvested power when $U = 1.7m/s$ for configuration 7 when $k_{\alpha 2} = 10N.m$ and $R = 10^5\Omega$

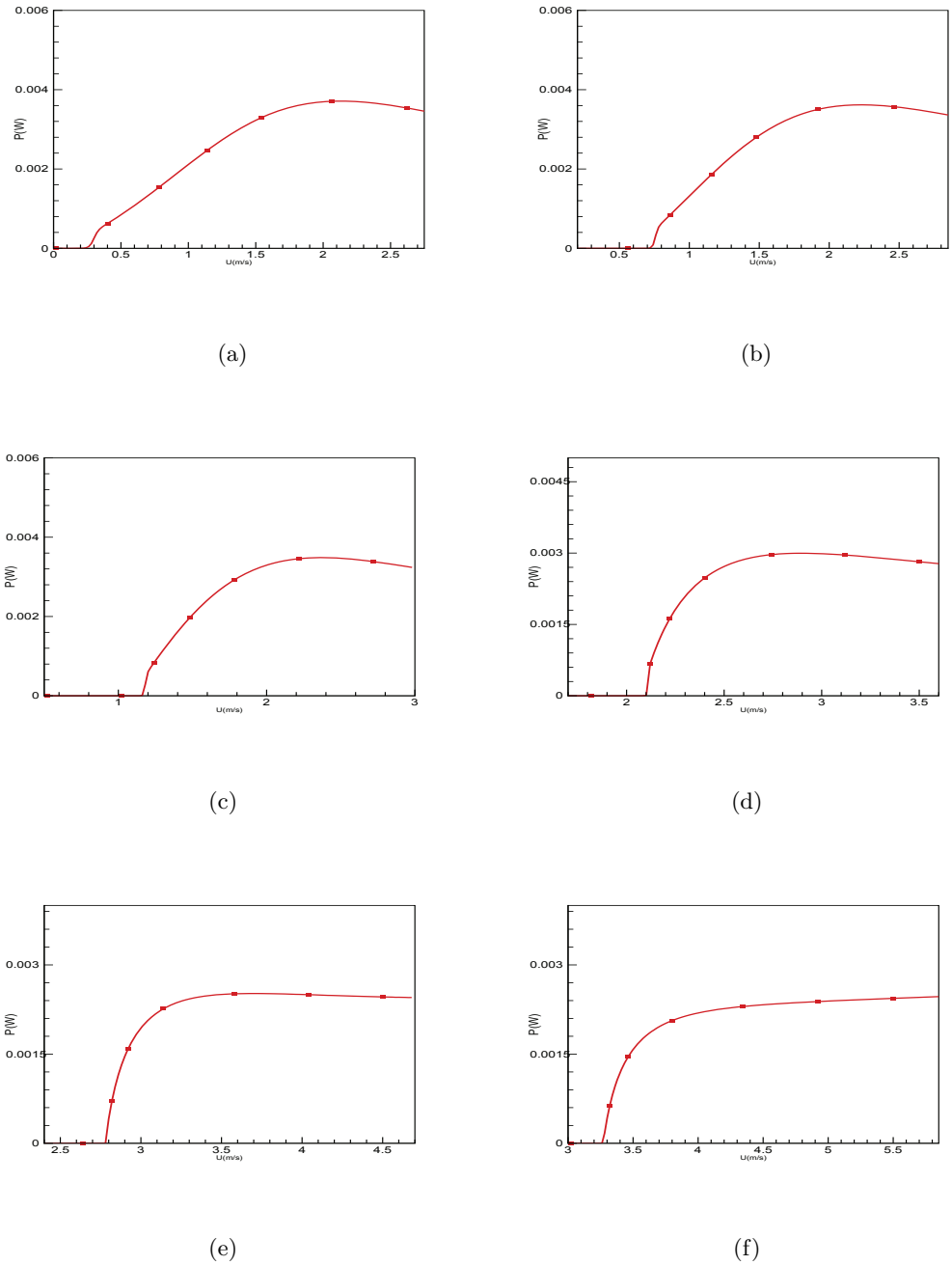

Figure 5.8: Variation of the harvested power with the freestream velocity for the different considered configurations in Table 5.4: (a) κ_h=29.63, (b) κ_h=29.5, (c) κ_h=29.3, (d) κ_h=28.3, (e) κ_h=26.3, and (f) κ_h=23.3 when $k_{\alpha 2} = 10N.m$ and $R = 10^5\Omega$

Table 5.3: Variation of the wind speed at which quasiperiodic motions first appear (i.e., secondary Hopf bifurcation) with the flutter speed for the first configuration when $\kappa_\alpha = 0$ and $k_{\alpha 2} = 10N.m$

κ_h	29.63	29.5	29.3	28.3	26.3	23.3
$U_f(m/s)$	0.025	0.59	1.08	2.07	2.78	3.27
$U_{quasi}(m/s)$	2.2	2.85	3	3.6	4.7	5.85

ity feedback controllers to produce flutter and hence generate energy at any desired (low) wind speed. We have used the normal form of the Hopf bifurcation to choose nonlinear spring coefficients that would (a) produce supercritical Hopf bifurcations and (b) maximize the harvester outputs, including the generated power. The normal form shows that the aerodynamic nonlinearity produces a supercritical bifurcation, whereas the nonlinear spring coefficients produce supercritical or subcritical bifurcations, depending on whether they are hard or soft. This proposed approach for design has been validated by numerically integrating the coupled nonlinear differential equations. The results show that the gains should be adapted to vary the flutter speed, depending on the wind speed. Fixing the gains and hence the flutter speed, we found that the periodic harvester response looses stability via a secondary Hopf bifurcation and other bifurcations that might result in chaotic motions. These complex motions at the higher speeds may result in a reduction in the harvested power and, as such, should be avoided by adjusting the gains.

Chapter 6

Enhancement of Power Harvesting from Piezoaeroelastic Systems

The amount of energy that can be harvested from a wing-based piezoaeroelastic energy harvester depends on its parameters and the wind speed. The distribution of energy between pitch and plunge is determined by different system parameters, including the eccentricity between the gravity axis and the elastic axis, the aerodynamic lift and moment coefficients, the damping coefficients, and the linear and nonlinear coefficients of the springs. In the preceding chapter, we demonstrated that the nonlinear coefficient of the torsional spring can be designed to maximize the harvested power from plunge. However, the choice of this coefficient to maximize the extracted energy can lead to non-physical behaviors (very large angular motions) in pitch. Consequently, to harvest more energy, one needs to minimize the pitch and maximize the plunge. To do so, we investigate in this chapter the effects of the eccentricity between the gravity axis and the elastic axis on the pitch, plunge, and harvested power for two different configurations that would be used at different wind speeds. Particularly, we aim to determine the system parameters that will yield maximum harvested power for specified wind speeds. We also determine the range of wind speeds over which power can be effectively harvested.

6.1 Representation of the Piezoaeroelastic Energy Harvester

We consider a piezoaeroelastic energy harvester consisting of a rigid airfoil constrained to pitch and plunge and supported by linear and nonlinear torsional and flexural springs with a piezoelectric coupling attached to the plunge degree of freedom. As in Chapter 4, the equations of motion of this system are written as:

$$m_T\ddot{h} + m_W x_\alpha b\ddot{\alpha} + c_h\dot{h} + (k_{h0} + k_{h2}h^2)h - \theta V = -L \tag{6.1}$$

$$m_W x_\alpha b\ddot{h} + I_\alpha\ddot{\alpha} + c_\alpha\dot{\alpha} + (k_{\alpha 0} + k_{\alpha 2}\alpha^2)\alpha = M \tag{6.2}$$

$$C_p\dot{V} + \frac{V}{R} + \chi\dot{h} = 0 \tag{6.3}$$

The aerodynamic loads are evaluated using a quasi-steady approximation with a stall model and written as

$$L = \rho U^2 b c_{l\alpha}(\alpha_{eff} - c_s\alpha_{eff}^3) \tag{6.4}$$

$$M = \rho U^2 b^2 c_{m\alpha}(\alpha_{eff} - c_s\alpha_{eff}^3) \tag{6.5}$$

where U is the freestream velocity, $c_{l\alpha}$ and $c_{m\alpha}$ are the aerodynamic lift and moment coefficients, and c_s is a nonlinear parameter associated with stall. The effective angle of attack due to the instantaneous motion of the airfoil is given by

$$\alpha_{eff} = \alpha + \frac{\dot{h}}{U} + (\frac{1}{2} - a)b\frac{\dot{\alpha}}{U}$$

We define the following state variables:

$$X = \begin{bmatrix} X_1 \\ X_2 \\ X_3 \\ X_4 \\ X_5 \end{bmatrix} = \begin{bmatrix} h \\ \dot{h} \\ \alpha \\ \dot{\alpha} \\ V \end{bmatrix} \tag{6.6}$$

and rewrite the equations of motion in the following vector form:

$$\dot{\mathbf{X}} = A(U)\mathbf{X} + \mathbf{C}(\mathbf{X}, \mathbf{X}, \mathbf{X}) \tag{6.7}$$

Table 6.1: Parameters of the considered configurations

	First configuration	Second configuration
$b\ (m)$	0.135	0.135
a	-0.6847	-0.6847
$\rho_p\ (kg/m^3)$	1.225	1.225
$m_W\ (kg)$	2.049	2.049
$m_T\ (kg)$	12.387	12.387
$c_\alpha\ (kgm^2/s)$	0.016	0.036
$c_h\ (kg/s)$	7.43	27.43
$k_{\alpha 0}\ (Nm)$	4	6.833
$k_{h0}\ (N/m)$	1000	2844.4

where $\mathbf{C}(\mathbf{X}, \mathbf{X}, \mathbf{X})$ is a cubic vector function of the state variables and $A(U)$ is given in Chapter 4.

6.2 Effect of the Eccentricity on the Flutter Speed and the Instability

We determine the effect of the eccentricity on the flutter speed and determine critical values for the nonlinear coefficient of the torsional spring that eliminate the occurrence of subcritical Hopf bifurcations for two configurations covering two ranges of wind speeds. The parameters of these configurations are presented in Table 6.1. Figure 6.1 shows variations of the flutter speed with the eccentricity for the two configurations. In both cases, there is an optimum value of the eccentricity for which the flutter speed is minimum. Moreover, when the eccentricity approaches zero, the flutter speed tends to infinity and the system is stable for any wind speed.

The effect of the eccentricity on the system stability is investigated through a nonlinear analysis based on the normal form of the Hopf bifurcation, as derived in Chapter 4. Having the normal form is important to limit the choice of the nonlinear spring coefficients that

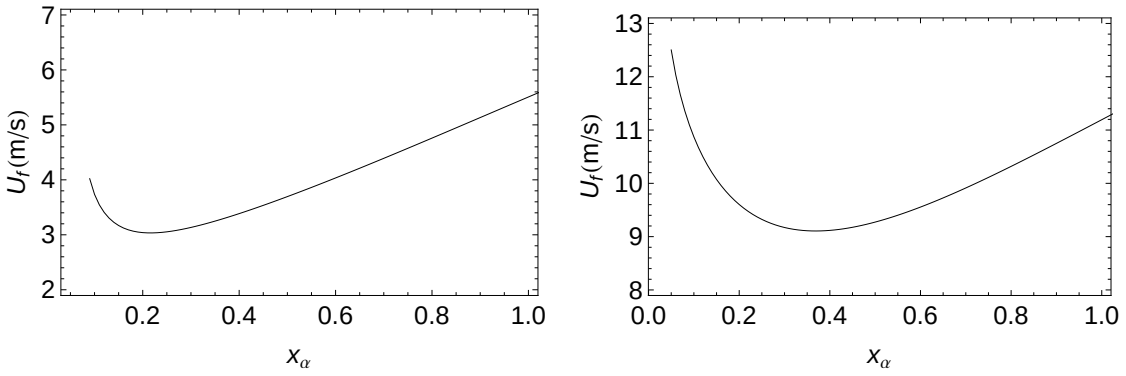

(a) (b)

Figure 6.1: Variations of the flutter speed U_f with the eccentricity x_α in the first (a) and second (b) configurations when the load resistance $R = 10^6\Omega$

would produce only supercritical (safe) bifurcations. As derived in Chapter 4, the real-valued normal form of the Hopf bifurcation are given by

$$\dot{a} = \beta_r a + \frac{1}{4} N_{er} a^3 \tag{6.8}$$

$$\dot{\gamma} = \beta_i + \frac{1}{4} N_{ei} a^2 \tag{6.9}$$

where a and γ represent the amplitude and phase of the limit-cycle oscillation. The subscripts r and i denote the real and imaginary parts, respectively; β_r is the linear growth rate; and β_i is the linear frequency. The effective nonlinearity N_e depends on the system parameters, including the eccentricity x_α, the nonlinear coefficients $k_{\alpha 2}$ and k_{h2} of the springs, and the nonlinear aerodynamic coefficient c_s, which is taken to be equal to 10.833.

Equation (6.8) has the following three equilibrium solutions:

$$a = 0 \text{ and } a = \pm\sqrt{\frac{-4\beta_r}{N_{er}}}$$

where $a = 0$ is the trivial solution. The other two solutions are nontrivial. The origin is (a)

Table 6.2: The real part of the effective nonlinearity for different values of the eccentricity x_α for the first configuration when $R = 10^6\Omega$ and $c_s = 10.833$

x_α	N_{er}
0.1	-1.2 $\times$ 10^{-6} + 9.5 $\times$ 10^{-12} k_{h2} - 1.7 $\times$ 10^{-7} $k_{\alpha 2}$
0.2	-1.5$\times$ 10^{-6} - 1.6 $\times$ 10^{-11} k_{h2} +7.6 $\times$ 10^{-7} $k_{\alpha 2}$
0.3	-4.1 $\times$ 10^{-6} - 3.3 $\times$ 10^{-11} k_{h2} +2.0 $\times$ 10^{-6} $k_{\alpha 2}$
0.4	-6.7 $\times$ 10^{-6} - 4.9 $\times$ 10^{-11} k_{h2} +2.9 $\times$ 10^{-6} $k_{\alpha 2}$

Table 6.3: The real part of the effective nonlinearity for different values of the eccentricity x_α for the second configuration when $R = 10^6\Omega$ and $c_s = 10.833$

x_α	N_{er}
0.05	-1.3 $\times$ 10^{-6}- 3.4 $\times$ 10^{-12} k_{h2} +9.1 $\times$ 10^{-9} $k_{\alpha 2}$
0.1	-5.4$\times$ 10^{-6}- 1.3 $\times$ 10^{-11} k_{h2} +1.1 $\times$ 10^{-7} $k_{\alpha 2}$
0.3	-3.9 $\times$ 10^{-5}- 3.3 $\times$ 10^{-11} k_{h2} +7.9 $\times$ 10^{-7} $k_{\alpha 2}$
0.4	-6.4 $\times$ 10^{-5}- 3.4 $\times$ 10^{-11} k_{h2} +1.1 $\times$ 10^{-6} $k_{\alpha 2}$

asymptotically stable for $\beta_r < 0$ or $\beta_r = 0$ and $N_{er} < 0$ and (b) unstable for $\beta_r > 0$ or $\beta_r = 0$ and $N_{er} > 0$. The nontrivial solutions exist when $\beta_r N_{er} < 0$. They are stable (supercritical Hopf bifurcation) for $\beta_r > 0$ and $N_{er} < 0$ and unstable (subcritical Hopf bifurcation) for $\beta_r < 0$ and $N_{er} > 0$. To eliminate subcritical instabilities, one needs to make sure that the real part of N_e is negative. The amplitudes of the ensuing limit cycles also depend on $\mid N_{er} \mid$ and one needs to decrease it by properly choosing the nonlinear coefficients of the springs.

Tables 6.2 and 6.3 show N_{er} as functions of k_{α_2} and k_{h_2} for different values of x_α for the first and second configurations, respectively. As c_s is set equal to 10.833, its contribution to N_{er} is always negative for both considered configurations. The contributions of the nonlinear coefficients of the plunge and pitch springs to N_{er} have opposite effects and could be either positive or negative, depending on whether they are hard or soft. In all configurations, N_{er} can be made negative, yielding supercritical bifurcations by properly choosing the nonlinear coefficients of the springs. We note that, in both configurations, the sensitivity of N_{er} to

Table 6.4: Variation of the flutter speed and the nonlinear coefficient of the torsional spring with the eccentricity for the first configuration

x_α	0.1	0.2	0.3	0.4
$U_f(m/s)$	3.73	3.04	3.13	3.38
β_r	0.27 σ_U	0.50 σ_U	0.82 σ_U	1.22 σ_U
$k_{\alpha 2}^{cr}$	-6.8	21.4	22.1	24.7

Table 6.5: Variations of the flutter speed and the nonlinear coefficient of the torsional spring with the eccentricity for the second configuration

x_α	0.05	0.1	0.3	0.4
$U_f(m/s)$	12.62	10.95	9.23	9.17
β_r	1.1 σ_U	1.98 σ_U	3.66 σ_U	4.54 σ_U
$k_{\alpha 2}^{cr}$	146.2	50.7	49.1	55.65

the nonlinear coefficient of the plunge spring is very small in comparison to its sensitivity to the nonlinear coefficient of the torsional spring and the nonlinear aerodynamic coefficient. Moreover, the sensitivity to k_{α_2} increases with increasing x_α in both configurations.

Tables 6.4 and 6.5 show the effects of varying x_α on U_f and β_r when $R = 10^6\Omega$ for the first and second configurations, respectively. In addition, we present in these tables the critical values of the nonlinear coefficient of the torsional spring when the nonlinear coefficient of the plunge is set equal to $k_{h2} = 67.685N/m$. It follows from Tables 6.2 and 6.3 that N_{er} is negative and hence the bifurcation is supercritical as long as k_{α_2} is smaller than the correspondent critical value for each case of x_α for both configurations except the case when $x_\alpha = 0.1$ for the first configuration. Indeed, for this case, a supercritical instability is obtained when $k_{\alpha_2} > k_{\alpha_2}^{cr}$. As shown below, this characterization of the effect of x_α on the critical values of k_{α_2} will help us choose the nonlinear coefficient of the torsional spring that results in a safe (i.e., free of jumps and hysteresis) response and maximum harvested power.

Figures 6.2 and 6.3 show variation of the system outputs with the nonlinear torsional spring coefficient and the eccentricity for $U = 5m/s$ in the first configuration and $U = 15m/s$

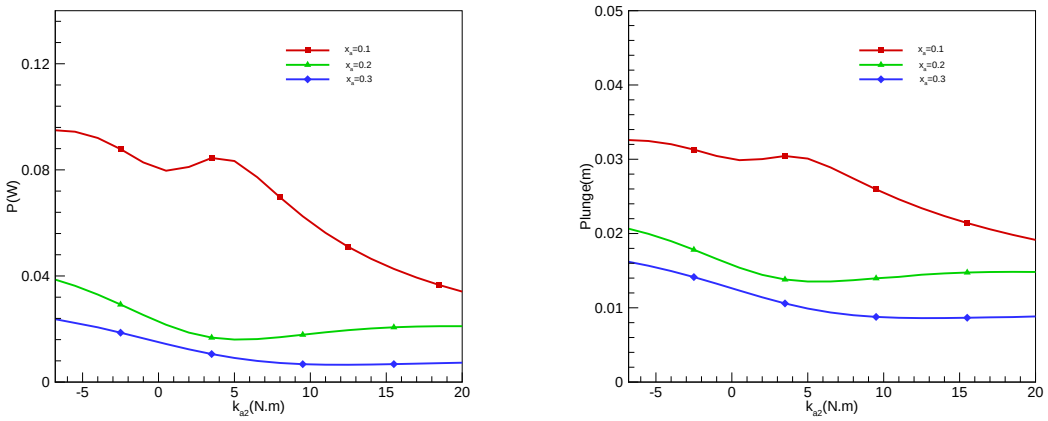

(a)

(b)

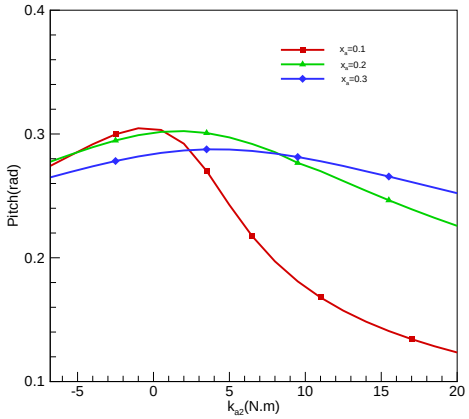

(c)

Figure 6.2: Variation of the (a) harvested power, (b) plunge amplitude, and (c) pitch amplitude with $k_{\alpha 2}$ for different values of the eccentricity when $U = 5m/s$ and $R = 10^6\Omega$ for the first configuration

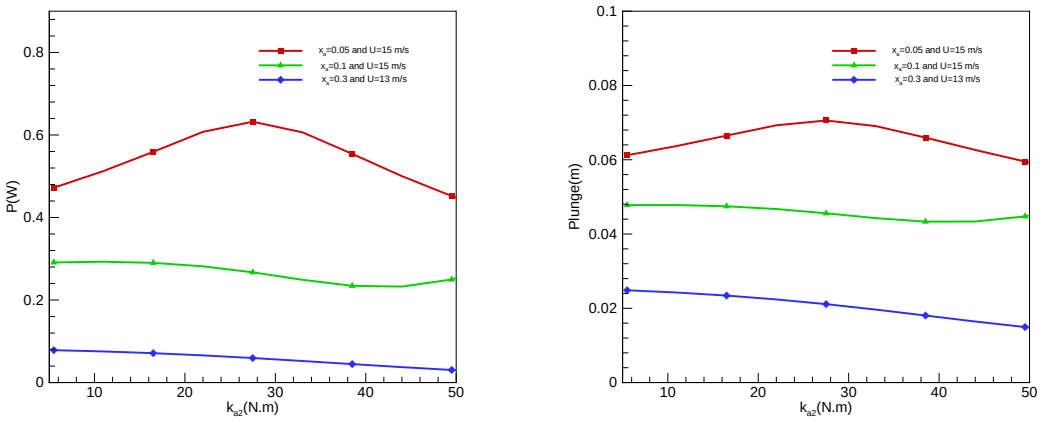

(a) (b)

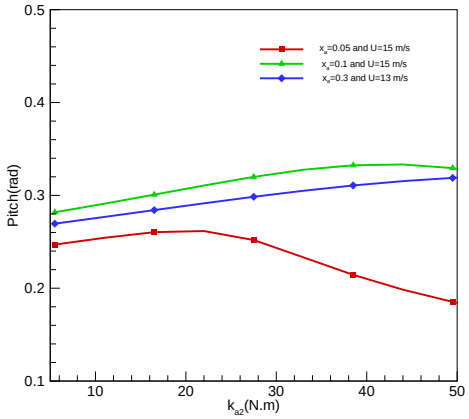

(c)

Figure 6.3: Variation of the (a) harvested power, (b) plunge amplitude, and (c) pitch amplitude with $k_{\alpha 2}$ for different values of the eccentricity when $R = 10^6\Omega$ and $U > U_f$

in the second configuration. For the second configuration, quasiperiodic responses occur when $x_\alpha = 0.3$ and $U = 15m/s$. As such, the wind speed was reduced to $U = 13m/s$. We note that decreasing the eccentricity is accompanied by an increase in the plunge amplitude and hence the harvested power. We note also that there is an optimum value of $k_{\alpha 2} \approx -6N.m$ in the first configuration and $k_{\alpha 2} \approx 25N.m$ in the second configuration which yield maximum harvested power and supercritical bifurcation. These power levels are obtained when $x_\alpha = 0.1$ and 0.05, respectively, for the first and second configurations.

To determine the relation between the level of harvested power and the eccentricity, we show in Figures 6.4 and 6.5 the effect of the eccentricity on the system outputs for $k_{\alpha 2}= -6N.m$ and $10N.m$ for the first configuration and $k_{\alpha 2} = 0N.m$ and $25N.m$ for the second configuration. The respective freestream velocities are set equal to $5m/s$ and $15m/s$. We note that, for the two distinct values of $k_{\alpha 2}$, an increase in the eccentricity results in a decrease in the plunge amplitude and hence the harvested power. The results also show that the harvested energy is the highest for small eccentricity for which the pitch amplitude is small and the plunge amplitude is large. For example, Figure 6.5 shows that, as x_α decreases from 0.33 to 0.1, the harvested power increases from $0.021W$ to $0.088W$ when $k_{\alpha 2} = -6N.m$ and from $0.014W$ to $0.064W$ when $k_{\alpha 2} = 10N.m$. Moreover, Figure 6.6 shows that, as x_α decreases from 0.33 to 0.05, the harvested power increases from $0.092W$ to $0.43W$ when $k_{\alpha 2} = 0N.m$ and from $0.062W$ to $0.63W$ when $k_{\alpha 2} = 25N.m$. These results clearly show that the harvested power can be increased by an order of magnitude by a proper choice of the eccentricity.

Next, we assess the influence of the load resistance on the harvested power. We show in Figure 6.6 variation of the harvested power with the load resistance when $U = 5m/s$ and $U = 15m/s$ for the first and second configurations, respectively. We note that, for every eccentricity and configuration, there is an optimum load resistance that maximizes the harvested power. We also note that, for both configurations and all eccentricities, the optimum values are in the range of $R \approx 10^6\Omega$.

Finally, it is also important to assess variation of the harvested power with the wind speed near the design values of the eccentricity and the load resistance. To this end, we show in Figures 6.7-a and 6.7-b variation of the harvested power with the wind speed for the

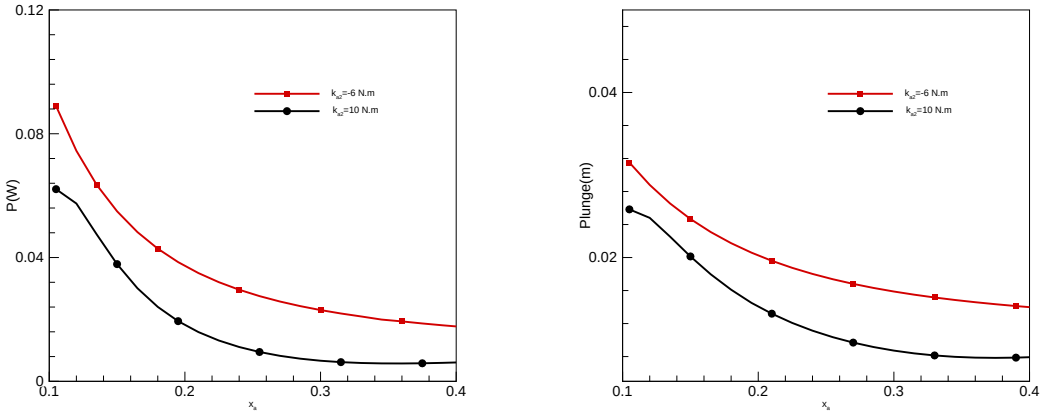

(a) (b)

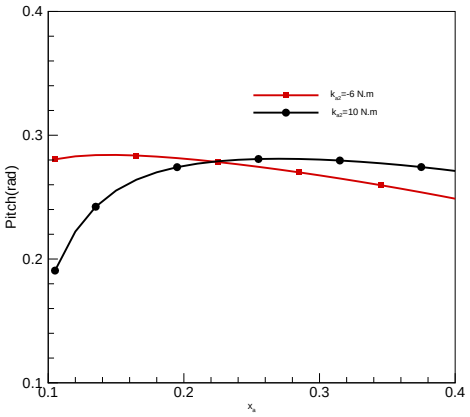

(c)

Figure 6.4: Variation of the (a) harvested power, (b) plunge amplitude, and (c) pitch amplitude with the eccentricity for different values of $k_{\alpha 2}$ when $U = 5m/s$ and $R = 10^6\Omega$ for the first configuration

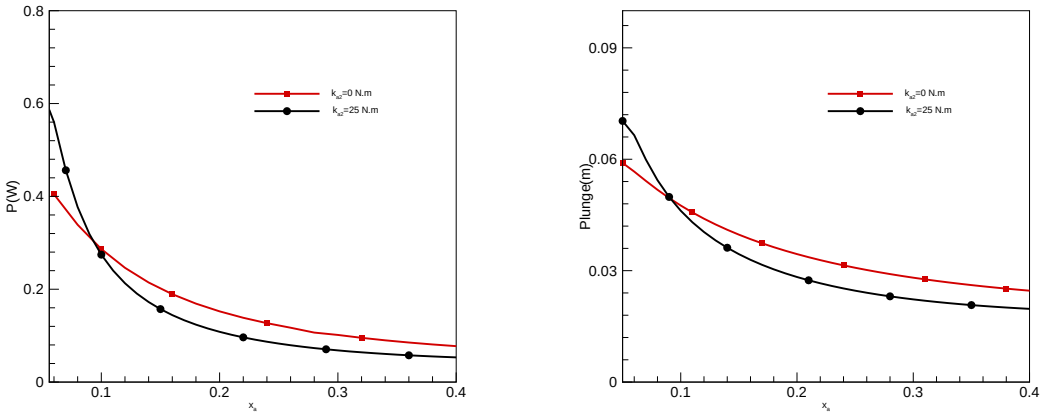

(a) (b)

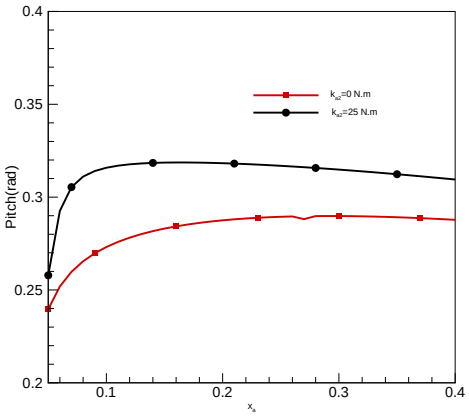

(c)

Figure 6.5: Variation of the (a) harvested power, (b) plunge amplitude, and (c) pitch amplitude with the eccentricity for different values of $k_{\alpha 2}$ when $U = 15m/s$ and $R = 10^6\Omega$ for the second configuration

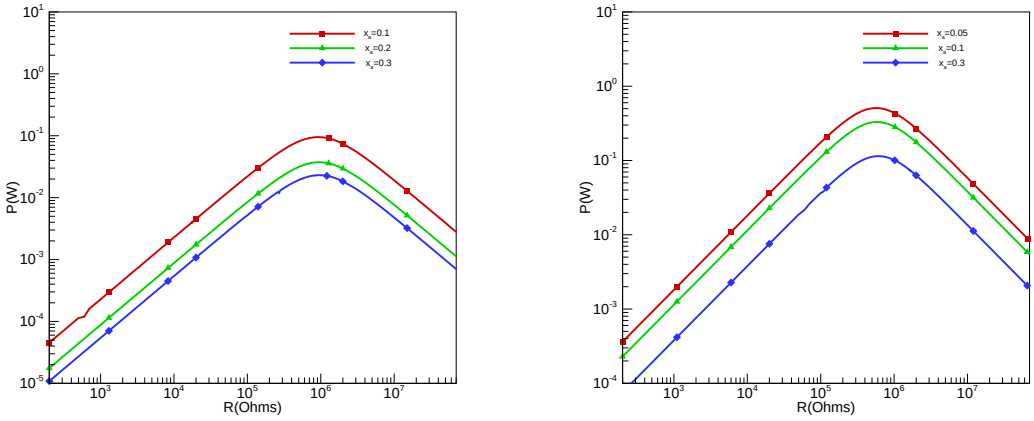

(a) (b)

Figure 6.6: Variation of the harvested power with the load resistance when (a) $k_{\alpha 2} = -6N.m$ and $U = 5m/s$ for the first configuration and (b) $k_{\alpha 2} = 25N.m$ and $U = 15m/s$ for the second configuration for different values of the eccentricity

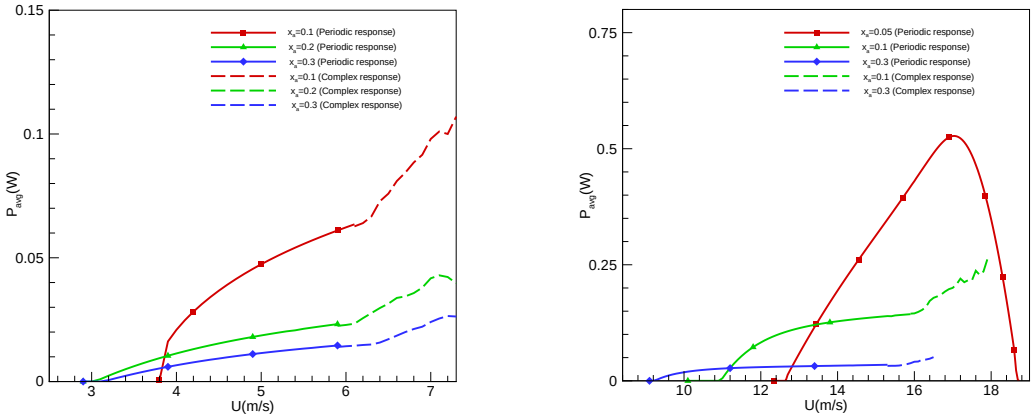

(a) (b)

Figure 6.7: Variation of the harvested power with the wind speed when (a) $k_{\alpha 2} = -6N.m$ for the first configuration and (b) $k_{\alpha 2} = 25N.m$ for the second configuration for different values of the eccentricity when $R = 10^6\Omega$

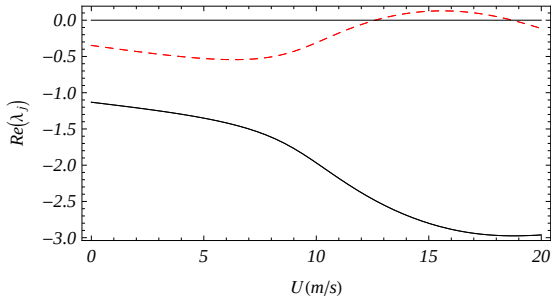

(a)

Figure 6.8: Variation of the damping with the wind speed for the second configuration when $x_\alpha = 0.05$

first and second configurations when the nonlinear coefficient of the torsional spring and the load resistance are chosen to produce the maximum harvested power. We note that, for the first configuration, the harvested power increases as the wind speed increases. The response is periodic for wind speeds up to $6.2m/s$, $5.98m/s$, $6.15m/s$ for $x_\alpha = 0.1$, $x_\alpha = 0.2$, and $x_\alpha = 0.3$, respectively. Beyond these speeds, the response becomes quasiperiodic and then chaotic. It is important to note that the harvested power in the quasiperiodic or chaotic regime cannot be always guaranteed to be larger than the harvested power in the periodic regime, as presented in Chapter 5. Moreover, we note that decreasing the eccentricity results in an increase in the harvested power for all considered freestream velocities.

It follows from Figure 6.7-b that the flutter speed is more affected by the eccentricity in the second configuration than in the first configuration. In addition, the quasiperiodic motions occur when the wind speed increases beyond $15.9m/s$ and $15.3m/s$ when $x_\alpha = 0.1$ and $x_\alpha = 0.3$, respectively. On the other hand, when $x_\alpha = 0.05$, the harvested power increases to a maximum averaged value near $0.5W$ $(1Wpeak)$ at a wind speed of about $17m/s$. As the wind speed is increased further, the level of harvested power drops suddenly to near zero at the wind speed $18.8m/s$. This drop in the harvested power is related to the decrease in the damping associated with the aerodynamics effects up to the point where it becomes negative and causes the harvester to regain stability, as can be seen from the plot in Figure 6.8.

6.3 Conclusions

The amount of energy that can be harvested from a piezoaeroelastic system, a pitching and plunging rigid airfoil supported by nonlinear springs, depends on its parameters and the wind speed. Particularly, the distribution of energy between the pitch and plunge motions and hence the harvested energy is determined by the system parameters, including the eccentricity between the gravity and elastic axes, the aerodynamic lift and moment coefficients, and the nonlinear coefficients of the structural springs. We have investigated the effect of the eccentricity on the pitch, plunge, and harvested power for two different configurations. An analysis based on the normal form of the Hopf bifurcation yields a characterization of the effect of the eccentricity on the critical values of the nonlinear coefficients of the springs that result in large harvested power and yet avoid jumps and hysteresis. This analysis helps in choosing the required nonlinear spring coefficients for safe operation and maximum harvested power. The results show that the harvested power can be increased by an order of magnitude by properly choosing small eccentricities. They also show that the harvested power can be increased by properly choosing the load resistance and designing the harvester to operate optimally at the prevailing wind speeds.

Chapter 7

Sensitivity Analysis of Piezoaeroelastic Energy Harvesters

In the previous chapter, it is demonstrated that the level of the harvested power is a function of the harvester parameters and wind speed. If the energy is harvested from plunge, it would be important to design an aeroelastic system where the pitch amplitude is kept small and mostly, the wind energy is picked up by plunge. Because the amplitudes of these motions depend on many system parameters, it is important to evaluate the uncertainties associated with variations in these parameters and the respective sensitivities to these variations. Although one could independently vary one parameter and keep the others constant to achieve this objective, a better analysis would allow for combined variations in the system parameters.

In this Chapter, we aim to evaluate the sensitivities of the harvested power, pitch, and plunge amplitudes to the load resistance, the eccentricity between the gravity axis and elastic axis, and the nonlinear coefficients of the springs. To this end, we employ the non-intrusive formulation of the Polynomial Chaos Expansion (PCE) in terms of the multivariate Hermite polynomials to quantify the effects of variations in the load resistance, the eccentricity, and the nonlinear coefficients of the springs on the harvested power and the pitch and plunge amplitudes.

7.1 Modeling of the Energy Harvester

The energy harvester consists of a rigid airfoil that is allowed to move with two degrees of freedom. The airfoil is supported by linear and nonlinear torsional and flexural springs with a piezoelectric coupling attached to the plunge degree of freedom. The governing equations of this system are written as:

$$m_T\ddot{h} + m_W x_\alpha b\ddot{\alpha} + c_h\dot{h} + (k_{h0} + k_{h2}h^2)h - \theta V = -L \tag{7.1}$$

$$m_W x_\alpha b\ddot{h} + I_\alpha\ddot{\alpha} + c_\alpha\dot{\alpha} + (k_{\alpha0} + k_{\alpha2}\alpha^2)\alpha = M \tag{7.2}$$

$$C_p\dot{V} + \frac{V}{R} + \theta\dot{h} = 0 \tag{7.3}$$

where m_T is the total mass of the wing, including its support structure; m_W is the wing mass alone; I_α is the mass moment of inertia about the elastic axis; l is the wing span; b is the half chord length; x_α is the dimensionless distance between the center of mass and the elastic axis; c_h and c_α are, respectively, the plunge and pitch structural damping coefficients; L and M are the aerodynamic lift and moment about the elastic axis; R is the load resistance; V is the voltage across this load resistance; C_p is the capacitance of the piezoelectric layer; θ is the electromechanical coupling term; k_{h0} and $k_{\alpha0}$ are the linear structural stiffnesses for the plunge and pitch degrees of freedom, respectively; and k_{h2} and $k_{\alpha2}$ are, respectively, the nonlinear structural stiffnesses for the plunge and pitch degrees of freedom.

The aerodynamic loads are evaluated using a quasi-steady approximation with a stall model and written as

$$L = \rho U^2 b c_{l\alpha}(\alpha_{eff} - c_s\alpha_{eff}^3) \tag{7.4}$$

$$M = \rho U^2 b^2 c_{m\alpha}(\alpha_{eff} - c_s\alpha_{eff}^3) \tag{7.5}$$

where U is the freestream velocity, $c_{l\alpha}$ and $c_{m\alpha}$ are the aerodynamic lift and moment coefficients, and c_s is a nonlinear parameter associated with stall. The effective angle of attack

due to the instantaneous motion of the airfoil is given by (201)

$$\alpha_{eff} = \alpha + \frac{\dot{h}}{U} + (\frac{1}{2} - a)b\frac{\dot{\alpha}}{U}$$

where a is the position of the elastic axis relative to the mid chord.

To determine the stability characteristics, we introduce the following state variables:

$$X = \begin{bmatrix} X_1 \\ X_2 \\ X_3 \\ X_4 \\ X_5 \end{bmatrix} = \begin{bmatrix} h \\ \dot{h} \\ \alpha \\ \dot{\alpha} \\ V \end{bmatrix} \tag{7.6}$$

The equations of motion are then rewritten in the following vector form (30):

$$\dot{\mathbf{X}} = A(U)\mathbf{X} + \mathbf{C}(\mathbf{X}, \mathbf{X}, \mathbf{X}) \tag{7.7}$$

where $\mathbf{C}(\mathbf{X}, \mathbf{X}, \mathbf{X})$ is a cubic vector function of the state variables and

$$A(U) = \begin{bmatrix} 0 & 1 & 0 & 0 & 0 \\ -\frac{I_\alpha k_{h0}}{d} & -(c_1 + d_1 U) & -(k_1 U^2 - \frac{m_W x_\alpha b k_{\alpha 0}}{d}) & -(c_2 + d_2 U) & -\theta_1 \\ 0 & 0 & 0 & 1 & 0 \\ \frac{m_W x_\alpha b k_{h0}}{d} & -(c_3 + d_3 U) & -(k_2 U^2 + \frac{k_{\alpha 0} m_T}{d}) & -(c_4 + d_4 U) & -\theta_2 \\ 0 & -\frac{\chi_1}{C_p} & 0 & 0 & -\frac{1}{RC_p} \end{bmatrix}$$

The matrix $A(U)$ has a set of five eigenvalues λ_i, $i = 1, 2..., 5$, which determine the stability of the trivial solution of equation (7.7). We arrange these eigenvalues so that the first four are complex conjugates ($\lambda_2 = \overline{\lambda_1}$ and $\lambda_4 = \overline{\lambda_3}$). The wind speed at which one or more eigenvalues have zero real parts corresponds to the onset of linear instability and is termed the flutter speed, U_f.

7.2 Effects of Eccentricity and Load Resistance on the Flutter Speed

As a first step in the sensitivity analysis, we determine the effects of the eccentricity and the load resistance on the flutter speed. The rest of the parameters of the energy harvester

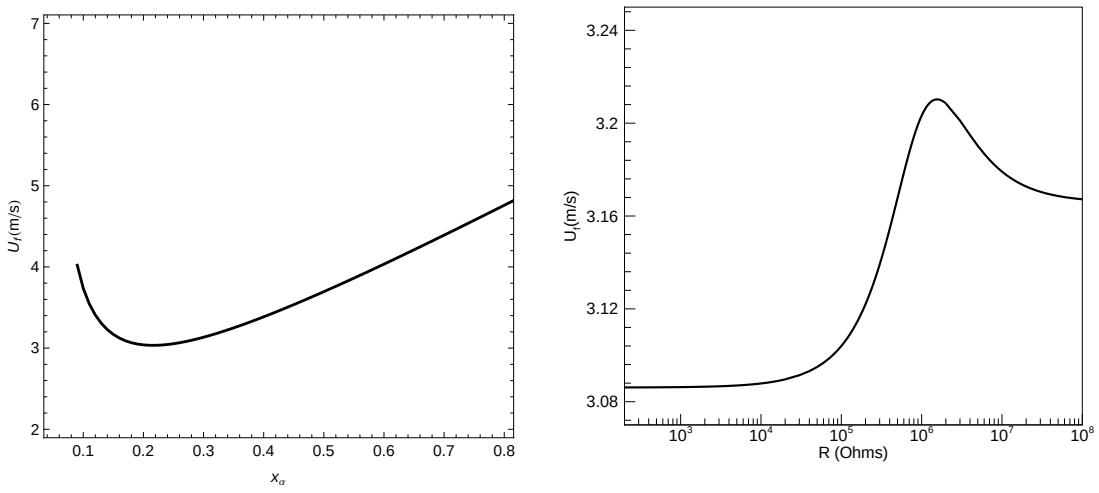

(a) (b)

Figure 7.1: Variations of the flutter speed U_f with (a) the eccentricity x_α when $R = 10^6\Omega$ and (b) the load resistance R when $x_\alpha = 0.33$.

Table 7.1: Parameters of the piezoaeroelastic system

$b\ (m)$	0.135
a	-0.6847
$\rho\ (kg/m^3)$	1.225
$m_W\ (kg)$	2.049
$m_T\ (kg)$	12.387
$c_\alpha\ (kgm^2/s)$	0.016
$c_h\ (kg/s)$	7.43
$k_{\alpha 0}\ (Nm)$	4
$k_{h0}\ (N/m)$	1000

are presented in Table 7.1. These parameters are chosen to enable energy harvesting at low freestream velocities. As shown in Figure 7.1-a, the choice of the eccentricity plays an important role in determining the flutter speed. We note that, as the distance between the elastic and gravity axes is decreased to very small values, the flutter speed approaches infinity. The same figure shows also that there is a value for which the flutter speed is minimum. Inspecting Figure 7.1-b, we note that the flutter speed depends also on the electrical load resistance. These results are used in the subsequent analysis to make sure that flutter will always take place. To this end, we set the wind speed at $5m/s$.

7.3 Stability Analysis of the Harvester

Solving numerically the equations of motion of this piezoaeroelastic system, we note that decreasing the eccentricity is followed by an increase in the harvested power, as shown in Figure 7.2-a. We note also that there is an optimum value for the load resistance to maximize the harvested energy. In addition, when varying the eccentricity, we find that that the maximum harvested power occurs when the load resistance is approximately equal to $10^6\Omega$, as shown in Figures 7.2-b.

In the rest of this chapter, we focus on the harvester's performance for a load resistance near $R = 10^6\Omega$ and an eccentricity $x_\alpha = 0.2$. To investigate the system output near the

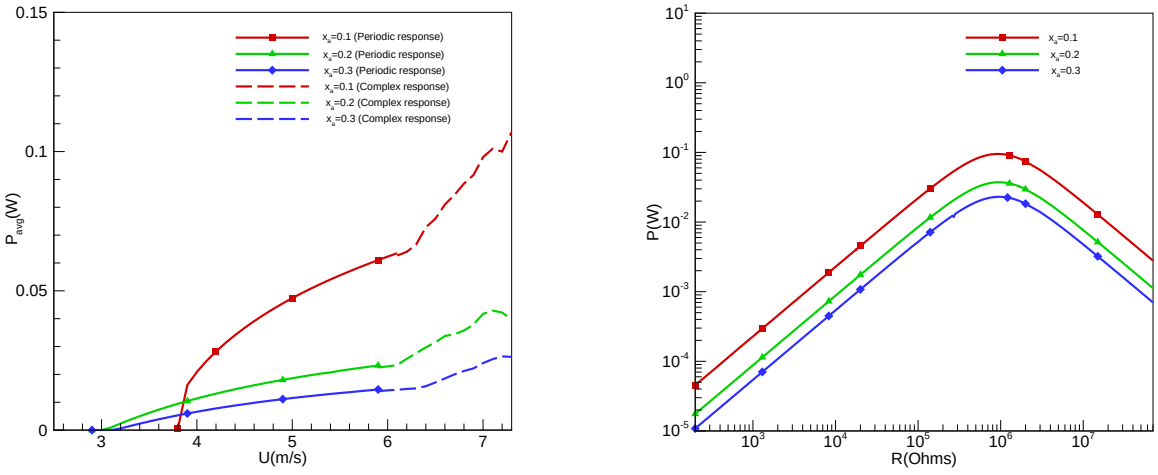

(a) (b)

Figure 7.2: Variations of the harvested power with (a) the wind speed when $R = 10^6\Omega$ and $k_{\alpha 2} = -6N.m$ and (b) the load resistance when $U = 5m/s$ and $k_{\alpha 2} = -6N.m$ for different values of the eccentricity.

bifurcation and determine whether the instability is supercritical or subcritical, we use the normal form of the Hopf bifurcation (202). We derived the normal form of the Hopf bifurcation for a piezoaeroelastic energy harvester in Chapter 4. The real-valued normal form of the Hopf bifurcation has the following form:

$$\dot{r} = \beta_r r + \frac{1}{4} N_{er} r^3 \tag{7.8}$$

$$\dot{\gamma} = \beta_i + \frac{1}{4} N_{ei} r^2 \tag{7.9}$$

where r is the amplitude and γ is the phase of the ensuing limit cycle and the subscripts r and i denote the real and imaginary parts, respectively. The effective nonlinearity N_e depends on the nonlinear coefficients ($k_{\alpha 2}$ and k_{h2}) of the springs and the nonlinear aerodynamic coefficient (c_s), which is set equal to 10.833 (200).

Equation (7.8) has the following three equilibrium solutions:

$$r = 0 \text{ and } r = \pm\sqrt{\frac{-4\beta_r}{N_{er}}}$$

where $r = 0$ is the trivial solution. The other two solutions are nontrivial. The origin is (a) asymptotically stable for $\beta_r < 0$ or $\beta_r = 0$ and $N_{er} < 0$ and (b) unstable for $\beta_r > 0$ or $\beta_r = 0$ and $N_{er} > 0$. The nontrivial solutions exist when $\beta_r N_{er} < 0$. They are stable (supercritical Hopf bifurcation) for $\beta_r > 0$ and $N_{er} < 0$ and unstable (subcritical Hopf bifurcation) for $\beta_r < 0$ and $N_{er} > 0$. To eliminate subcritical behaviors and at the same time enhance the amplitudes of the ensuing limit-cycle oscillations (LCOs), we require that the real part of the effective nonlinearity N_e to be negative and very close to zero.

For the considered configuration, the real part of the effective nonlinearity is given by

$$N_{er} = -1.5 \times 10^{-6} - 1.6 \times 10^{-11} k_{h2} + 7.6 \times 10^{-7} k_{\alpha 2} \tag{7.10}$$

The contributions of the nonlinear coefficients of the flexural and torsional springs to N_{er} have opposite effects and could be either positive or negative, depending on whether the springs are hard or soft. To avoid any subcritical instabilities, we require N_{er} to be negative. Hence, when

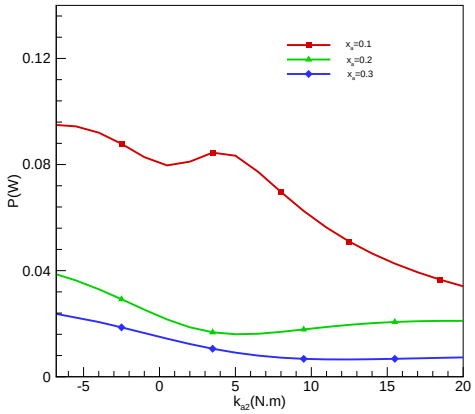

(a)

Figure 7.3: Variation of the harvested power with $k_{\alpha 2}$ for different values of the eccentricity when $U = 5m/s$ and $R = 10^6\Omega$

$k_{h2} = 67.685N/m$ and $x_\alpha = 0.2$, k_{α_2} must be less than $21.4N.m$ for supercritical instability. For this work, we set the wind speed $5m/s$, which is larger than the flutter speed when $x_\alpha = 0.2$. For this wind speed, the maximum harvested power is obtained for $k_{\alpha_2} = -6N.m$, as shown in Figure 7.3. Clearly, the use of the normal form, although applicable only near the bifurcation, is helpful when determining parameter values that ensure a supercritical instability.

7.4 Uncertainties and Sensitivity Analysis of the System Outputs

We quantify uncertainties in the harvester's performance that are associated with variations in the system parameters, including the load resistance, the eccentricity, and the nonlinear coefficients of the flexural and torsional springs. This approach also yields the sensitivity of the harvested power and the plunge and pitch to all parameters while accounting for the combined effects of such variations, which is very important when the nonlinearities are

significant in determining the system's output. The sensitivity analysis makes use of a non-intrusive formulation of the Polynomial Chaos Expansion (PCE). Through the governing equations, uncertainties in the input parameters are introduced and propagated to determine the rate of variation of the harvested power with variations in the input parameters. Using this non-intrusive PCE, we identify the input parameters that have the largest influence on the system output.

7.4.1 Non-intrusive Polynomial Chaos Expansion

An important aspect of spectral representation of uncertainty (203–205) is that it decomposes a random function (or variable) into separate deterministic and stochastic components (206). In this representation, any stochastic variable (i.e., α^*), such as the pitch, plunge, voltage, or power is expressed as

$$\alpha^*(t,\vec{\xi}) = \sum_{i=0}^{Q} \alpha_i(t)\psi_i(\vec{\xi}) \tag{7.11}$$

where $\alpha_i(t)$ is deterministic and represents the amplitude of the i^{th} fluctuation, $\psi_i(\vec{\xi})$ is a random basis function corresponding to the i^{th} mode, and Q is the number of output modes. This number is expressed as $Q+1 = \frac{(n+p)!}{n!+p!}$, where p is the order of the polynomial chaos and n is the number of random variables.

The choice of the polynomial basis is highly dependent on the distribution of the random variables (205). For Gaussian distribution of the random variables, Hermite polynomials are used as basis functions. A convenient form of the Hermite polynomials is given by

$$H_p(\xi_1,..,\xi_n) = (-1)^p e^{\frac{1}{2}\vec{\xi}^T\vec{\xi}} \frac{\partial^p}{\partial(\xi_1)^{c_1}..\partial(\xi_n)^{c_n}} e^{-\frac{1}{2}\vec{\xi}^T\vec{\xi}} \tag{7.12}$$

where $\sum_{i=0}^{n} c_i = p$. This set of polynomials form a complete orthogonal set of functions in the random space with respect to the following inner product:

$$< \psi_i(\vec{\xi}), \psi_j(\vec{\xi}) >= (\frac{1}{\sqrt{(2\pi)^n}}) \int_{-\infty}^{\infty} \psi_i(\vec{\xi})\psi_j(\vec{\xi}) e^{-\frac{1}{2}\vec{\xi}^T\vec{\xi}} d(\vec{\xi}) \tag{7.13}$$

with the density function of the n variate standard Gaussian distribution being the weighting function. We note that

$$< \psi_i, \psi_j >=< \psi_i^2 > \delta_{ij} \tag{7.14}$$

To determine the polynomial representation of the system output, we need to compute the deterministic coefficients α_i. Using the orthogonality condition of the basis functions, we obtain the following relation:

$$\alpha_i = \frac{< \alpha^*(\xi), \psi_i(\xi) >}{< \psi_i^2(\xi) >} \tag{7.15}$$

Three different methods can be used to obtain approximations of the polynomial expansion coefficients: the sampling based method, the quadrature method, and the linear regression method (207; 208). The latter allows for more flexibility in the choice of the sampling points and the use of sampling strategies, such as the Latin Hypercube Sampling (LHS). Another advantage of using this method is that the required number of sampling points is very small compared to the other approaches. This is an important advantage particularly for time consuming computations. This method is based on the following matrix equation:

$$\begin{bmatrix} \alpha_1^* \\ \alpha_2^* \\ . \\ . \\ . \\ \alpha_N^* \end{bmatrix} = \begin{bmatrix} \psi_0(\xi^1) & \psi_1(\xi^1) & . & . & . & \psi_Q(\xi^1) \\ \psi_0(\xi^2) & \psi_1(\xi^2) & . & . & . & \psi_Q(\xi^2) \\ . & . & . & . & . & . \\ . & . & . & . & . & . \\ . & . & . & . & . & . \\ \psi_0(\xi^N) & \psi_1(\xi^N) & . & . & . & \psi_Q(\xi^N) \end{bmatrix} \begin{bmatrix} \alpha_0 \\ \alpha_1 \\ . \\ . \\ . \\ \alpha_Q \end{bmatrix} \tag{7.16}$$

which represents the discretized form of equation (7.11). When N is equal to the number $Q+1$ of polynomials in the expansion, the matrix is square. Therefore, it can be inverted to determine the expansion coefficients α_i from the outputs α_i^*.

As aforementioned, we consider uncertainties in R, x_α, k_{α_2}, and k_{h_2} and study their impacts on the harvested power and pitch and plunge amplitudes. To generate samples, we assume that the uncertainties follow Gaussian distributions. The mean and standard deviation of each considered parameter are given in Table 7.2. The mean values of the electrical load resistance and the eccentricity are chosen to maintain flutter speeds that are smaller than the considered wind speed in the simulations, which is set equal to $5m/s$. Furthermore, the mean values of the nonlinear coefficients of the springs are chosen based on the normal form of the Hopf bifurcation to guarantee a supercritical instability. The α_i^* are determined numerically by using the governing equations (7.1-7.3) for the samples generated

Table 7.2: The mean and standard deviation values for the load resistance, the eccentricity, and the nonlinear coefficients of the springs

Parameter	$R = \mu_1 + \sigma_1\xi_1$	$x_\alpha = \mu_2 + \sigma_2\xi_2$	$k_{\alpha_2} = \mu_3 + \sigma_3\xi_3$	$k_{h_2} = \mu_4 + \sigma_4\xi_4$
μ_i	$10^6\ \Omega$	0.2	$10\ Nm$	$60\ N/m$
σ_i	$10^5\ \Omega$	0.02	$1\ Nm$	$6\ N/m$

based on a Latin Hypercube Sampling methodology. Then, we use the linear regression method to determine the PCE coefficients. Because the relationship between the input and output parameters is nonlinear, the sensitivity of the output α^* to changes in the i-th input parameter ξ_i is given by

$$\frac{\partial \alpha^*}{\partial \xi_i}(\xi) = \sum_{\mathbf{p=0}}^{\mathbf{Q}} \alpha_{\mathbf{p}} \frac{\partial \psi_{\mathbf{p}}(\xi)}{\partial \xi_{\mathbf{i}}} \tag{7.17}$$

Determining these sensitivities facilitates the identification of the variations that would impact the level of the harvested power.

7.5 Results and Discussions

Figures 7.5-a, 7.5-b, and 7.5-c show the empirical density functions of the harvested power, plunge amplitude, and pitch amplitude, respectively and that are associated with the variations presented in Table 7.2. These probability density functions of the output parameters were computed from 450 realizations based on the Monte Carlo simulations (MCs). We note that, for all system outputs, the seventh-order non-intrusive PCE is needed, as a minimum, to obtain excellent agreement with the MC. This is due to the fact that the relationship between the input parameters and the system outputs is nonlinear.

Tables 7.3 and 7.4 show the sensitivity of the harvested power and the plunge and pitch amplitudes to variations in the system's parameters including the load resistance, the eccentricity, the nonlinear coefficients of the springs, and the nondimensional uncertain parameters (ξ_i), respectively. The results show that increasing the eccentricity and the nonlinear coefficient of the torsional spring results in a decrease in the harvested power and the plunge

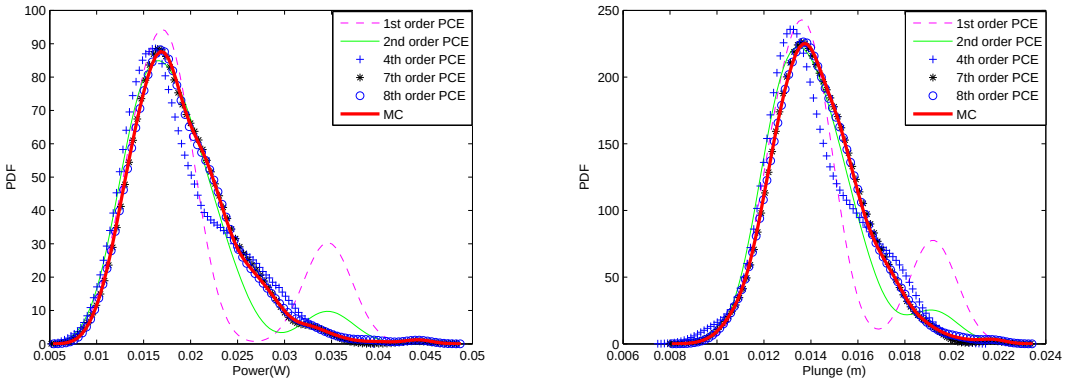

(a) (b)

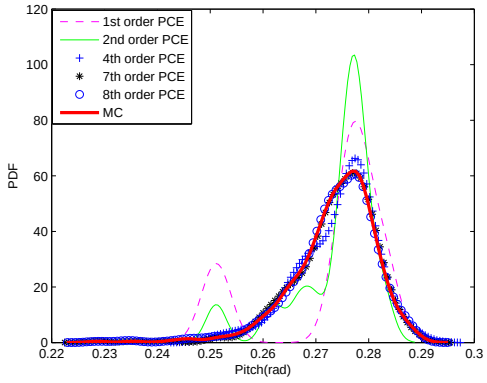

(c)

Figure 7.4: Probability density functions of the (a) harvested power, (b) plunge amplitude, and (c) pitch amplitude when using the Monte Carlo simulations and the first, second, fourth, seventh, and eighth non-intrusive PCE orders

Table 7.3: Sensitivity analysis of the harvested power and the plunge and pitch amplitudes to variations in the load resistance, the eccentricity, and the nonlinear coefficients of the springs

Parameter (γ_i)	R	x_α	$k_{\alpha 2}$	k_{h2}
$\partial P/\partial\gamma_i$	1.4746×10^{-6} $\frac{W}{\Omega}$	-0.96 W	-0.146739 $\frac{W}{Nm}$	0.01043 $\frac{W}{N/m}$
$\partial h/\partial\gamma_i$	2.46819×10^{-6} $\frac{m}{\Omega}$	-3.17236 m	-0.31345 $\frac{m}{Nm}$	0.0226985 $\frac{m}{N/m}$
$\partial\alpha/\partial\gamma_i$	-6.3292×10^{-5} $\frac{1}{\Omega}$	-126.44	25.6367 $\frac{1}{Nm}$	-0.34209 $\frac{1}{N/m}$

Table 7.4: Sensitivity of the harvested power and the plunge and pitch amplitudes to ξ_i where ξ_i represents the uncertainty in the system's parameters

Uncertain parameter (ξ_i)	ξ_1	ξ_2	ξ_3	ξ_4
$\partial P/\partial\xi_i$ (W)	0.14746	-0.01923	-0.146739	0.062559
$\partial h/\partial\xi_i$ (m)	0.00247	-0.06345	-0.31345	0.13619
$\partial\alpha/\partial\xi_i$	-0.53292	-2.5288	25.6367	-2.0525

amplitude. On the other hand, increasing the load resistance and the nonlinear coefficient of the plunge spring results in an increase in the harvested power. Based on the sensitivity magnitudes in Table 7.3, variations in the eccentricity are the most influential on the system outputs. Moreover, variations in the load resistance are small in comparison to variations in x_α, $k_{\alpha 2}$, and k_{h2} for the plunge and pitch amplitudes. Furthermore, for the chosen mean values, the load resistance has a negligible impact on the harvested power. We note also that the sensitivities of the different outputs to the nonlinear coefficient of the plunge spring are smaller than those of the nonlinear coefficient of the pitch spring and the eccentricity. Inspecting Table 7.4, we note that $\partial P/\partial\xi_1$ and $\partial P/\partial\xi_3$ are larger than $\partial P/\partial\xi_2$ and $\partial P/\partial\xi_4$ for the same fractional values ξ_1, ξ_2, ξ_3, and ξ_4. This show that fractional variations in the load resistance and the nonlinear coefficient of the torsional spring have a larger influence on the harvested power than those of the eccentricity and the nonlinear coefficient of the plunge spring. In addition, decreasing the nonlinear coefficient of the torsional spring decreases the pitch amplitude and increases the plunge amplitude and hence the harvested power. This is expected because energy harvesting is associated with the plunge.

7.6 Conclusions

A stochastic approach is presented to evaluate uncertainties in the performance associated with variations in design parameters of an energy harvester. The sensitivities of the harvested power to variations in the load resistance, the eccentricity (distance between the center of mass and the elastic axis), and the nonlinear coefficients are also determined. As a first step, we used the normal form of the Hopf bifurcation to determine the type of instability and select nonlinear coefficients of the springs that produce supercritical Hopf bifurcations. Moreover, the non-intrusive formulation of the Polynomial Chaos Expansion in terms of the multivariate Hermite polynomials was employed to quantify the sensitivities in the harvested power, plunge amplitude, and pitch amplitude. The results show that the relationship between the input parameters and the harvested power is highly nonlinear. The results show also that the generated power is most sensitive to variations in the eccentricity and that the nonlinear coefficient of the plunge spring is less influential than the nonlinear coefficient of the torsional spring on the harvester's performance.

Part III

Cylinder-based Piezoelectric Energy Harvesters from Vortex-Induced Vibrations

Chapter 8

Phenomena and Modeling of Cylinder-based Piezoaeroelastic Energy Harvesters

A well-know phenomenon in bluff body aerodynamics is the alternate shedding of vortices and the associated unsteady aerodynamic forces acting on it. When these vortices shed at a frequency near a natural frequency of the bluff body, lock-in or synchronization takes place and resonant transverse vibrations occur. These vibrations are referred to as vortex-induced vibrations (VIV). The objective of this chapter is to investigate the possibility of using VIV oscillations of structures to harvest energy. Particularly, we aim to determine the power levels that can be generated from VIV oscillations of a circular cylinder and variations of these levels with either the freestream velocity or the Reynolds number. To this end, we attach a piezoelectric transducer to the transverse displacement degree of freedom of the cylinder.

High-fidelity simulations of the VIV phenomenon are generally very expensive in terms of computing power and time. Such simulations can be significantly complicated if three-dimensional effects, turbulence structures, and elasticity are considered. Consequently, assumptions are often made to produce simple and accurate predictions of the VIV phenomenon and the structural response. Different models based on the van der Pol oscillator or its com-

bination with other nonlinear oscillators have been proposed for VIV oscillations. In this Chapter, we develop a representative coupled VIV-energy harvesting problem. Because of the nonlinear mechanisms associated with these vibrations and energy harvesting, we also aim to assess the effects of the load resistance and initial conditions on the level of the harvested power.

8.1 Mathematical Model

Bishop and Hassan (209) were the first to suggest modeling the lift over a circular cylinder due to vortex shedding by a self-excited oscillator. Hartlen and Currie (210) used a Rayleigh oscillator to model the lift and coupled this oscillator with the motion of the cylinder by a velocity term. A modified van der Pol oscillator was used by Skop and Griffin (92) to represent the lift. Skop and Griffin (95) made a correction to the predicted response frequencies by adding cubic terms to the lift equation. In this work, we use the empirical model of the vortex-induced vibrations of spring-mounted rigid cylinders developed by Skop and Griffin (95). In this model, a modified van der Pol equation is used to represent the lift and is coupled to the equation of motion of the cylinder by a velocity term. As shown in Figure 9.1, a piezoelectric transducer is attached to the transverse displacement of the cylinder to harvest energy.

Th coupling between the cylinder motion and the generated voltage is modeled using the Gauss law. The fluctuating lift coefficient C_L induced on a rigid circular cylinder by the vortex-shedding process is modeled by Skop and Griffin (95) as

$$\ddot{C_L} + \omega_s^2 C_L - [C_{L0}^2 - C_L^2 - (\frac{\dot{C_L}}{\omega_s})^2](\omega_s G \dot{C_L} - \omega_s^2 H C_L) = \omega_s F(\frac{\dot{Y}}{D}) \tag{8.1}$$

where Y is the transverse displacement of the cylinder, D is the diameter of the cylinder, and ω_s is the shedding frequency, which is related to the freestream velocity U by the Strouhal number S. This relation is given by $\omega_s = 2\pi SU/D$. The four coefficients C_{L0}, G, H, and F represent parameters, which can be identified from experimental results. These parameters depend on $S_G = \xi/\mu$, where ξ is the nondimensional damping coefficient and μ is the

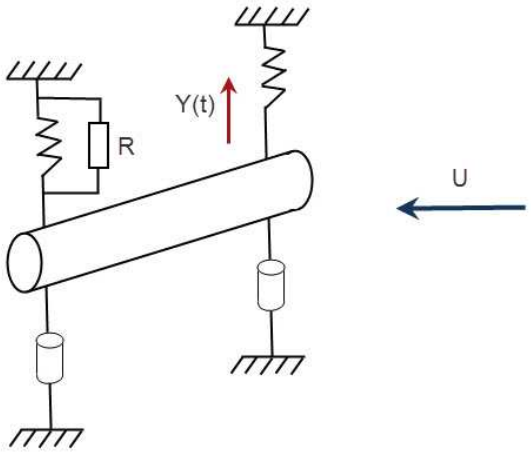

Figure 8.1: Schematic of a piezoelectric energy harvester of a freely oscillating cylinder

nondimensional mass coefficient. Skop and Griffin (95) provided empirical functions for each of these parameters that are valid in the Reynolds number range between 400 and 10^5, over which S and C_{L0} remain constant. These parameters are functions of $S_G = \xi/\mu$ and are given by

$$log_{10}G = 0.25 - 0.21S_G \tag{8.2}$$

$$log_{10}hS_G^2 = -0.24 + 0.66S_G \tag{8.3}$$

$$H = \xi h \tag{8.4}$$

$$F = 4S_G G/h \tag{8.5}$$

The equation of motion of a spring-mounted rigid cylinder that includes the effect of the piezoelectric coupling can be expressed as

$$\frac{\ddot{Y}}{D} + 2\xi\omega_n\frac{\dot{Y}}{D} + \omega_n^2\frac{Y}{D} - \frac{\theta}{MD}V = \frac{\rho U^2 L}{2M}C_L = \mu\omega_s^2 C_L \tag{8.6}$$

where M and L are used to represent the total mass and length of the cylinder and ρ is the fluid density. The natural frequency ω_n and the damping ratio ξ of the spring-mass system

are measured in a stationary fluid having the same physical properties as the used fluid. In equation (9.6), θ is the electromechanical coupling coefficient and V is the harvested voltage across the load resistance. The electromechanical coupling term appears also in the governing equation of the voltage, which is given by the Gauss law and written as (134; 211)

$$C_p\dot{V} + \frac{V}{R} + \theta\dot{Y} = 0 \tag{8.7}$$

where R is the load resistance and C_p is the capacitance of the piezoelectric layer.

8.2 Linear Analysis of the Electromechanical Model

Because the load resistance may affect the structural natural frequency and damping of the harvester, we analyze the coupled electromechanical problem by performing a linear analysis of the governing equation of the cylinder and the Gauss law equation. Using the following state variables:

$$\mathbf{X} = \begin{bmatrix} X_1 \\ X_2 \\ X_3 \end{bmatrix} = \begin{bmatrix} Y \\ \dot{Y} \\ V \end{bmatrix} \tag{8.8}$$

we rewrite the equations of motion as

$$\dot{X}_1 = X_2 \tag{8.9}$$

$$\dot{X}_2 = -2\xi\omega_n X_2 - \omega_n^2 X_1 + \frac{\theta}{M} X_3 \tag{8.10}$$

$$\dot{X}_3 = -\frac{1}{RC_p} X_3 - \frac{\theta}{C_p} X_2 \tag{8.11}$$

These equations can be expressed in the following matrix form:

$$\dot{\mathbf{X}} = B\mathbf{X} \tag{8.12}$$

$$B = \begin{bmatrix} 0 & 1 & 0 \\ -\omega_n^2 & -2\xi\omega_n & \frac{\theta}{M} \\ 0 & -\frac{\theta}{C_p} & -\frac{1}{RC_p} \end{bmatrix}$$

Table 8.1: Parameters of the two considered configurations

Parameter	Description	System 1	System 2
M	Mass (Kg)	1.13×10^{-4}	4.01×10^{-4}
D	Diameter (m)	6×10^{-3}	6×10^{-3}
ξ	Nondimensional damping	4.34×10^{-3}	2.51×10^{-3}
μ	Nondimensional mass	8.62×10^{-3}	2.43×10^{-3}
ω_n	Natural frequency (rad/s)	326.726	188.496
G	First identified parameter	1.397	1.0755
H	Second identified parameter	0.0214	0.00648
F	Third identified parameter	0.567	1.731

where B includes all parameters that affect the linear part of the system. This matrix is used to investigate the effects of the load resistance, damping ratio, and electromechanical coupling coefficients on the structural natural frequency and then on the onset of synchronization. Below, we consider two different configurations, namely, System 1 and System 2 of Skop and Griffin (92). The parameters of these two configurations are presented in Table 9.1.

The matrix B in equation (9.12) has a set of three eigenvalues k_i, $i = 1, 2, 3$. These eigenvalues are arranged so that the first two are complex conjugates; that is, $k_2 = \bar{k}_1$. The third eigenvalue, which is due to the electromechanical coupling, is always negative. These eigenvalues are solutions of the characteristic equation

$$\lambda^3 + (\frac{1}{RC_p\omega_n} + 2\xi)\lambda^2 + (1 + \frac{2\xi}{RC_p\omega_n} + \frac{\theta^2}{MC_p\omega_n^2}) + \frac{1}{RC_p\omega_n} = 0 \tag{8.13}$$

where $\lambda = \frac{k}{\omega_n}$. Clearly, the roots of equation (9.13) depend on all linear system parameters: total mass, damping coefficient, electromechanical coupling coefficients, and load resistance.

Considering the parameters presented in Table 9.1, we obtain from equation (9.13) that For System 1:

$$\lambda^3 + (\frac{25505.6}{R} + 8.68 \times 10^{-3})\lambda^2 + (2.66 + \frac{221.389}{R}) + \frac{25505.6}{R} = 0 \tag{8.14}$$

For System 2:

$$\lambda^3 + (\frac{44209.6}{R} + 5.02 \times 10^{-3})\lambda^2 + (2.41 + \frac{221.932}{R}) + \frac{44209.6}{R} = 0 \tag{8.15}$$

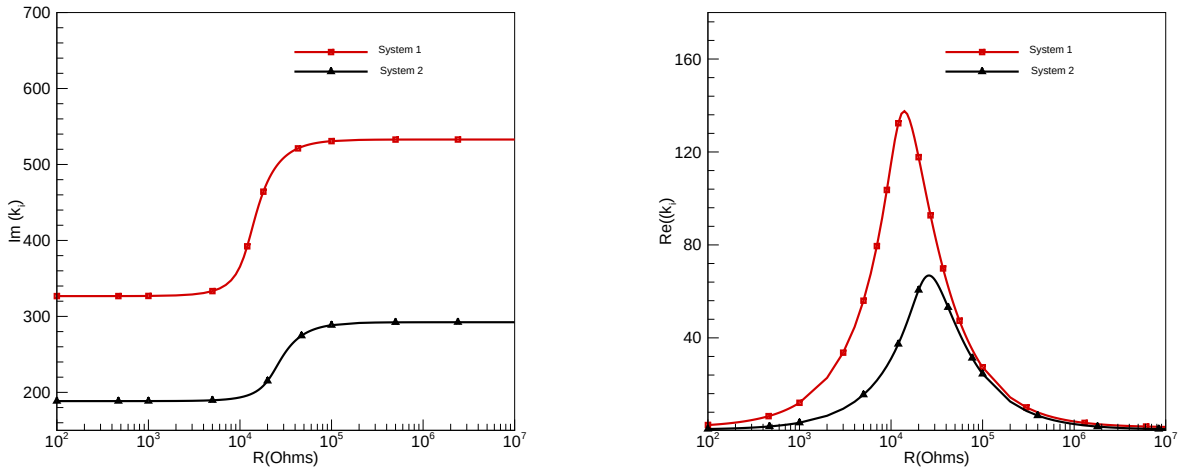

(a) (b)

Figure 8.2: Variations of (a) the imaginary parts and (b) the real parts of the electromechanical model with the load resistance for the two considered system parameters

Clearly, the roots, and hence the eigenvalues, of equations (9.14) and (9.15) depend on the load resistance R. Figure 9.2-a shows variations of the imaginary parts of the complex eigenvalues with the load resistance. In both systems, a steep increase is noted over the load resistance values between $10^4\Omega$ and $10^5\Omega$. The imaginary part of this eigenvalue constitutes the dimensional global frequency. For the parameters of System 1, the dimensional frequency is approximately equal to $326.72 rad/s$ when the load resistance is between $10^2\Omega$ and $10^3\Omega$; we refer to this frequency as the short global frequency. Increasing the load resistance causes an increase in the global frequency with a steep increase to values near $530 rad/s$ when the load resistance is near $R = 10^6\Omega$; we refer to this frequency as the open global frequency. For the parameters of System 2, the short global frequency is approximately equal to $188.496 rad/s$ and the open global frequency is approximately equal to $292.33 rad/s$. We note that the difference between the open and short global frequencies depends on all of the linear parameters.

As for the electromechanical damping, it follows from Figure 9.2-b that it is maximum

for specific values of the load resistance for both considered configurations. We note also that the region of load resistances over which the electromechanical damping is relatively high coincides with the region over which the steep increase in the global frequency occurs. This is true for both configurations. Away from this region, the damping coefficient is small and the global frequency is almost constant for both configurations.

This linear analysis gives a clear idea about the effect of the load resistance on the onset of the synchronization region and the electromechanical damping variations. Particularly, increasing the load resistance can significantly change both of the onset of synchronization and the electromechanical damping. These effects have an impact on the level of harvested power.

8.3 Nonlinear Analysis: Effects of Load Resistance on Synchronization Regime and Harvested Power

We investigate the effect of the load resistance on the cylinder displacement, lift coefficient, and harvested power. Furthermore, we study the effect of the load resistance on the short- and open-circuit configurations.

The dependence of the system response on the freestream velocity is shown in Figures 9.3 and 9.4 for both configurations, respectively. We note that, as the freestream velocity is increased, the synchronization region, defined by the region of higher amplitudes, is varied. Furthermore, we note a clear hardening behavior that is associated with resonances near the global frequencies, 326.72 rad/s for $R = 10^2\Omega$ and 532.83 rad/s for $R = 10^6\Omega$ for the first configuration, and near 188.495 rad/s for $R = 10^2\Omega$ and 292.33 rad/s for $R = 10^6\Omega$ for the second configuration. This behavior is a result of the cubic nonlinearity in the lift coefficient. Furthermore, as the load resistance increases from $10^3\Omega$ to $10^5\Omega$, the region of synchronization shifts to higher freestream velocities for both configurations. However, the hardening response for these values of the load resistance is not as clear as it is for $R = 10^2\Omega$ and $R = 10^6\Omega$ in both configurations.

The fact that changing the load resistance results in a change in the lock-in or synchronization region is expected from the linear analysis, which shows a delay in the onset of

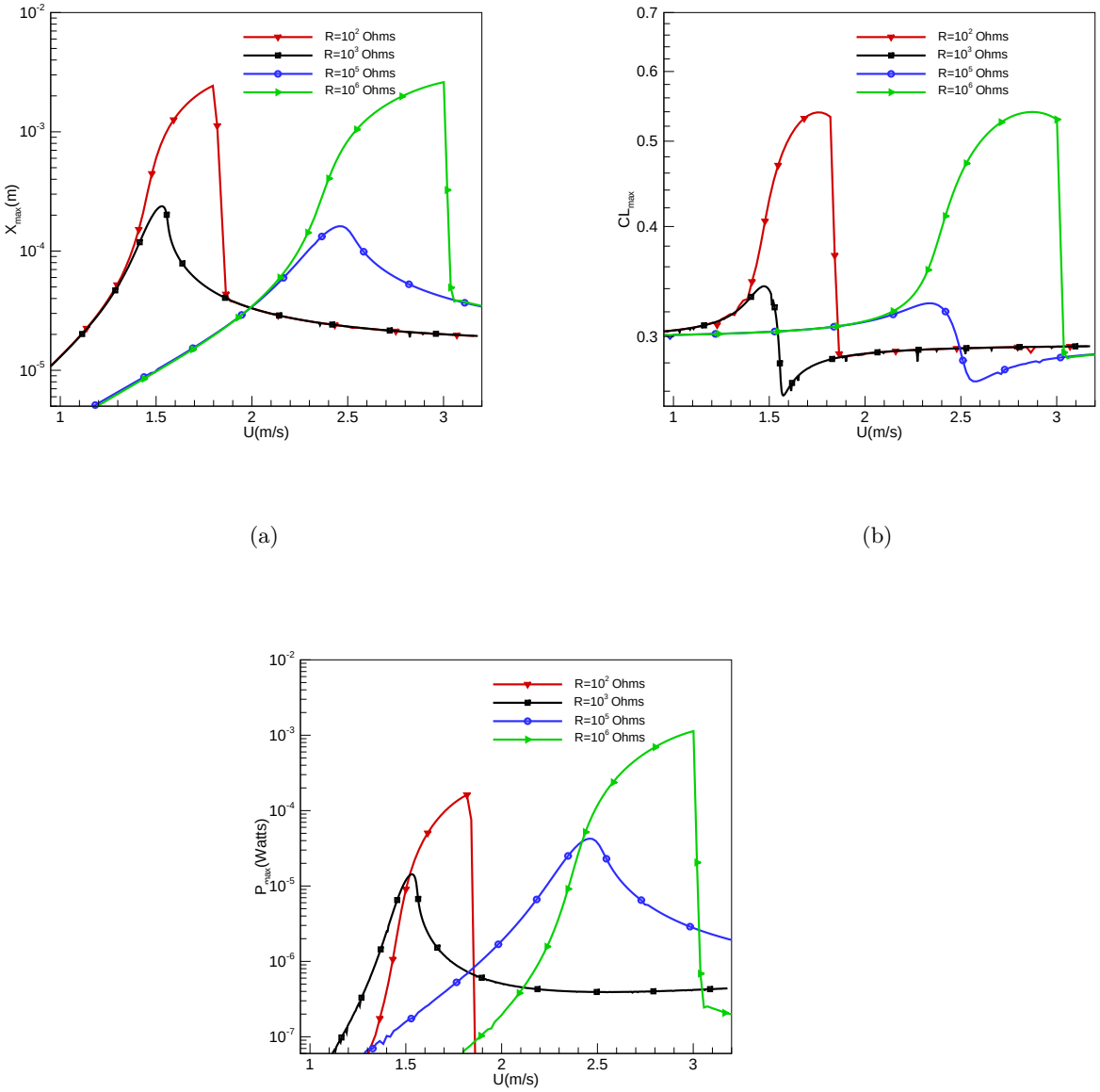

(a)

(b)

(c)

Figure 8.3: Frequency-response curves of the (a) transverse displacement, (b) lift coefficient, and (c) harvested power for different values of the load resistance and for the first configuration

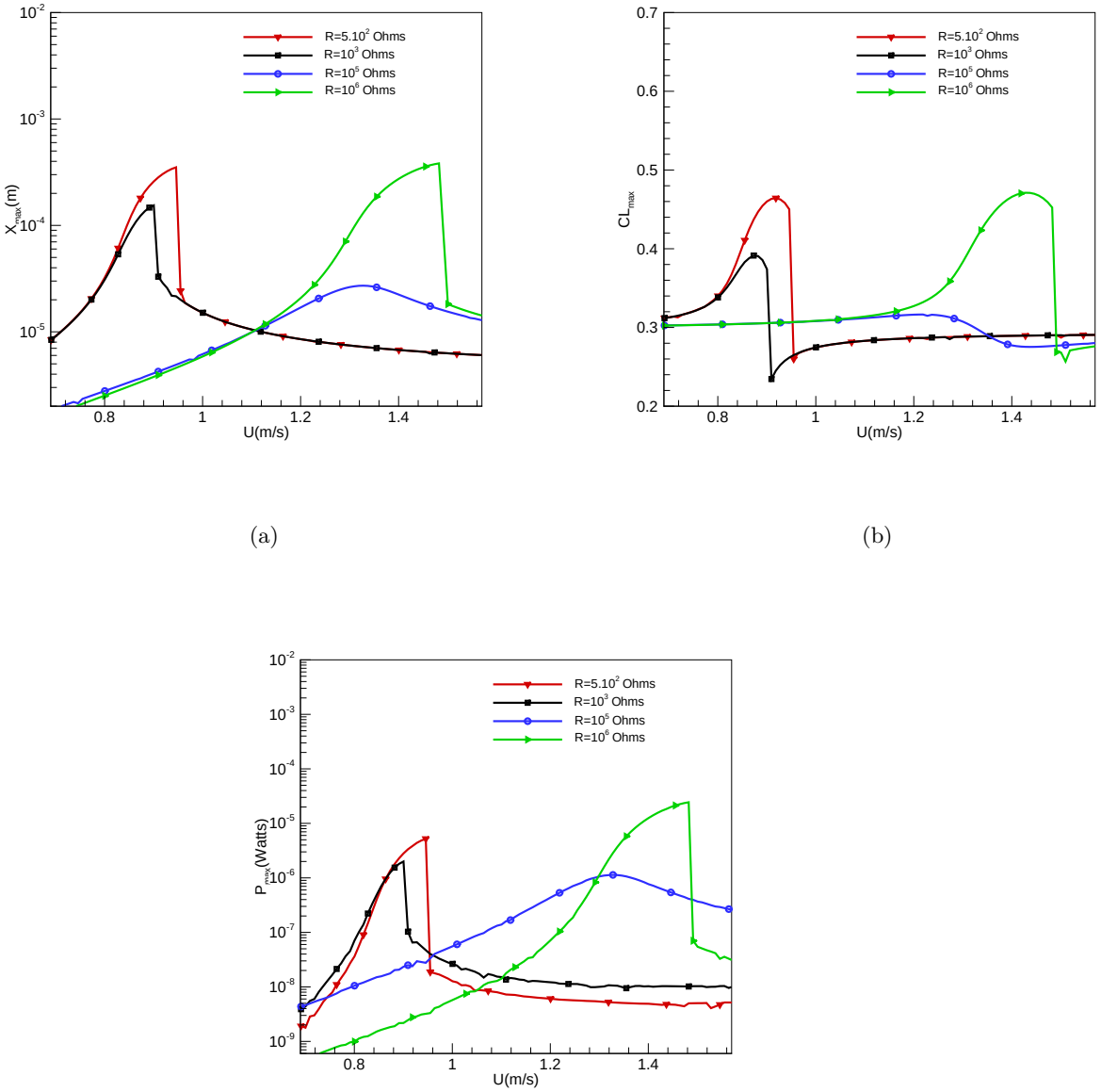

Figure 8.4: Frequency-response curves of the (a) transverse displacement, (b) lift coefficient, and (c) harvested power for different values of the load resistance and for the second configuration

synchronization, in terms of higher freestream velocities, as the load resistance is increased. Furthermore, the high peaks in the transverse displacement when $R = 10^2\Omega$ and $R = 10^6\Omega$ for the first configurations and $R = 5 \times 10^2\Omega$ and $R = 10^6\Omega$ for the second configuration are due to the relatively small electromechanical damping, as aforementioned (Figure 9.2-b). For the first configuration, we note that both maxima of the transverse displacement are small for the case when $R = 10^3\Omega$ and $R = 10^5\Omega$. This result is expected because of the high electromechanical damping associated with these values of the load resistance (Figure 9.2-b). Concerning the second configuration, we note that the maximum transverse displacement is very small when $R = 10^5\Omega$ because, in this case, the electromechanical damping is very large (Figure 9.2-b).

Variation of the maximum of the lift coefficient with the freestream velocity for different values of the load resistance are shown in Figures 9.3-b and 9.4-b for the first and second configurations, respectively. The observed variations when $R = 10^2\Omega$ and $R = 10^6\Omega$ for the first configuration and $R = 5 \times 10^2\Omega$ and $R = 10^6\Omega$ for the second configuration are similar to the variations of the displacement in terms of exhibiting a clear hardening behavior. For resistance values near $10^3\Omega$ and $10^5\Omega$, the lift coefficients are much smaller in comparison to those for $R = 10^2\Omega$ and $R = 10^6\Omega$. Furthermore, we note the possibility of anti-resonance for $R = 10^3\Omega$ and $R = 10^5\Omega$ occurring right after the resonance peak in terms of freestream velocities. Figures 9.3-c and 9.4-c show the harvested power for different resistance values, they show maximum power levels near 0.1 and $1mW$ that can be attained for $R = 10^2\Omega$ and $R = 10^6\Omega$ for the first configuration and maximum power levels near 0.01 and $0.2mW$ that can be attained for $R = 5 \times 10^2\Omega$ and $R = 10^6\Omega$ for the second configuration.

The observed hardening behavior is a result of the nonlinear phenomena associated with vortex-induced vibrations. Although, these nonlinearities can be helpful in enhancing the levels of generated power, they can also cause a drop in the harvested power with a slight increase in the freestream velocity. This is due to the presence of an unstable branch, which renders the response to be dependent on the initial conditions. Figures 9.5-a and 9.5-d show variation of the harvested power for different values of the load resistance. The results clearly show a hysteresis associated with the hardening behavior for $R = 10^2\Omega$ and $R = 10^6\Omega$ for the first configuration. This behavior is not observed at the other considered resistances.

Concerning the second configuration, the results also show a hysteresis associated with the hardening behavior for $R = 5 \times 10^2\Omega$, $R = 10^3\Omega$, and $R = 10^6\Omega$, as shown in Figures 9.6-a, 9.6-b, and 9.6-c.

Figures 9.7 and 9.8 show the short- and open-circuit configurations for the harvested power, voltage outputs, transverse displacement, and lift coefficient for the first and second configurations, respectively. These configurations are defined by setting the shedding frequency equal to the short and open global frequencies for both configurations, which are $326.72rad/s$ and $532.83rad/s$ for the first configuration and $188.495rad/s$ and $292.33rad/s$ for the second configuration. These shedding frequencies are obtained at the freestream velocities of $1.486m/s$ and $2.423m/s$ for $R = 10^2\Omega$ and $R = 10^6\Omega$, respectively, in the first configuration. Concerning the second configuration, the freestream velocities, which correspond to the shedding frequencies of $188.495rad/s$ and $292.33rad/s$, are, respectively, $0.857m/s$ and $1.329m/s$. The results show optimum values of the load resistance for both of the short- and open-circuit configurations for which the harvested power is maximized. The harvested power is maximum in the short- and open-circuit configurations when the load resistance is set equal to $R = 600\Omega$ and $R = 3 \times 10^5\Omega$, respectively, for the first configuration. For the second configuration, the harvested power is maximum in the short- and open-circuit configurations when the electrical load resistance is approximately equal to $R = 700\Omega$ and $R = 4 \times 10^5\Omega$, respectively. For both short- and open-circuit configurations, the generated voltage increases as the load resistance is increased and reaches a constant value. We note that, for the short-circuit configuration, an increase in the load resistance is followed by a decrease in the transverse displacement and lift coefficient before stabilizing at larger values. In the open-circuit configuration, an increase in the load resistance is accompanied with an increase in the transverse displacement and lift coefficient.

8.4 Conclusions

We investigate harvesting energy from vortex-induced vibrations (VIV) of a rigid circular cylinder by attaching a piezoelectric transducer to the transverse degree of freedom. We develop the coupled equations governing the lift, cylinder motion, and generated voltage. The

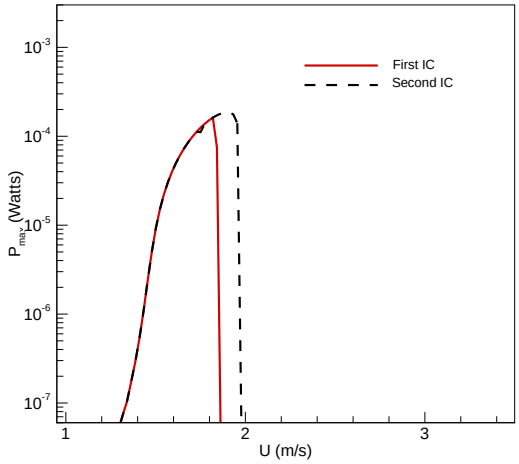

(a) $R = 10^2\Omega$

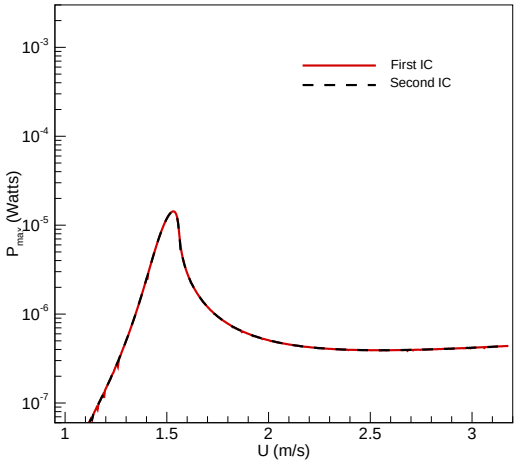

(b) $R = 10^3\Omega$

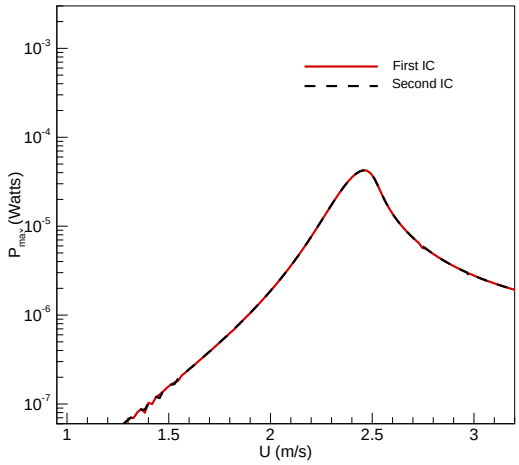

(c) $R = 10^5\Omega$

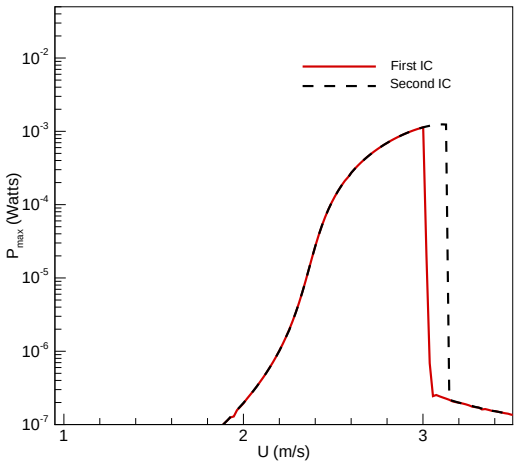

(d) $R = 10^6\Omega$

Figure 8.5: Frequency-response curves of the harvested power for the first configuration and for different values of the load resistance when using different initial conditions

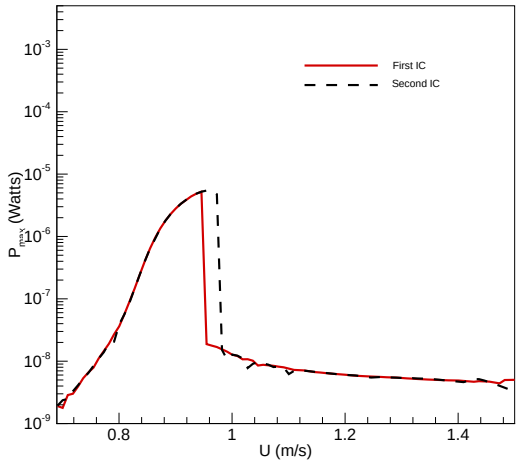

(a) $R = 5.10^2\Omega$

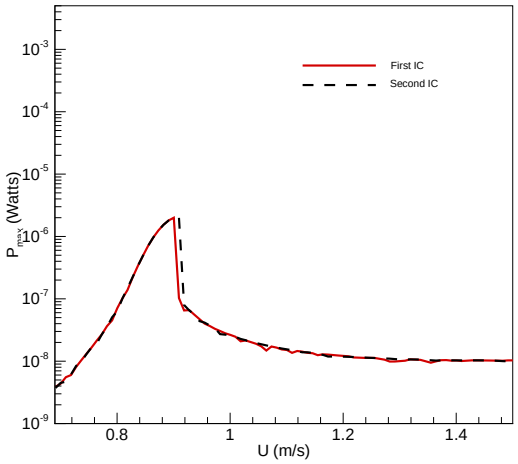

(b) $R = 10^3\Omega$

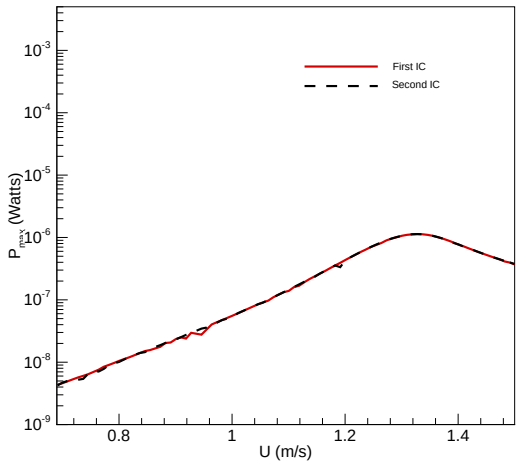

(c) $R = 10^5\Omega$

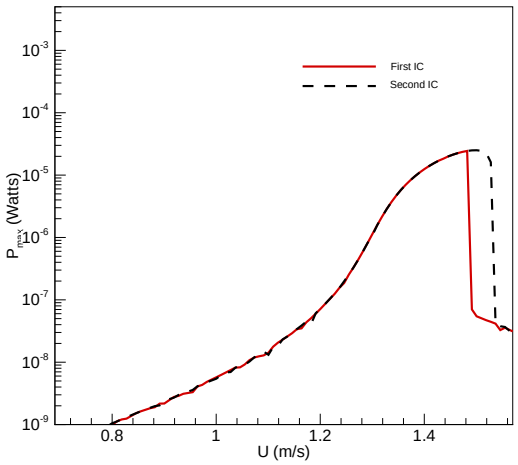

(d) $R = 10^6\Omega$

Figure 8.6: Frequency-response curves of the harvested power for the second configuration and for different values of the load resistance when using different initial conditions

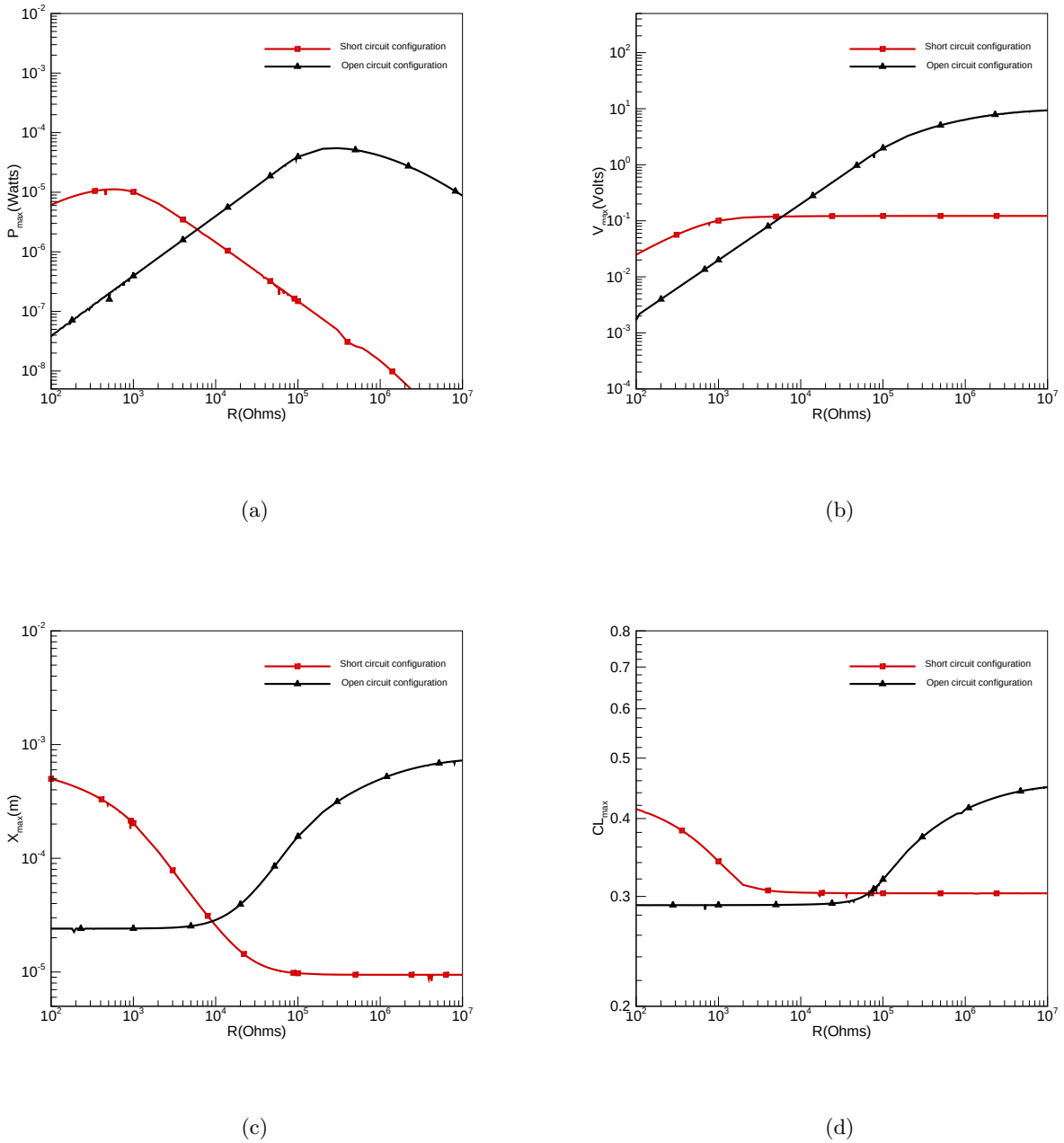

Figure 8.7: Variations of (a) the harvested power, (b) voltage output, (c) maximum transverse displacement, and (d) maximum lift coefficient, for the first configuration, with the load resistance for the short- and open-circuit configurations

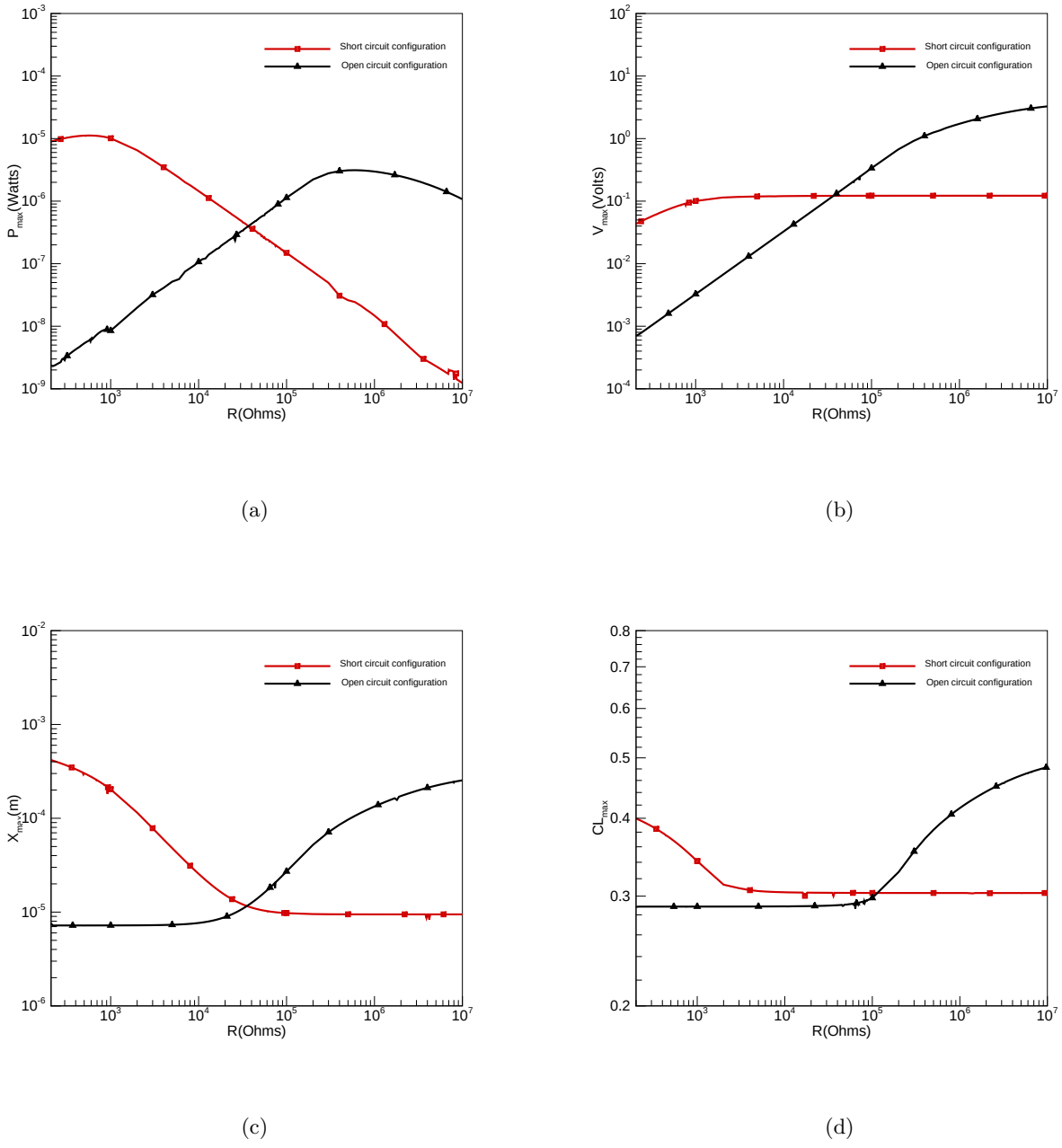

Figure 8.8: Variations of (a) the harvested power, (b) voltage output, (c) maximum transverse displacement, and (d) maximum lift coefficient, for the second configuration, with the load resistance for the short- and open-circuit configurations

lift on the oscillating cylinder is modeled by a modified van der Pol equation and the Gauss law is used to model the coupling between the generated voltage and the cylinder motion for two different configurations. The results show that the load resistance influences the onset of the synchronization (the shedding frequency is equal to the cylinder frequency) region and its characteristics. Increasing the load resistance shifts the onset of synchronization to higher freestream velocities. A comparison of the results obtained for the two configurations shows that synchronization depends on the linear system parameters. The results also show that the nonlinearity associated with the vortex-induced oscillations results in a hardening behavior and hysteresis. The fast drop in the level of the generated power for some freestream velocities and its dependence on the initial conditions require a careful analysis of the problem of generating power from VIV. These results also show that the harvested power can be the order of 1 mW delivered to a 1 MΩ load resistance. Variations in the synchronization region and an the drop in the lift coefficient and cylinder motion associated with energy harvesting from piezoelectric transducers suggest also the potential of using them for VIV control in different regions of freestream velocities.

Chapter 9

Summary and Conclusions

The research performed in this Dissertation has been mainly motivated by developing global nonlinear analyses for piezoelectric energy harvesters from ambient and aeroelastic vibrations. The objectives are to design and enhance the performance of different types of piezoelectric energy harvesters. Various representative models have been developed to predict the performance of these harvesters. In this chapter, we summarize these results and present concluding remarks.

Three different concepts were investigated. They include harvesting energy from base excitations, wing-based energy harvesting from aeroelastic vibrations, and VIV-based energy harvesting.

9.1 Harvesting Energy from Base Excitations

For the case of harvesting energy from base excitations, the harvester is usually subjected to random excitations with several dominant frequencies. These multifrequency excitations have different amplitudes and various directions. In Chapters 2 and 3, we developed innovative global nonlinear distributed-parameter models for piezoelectric energy harvesting from direct (i.e., excited in a direction perpendicular to the beam length) and parametric (i.e., excited in a direction parallel to the beam length) excitations. The harvester consists of a unimorph piezoelectric cantilever beam with a tip mass. The mechanics of this cantilever beam is based on the nonlinear Euler-Bernoulli theory. These models account for geometric, iner-

tia, piezoelectric, and fluid drag (only in the parametric case) nonlinearities. The developed reduced-order models are based on the Galerkin discretization of the governing equations that were derived from the extended Hamilton principle and Gauss law. The method of multiple scales was then used to determine analytical expressions for the steady-state beam deflection, output voltage, and harvested power near the first global resonance (direct excitation) and the first principal parametric resonance (parametric excitations). The results show that one- or two- mode approximations in the Galerkin procedure are not sufficient to accurately predict the performance of the harvester. Furthermore, the effects of the nonlinear piezoelectric coupling, quadratic damping (parametric case), and the excitation amplitude on the output voltage and harvested power were quantified. The results showed that the nonlinear piezoelectric coefficients have an important impact on the harvester behavior in terms of hardening or softening. These results show that a nonlinear distributed-parameter model that takes into consideration the first three modes is better suited than a lumped-parameter approach for the design of energy harvesters and for validation through system identification of experimental setups.

9.2 Wing-based Energy Harvesting from Aeroelastic Excitations

In the second part of this Dissertation, we focused on the modeling, design, and enhancement of wing-based piezoaeroelastic energy harvesters. The harvester is composed of a rigid airfoil that is constrained to pitch and plunge and supported by linear and nonlinear torsional and flexural springs with a piezoelectric transducer attached to the plunge degree of freedom. We performed a linear analysis to study the effects of the linear spring coefficients and the electrical load resistance on the linear flutter speed. This analysis show that the effect of the load resistance on the flutter speed is negligible in comparison to the effects of the linear spring coefficients. Then, we derived the normal form of the Hopf bifurcation to investigate the effects of the structural and aerodynamic nonlinearities on the system's stability near bifurcation. This nonlinear normal form is useful to characterize the effects of different parameters on the system's output and ensure that subcritical or "catastrophic" bifurcations do not take place.

Numerical simulations of the coupled equations of motion were performed to determine the effects of the load resistance and the nonlinear torsional and flexural spring coefficients on the limit-cycle oscillations in pitch and plunge, the voltage output, and harvested power. Based on these results, we have characterized the subcritical behavior of the harvester and determined optimal values of the load resistance that yield maximum harvested power.

To harvest energy at low freestream velocities, we designed, in Chapter 5, the linear spring coefficients of piezoaeroelastic energy harvesters to produce minimum flutter speed. Then, we implemented a linear velocity feedback to decrease the flutter speed to any desired value. These strategies give the possibility to generate energy at low freestream velocities. Then, we used the Center-Manifold theorem to derive the normal form of the Hopf bifurcation near the flutter onset. We used the nonlinear normal form to design nonlinear spring coefficients that (a) produce supercritical bifurcations and (b) maximize the harvester outputs, including the generated power. This proposed approach for design has been validated by numerically integrating the coupled nonlinear differential equations. The results showed that the harvester may undergo a secondary Hopf bifurcation resulting in complex motions. These responses may result in a reduction in the generated power.

In Chapter 6, we investigated the effects of the eccentricity (distance between the gravity axis and elastic axis) on the pitch, plunge, and harvested power. An analysis based on the normal form of the Hopf bifurcation yields a characterization of the effect of the eccentricity on the critical values of the nonlinear spring coefficients that result in large harvested power and yet avoid jumps and hysteresis. The results show that the harvested power can be increased by an order of magnitude by properly choosing small eccentricities and convenient load resistance and designing the harvester to operate optimally at the prevailing wind speeds.

In order to evaluate the uncertainties associated with variations in design parameters of a wing-based piezoaeroelastic energy harvesting, we employ a stochastic approach based on the non-intrusive formulation of the Polynomial Chaos Expansion in Chapter 7. This formulation is based on the Hermite polynomials and it was used to quantify the effects of variations in the load resistance, eccentricity, and nonlinear spring coefficients on the level of the generated power. The nonlinear normal form was used to determine the type of instability and select the nonlinear spring coefficients that produce supercritical Hopf bifurcations. The results

show that the relationship between the input parameters and the harvested power is highly nonlinear. The results also show that the generated power is most sensitive to variations in the eccentricity and that the nonlinear coefficient of the plunge spring is less influential than the nonlinear coefficient of the torsional spring on the harvester's performance.

9.3 Cylinder-based Energy Harvesting from Aeroelastic Excitations

In Chapter 8, we investigated the concept of harvesting energy from vortex-induced vibrations of a rigid circular cylinder by attaching a piezoelectric transducer to the transverse degree of freedom. We developed the coupled equations governing the lift, cylinder motion, and generated voltage. The lift on the oscillating cylinder was modeled by a modified van der Pol equation and Gauss law was used to model the coupling between the output voltage and the cylinder motion. Linear analysis of the electromechanical model was performed to determine the effects of the load resistance on the natural frequency of the rigid cylinder and the onset of synchronization region for energy harvesting. The results showed that the load resistance influences the onset of the synchronization region and its characteristics. The impacts of the nonlinearities on the cylinder's response and energy harvesting were investigated. The results show that the nonlinearity associated with vortex-induced oscillations results in a hardening behavior and hysteresis.

Bibliography

[1] Huesgan, T., Woias, P., and Kockmann, N., "Design and fabrication of MEMS thermoelectric generators with high temperature efficiency," *Sensors and Actuators A: Physical*, Vol. 145-146, 2008, pp. 423–429.

[2] Norman, B. C., "Power options for wireless sensor networks," *IEEE Aerospace and Electronic Systems Magazine*, Vol. 22, 2007, pp. 14–17.

[3] Beeby, S. P., Tudor, M. J., and White, N. M., "Energy harvesting vibration sources for microsystems applications," *Measurement Science Technology*, Vol. 17, 2006, pp. 175–195.

[4] Muralt, P., "Ferroelectric Thin Films for Micro-Sensors and Actuators: a review," *Journal of Micromechanics and Microengineering*, Vol. 10, 2000, pp. 136–146.

[5] Gurav, S. P., Kasyap, A., Sheplak, M., Cattafesta, L., Haftka, R. T., Goosen, J. F. L., and Keulen, F. V., "Uncertainty-based design optimazation of a micro piezoelectric composite energy reclamtation device," *Proc.* 10^{th} *AIAA/ISSSMO Multidisciplinary Analysis and Optimization Conference*, 2004, pp. 3559–3570.

[6] Zhou, W., Liao, W. H., and Li, W. J., "Analysis design of a self-powered piezoelectric microaccelerometer," *Proc. Smart Structures and Materials Conference. SPIE*, Vol. 5763, 2005, pp. 233–240.

[7] Inman, D. J. and Grisso, B. L., "Towards autonomous sensing," *Smart Structures and Materials Conference SPIE*, Vol. 6174, 2006, pp. 61740T.

[8] Roundy, S. and Wright, P. K., "'Energy Efficient Mobile Wireless Sensor Networks," *Journal of Intelligent Materials and Structures*, Vol. 16, 2005, pp. 809–823.

[9] Capel, I. D., Dorrell, H. M., Spencer, E. P., and Davis, M. W., "The amelioration of the suffering associated with spinal cord injury with subperception transcranial electrical stimulation," *Spinal Cord*, Vol. 41, 2003, pp. 109–117.

[10] Priya, S., Popa, D., and Lewis, F., "A piezoelectric vibration-based generator for wireless electronics," *Proc. ASME International Mechanical Engineering Congress Exposition, Chicago, IL*, Vol. 13, 2006, pp. 1131–1142.

[11] Magoteaux, K. C., Sanders, B., and Sodano, A. H., "Investigation of an energy harvesting small unmanned air vehicle," *Proceedings of the SPIE, San Diego, CA*, Vol. 6928, 2008, pp. 1–11.

[12] Arnold, D., "Review of microscale magnetic power generation," *IEEE Transactions Magnetics*, Vol. 43, 2007, pp. 3940–3951.

[13] Glynne-Jones, P., Tudor, M. J., Beeby, S. P., and White, N. M., "An electromagnetic, vibration-powered generator for intelligent sensor systems," *Sensors Actuators A*, Vol. 110, 2004, pp. 344–349.

[14] Mitcheson, P., Miao, P., Start, B., Yeatman, E., Holmes, A., and Green, T., "MEMS electrostatic micro-power generator for low frequency operation," *Sensors Actuators A*, Vol. 115, 2004, pp. 523–529.

[15] Anton, S. R. and Sodano, H. A., "A review of power harvesting using piezoelectric materials (2003-2006)," *Smart Materials and Structures*, Vol. 16, 2007, pp. 1–21.

[16] Cook-Chennault, K. A., Thambi, N., and Sastry, A. M., "Powering MEMS portable devices-a review of non-regenerative and regenerative power supply systems with emphasis on piezoelectric energy harvesting systems," *Smart Materials and Structures*, Vol. 17, 2008, pp. 043001.

[17] Erturk, A., "Electromechanical modeling of piezoelectric energy harvesters," *PhD Dissertation, Virginia Polytechnic Institute and State University*, 2009.

[18] Kim, H. S., Kim, J. H., and Kim, J., "A review of piezoelectric energy harvesting based on vibration," *International Journal of Presicion Engineering and Manufacturing*, Vol. 12, 2011, pp. 1129–1141.

[19] Sodano, H. A., Park, G., and Inman, D. J., "A review of power harvesting using piezoelectric materials," *Shock Vibration Digest*, Vol. 36, 2004, pp. 197–206.

[20] Sodano, H. A., Park, G., and Inman, D. J., "Estimation of electric charge output for piezoelectric energy harvesting," *Strain*, Vol. 40, 2004, pp. 49–58.

[21] Priya, S., "Advances in energy harvesting using low profile piezoelectric transducers," *Journal of Electroceramics*, Vol. 19, 2007, pp. 167–184.

[22] Erturk, A. and Inman, D. J., "Issues in mathematical modeling of piezoelectric energy harvesters," *Smart Materials and Structures*, Vol. 17, 2008, pp. 065016.

[23] Erturk, A. and Inman, D. J., "A distributed parameter electromechanical model for cantilevered piezoelectric energy harvesters," *ASME Journal Vibration and Acoustics*, Vol. 130, 2008, pp. 041002.

[24] Erturk, A. and Inman, D. J., "An experimentally validated bimorph cantilever model for piezoelectric energy harvesting from base excitations," *Smart Materials and Structures*, Vol. 18, 2009, pp. 025009.

[25] Erturk, A., Renno, J. M., and Inman, D. J., "Modeling of a piezoelectric energy harvesting from an L-shaped beam-mass structure with an application to UAVs," *Journal of Intelligent Materials Systems and Structures*, Vol. 20, 2009, pp. 529–544.

[26] Renno, J. M., Daqaq, M. F., and Inman, D. J., "On the optimal energy harvesting from a vibration source," *Journal of Sound and Vibration*, Vol. 320, 2009, pp. 386–405.

[27] Erturk, A., Tarazaga, P. A., Farmer, J. R., and Inman, D. J., "Effect of strain nodes and electrode configuration on piezoelectric energy harvesting from cantilevered beams," *ASME Journal Vibration and Acoustics*, Vol. 131, 2009, pp. 011010.

[28] Stanton, S. C., Erturk, A., Mann, B. P., and Inman, D. J., "Nonlinear piezoelectricity in electroelastic energy harvesters: Modeling and experimental identification," *Journal of Applied Physics*, Vol. 108, 2010, pp. 074903.

[29] Abdelkefi, A., Najar, F., Nayfeh, A. H., and Ayed, S. B., "An energy harvester using piezoelectric cantilever beams undergoing coupled bending-torsion vibrations," *Smart Materials and Structures*, Vol. 20, 2011, pp. 115007.

[30] Abdelkefi, A., Nayfeh, A. H., and Hajj, M. R., "Global nonlinear distributed-parameter model of parametrically excited piezoelectric energy harvesters," *Nonlinear Dynamics*, Vol. 67, 2011, pp. 1147–1160.

[31] Abdelkefi, A., Nayfeh, A. H., and Hajj, M. R., "Effects of nonlinear piezoelectric coupling on energy harvesters under direct excitation," *Nonlinear Dynamics*, Vol. 67, 2011, pp. 1221–1232.

[32] Erturk, A., "Piezoelectric energy harvesting for civil infrastructure system applications: moving loads and surface strain fluctuations," *Journal of Intelligent Material Systems and Structures*, Vol. 22, 2011, pp. 1959–1973.

[33] Karami, A., Bilgen, O., Inman, D. J., and Friswell, M. I., "Experimental and analytical parametric study of single-crystal unimorph beams for vibration energy harvesting," *IEEE Transactions on Ultrasonics, Ferroelectrics, and Frequency Control*, Vol. 58, 2011, pp. 1508–1520.

[34] Karami, A., "Micro-scale and nonlinear vibrational energy harvesting," *PhD Dissertation, Virginia Polytechnic Institute and State University*, 2011.

[35] Daqaq, M. F., "On intentional introduction of stiffness nonlinearities for energy harvesting under white Gaussian excitations," *Nonlinear Dynamics*, 2012, pp. 1–17.

[36] Abdelkefi, A., Nayfeh, A. H., Hajj, M. R., and Najar, F., "Energy harvesting from a multifrequency response of a tuned bending-torsion system," *Smart Materials and Structures*, Vol. 21, 2012, pp. 075029.

[37] Lee, C. S., Joo, J., Han, S., Lee, J. H., and Koh, S. K., "Poly(vinylidene fluoride) transducers with highly conducting poly(3,4-ethylenedioxythiophene) electrodes," *Proceeding International Conference on Science and Technology of Synthetic Metals*, Vol. 152, 2005, pp. 49–52.

[38] Kymissis, J., Kendall, C., Paradiso, J., and Greshenfeld, N., "Parasitic power harvesting in shoes," *In the second IEEE International Conference on Wearable Computing*, 1998, pp. 132–139.

[39] Lee, C., Joo, J., Han, S., and Koh, S., "Multifunctional transducer using poly(vinylidene fluoride) active layer and highly conducting poly(3,4-ethylenedioxythiophene) electrode: actuator and generator," *Applied Physics Letters*, Vol. 85, 2004, pp. 1841–1843.

[40] Sodano, H. A., Inman, D. J., and Park, G., "Comparison of piezoelectric energy harvesting devices for recharging batteries," *Journal of Intelligent Material Systems and Structures*, Vol. 16, 2005, pp. 799–807.

[41] Zhu, D. and Beeby, S., "Kinetic energy harvesting," *In: Energy Harvesting Systems: Principles, Modeling and Applications, Springer*, 2011, pp. 1–78.

[42] Baker, J., Roundy, S., and Wright, P., "Alternative geometries for increasing power density in vibration energy scavenging for wireless senor networks," *Proc. 3rd International Energy Conversion Engineering Conference (San Francisco, CA, Aug.)*, 2005, pp. 959–970.

[43] L. M. Miller, E. Halvorsen, T. D. and Wright, P. K., "Modeling and experimental verification of low-frequency MEMS energy harvesting from ambient vibrations," *Smart Materials and Structures*, Vol. 21, 2011, pp. 045029.

[44] Zhu, D., "Vibration energy harvesting: Machinery, vibration, human movement and flow induced vibration," *In: Sustainable Energy Harvesting Technologies - Past, Present and Future*, 2011, pp. 25–54.

[45] Wu, W., chen, Y., Lee, B., He, J., and Peng, Y., "Tunable resonant frequency power

harvesting devices," *Smart Structures and Materials Conference, SPIE*, Vol. 6169, 2006, pp. 55–62.

[46] Shahruz, S. M., "Design of mechanical band-pass filters for energy scavenging," *Journal of Sound and Vibration*, Vol. 292, 2006, pp. 987–998.

[47] Elvin, N. G. and Elvin, A. A., "Effects of axial forces on cantilever piezoelectric resonators for structural energy harvesting," *Strain*, Vol. 47, 2011, pp. 153–157.

[48] Lui, H., Lee, C., Kobayashi, T., and Quan, C., "Investigation of a MEMS piezoelectric energy harvester system with a frequency-widened-bandwidth mechanism introduced by mechanical stoppers," *Smart Materials and Structures*, Vol. 21, 2012, pp. 035005.

[49] Roundy, S. and Zhang, Y., "Toward self-tuning adaptive vibration-based microgenerators," *Smart Structures, Devices, and Systems II*, Vol. 5649, 2005, pp. 373–384.

[50] Masana, R. and Daqaq, M. F., "Electromechanical modeling and nonlinear analysis of axially loaded energy harvesters," *ASME Journal of Vibration and Acoustics*, Vol. 133, 2011, pp. 011007.

[51] C. R. McInnes, D. G. G. and Cartmell, M. P., "Enhanced vibrational energy harvesting using nonlinear stochastic resonance," *Journal of Sound and Vibration*, Vol. 318, 2008, pp. 655–662.

[52] Erturk, A., Hoffman, J., and Inman, D. J., "A piezo-magneto-elastic structure for broadband vibration energy harvesting," *Applied Physics Letters*, Vol. 94, 2009, pp. 254102.

[53] Stanton, S. C., McGehee, C. C., and Mann, B. P., "Nonlinear dynamics for broadband energy harvesting: investigation of a bistable piezoelectric inertial generator," *Physica D, Nonlinear Phenomena*, Vol. 239, 2010, pp. 640–653.

[54] Masana, R. and Daqaq, M. F., "Relative performance of a vibratory energy harvester in mono- and bi-stable potentials," *Journal of Sound and Vibration*, Vol. 330, 2011, pp. 6036–6052.

[55] Adhikari, S., Friswell, M. I., and Inman, D. J., "Piezoelectric energy harvesting from broadband random vibrations," *Smart Materials and Structures*, Vol. 18, 2009, pp. 115005.

[56] Ali, S. F., Friswell, M. I., and Adhikari, S., "Piezoelectric energy harvesting with parametric uncertainty," *Smart Materials and Structures*, Vol. 19, 2010, pp. 105010.

[57] Litak, G., Borowiec, M., Friswell, M. I., and Adhikari, S., "Energy harvesting in a magnetopiezoelastic system driven by random excitations with uniform and Gaussian distributions," *Journal of Theoretical and Applied Mechanics*, Vol. 49, 2011, pp. 757–764.

[58] Gammaitoni, L., Neri, I., and Vocca, H., "Nonlinear oscillators for vibration energy harvesting," *Applied Physics Letters*, Vol. 94, 2009, pp. 164102.

[59] Barton, D., Burrow, S., and Clare, L., "Energy harvesting from vibrations with a nonlinear oscillator," *ASME Journal of Vibration and Acoustics*, Vol. 132, 2010, pp. 0210091.

[60] Daqaq, M. F., "Response of uni-modal duffing type harvesters to random forced excitations," *Journal of sound and Vibration*, Vol. 329, 2010, pp. 3621–3631.

[61] Daqaq, M. F., "Transduction of a bistable inductive generator driven by white and exponentially correlated Gaussian noise," *Journal of sound and Vibration*, Vol. 330, 2011, pp. 2554–2564.

[62] Roundy, S. and Wright, P. K., "A piezoeletcric vibration based generator for wireless electronics," *Smart Materials and Structures*, Vol. 13, 2004, pp. 1131–1142.

[63] N. E. duToit, B. L. W. and Kim, S., "Design considerations for MEMS-scale piezoelectric mechanical vibration energy harvesters," *Integrated Ferroelectrics*, Vol. 71, 2005, pp. 121160.

[64] H. A. Sodano, G. P. and Inman, D. J., "Estimation of electric charge output for piezoelectric energy harvesting," *Strain*, Vol. 40, 2004, pp. 49–58.

[65] Goldschmidtboeing, F. and Woias, P., "Characterization of different bean shapes for piezoelectric energy harvesting," *Journal of Micromachining and Microengineering*, Vol. 18, 2008, pp. 104013.

[66] Leland, E. S. and Wright, P. K., "Resonance tuning of piezoeletcric vibration energy scavenging generators using compressive axil preload," *Smart Material and Structures*, Vol. 15, 2006, pp. 1413–1420.

[67] Zhu, D., Almusallam, A., Beeby, S., Tudor, J., and Harris, N., "A bimorph multi-layer piezoelectric vibration energy harvester," *Proceedings of PowerMEMS 2010, Leuven, Belgium, December 1-3*, 2010.

[68] Mahmoodi, S. N., Jalili, N., and Daqaq, M. F., "Modeling, nonlinear dynamics, and identification of a piezoelectrically actuated microcantilever sensor," *IEEE/ASME Transaction Mechatronic*, Vol. 13, 2008, pp. 58–65.

[69] von Wagner, U. and Hagedorn, P., "Piezo-beam systems subjected to weak electric field: Experiments and modelling of non-linearities," *Journal of Sound and Vibration*, Vol. 256, 2002, pp. 861–872.

[70] von Wagner, U. and Hagedorn, P., "Nonlinear effects of piezoceramics excited by weak electric fields," *Nonlinear Dynamics*, Vol. 31, 2003, pp. 133–149.

[71] Samal, M. K., Seshu, P., Parashar, S., von Wagner, U., Hagedorn, P., Dutta, B. K., and Kushwaha, H. S., "A finite element model for nonlinear behaviour of piezoceramics under weak electric fields," *Finite Elements in Analysis and Design*, Vol. 41, 2005, pp. 1464–1480.

[72] Samal, M. K., Seshu, P., Parashar, S., von Wagner, U., Hagedorn, P., Dutta, B. K., and Kushwaha, H. S., "Nonlinear behaviour of piezoceramics under weak electric fields. Part-I: 3-D finite element formulation," *International Journal of Solids and Structures*, Vol. 43, 2006, pp. 14221436.

[73] Samal, M. K., Seshu, P., Parashar, S., von Wagner, U., Hagedorn, P., Dutta, B. K., and Kushwaha, H. S., "Nonlinear behaviour of piezoceramics under weak electric fields.

Part-II: Numerical results and validation with experiments," *International Journal of Solids and Structures*, Vol. 43, 2006, pp. 14371458.

[74] Hu, Y., Xue, H., Yang, J., and Jiang, Q., "Nonlinear behavior of a piezoelectric power harvester near resonance," *IEEE Transactions on Ultrasonics, Ferroelectrics, and Frequency Control,*, Vol. 53, 2006, pp. 1387–1381.

[75] Maugin, G., *Nonlinear Electromechanical Effects and Applications*, Wold Scientific, Singapore, 1985.

[76] Yang, J., *Analysis of Piezoelectric Devices*, Springer, New York, NY, 2005.

[77] Tiersten, H., "Electroelastic equations for electroded thin plates subject to large driving voltages," *Journal of Applied Physics*, Vol. 74, 1993, pp. 3389–3393.

[78] Triplett, A. and Quinn, D. D., "The effect of non-linear piezoelectric coupling on vibration-based energy harvesting," *Journal of Intelligent Material Systems and Structures*, Vol. 20, 2009, pp. 1959–1967.

[79] Daqaq, M. F., Stabler, C., Qaroush, Y., and Seuaciuc-Osorio, T., "Investigation of power harvesting via parametric excitations," *Journal of Intelligent Material Systems and Structures*, Vol. 20, 2009, pp. 545–557.

[80] Nayfeh, A. H. and Mook, D. T., *Nonlinear Oscillations*, Wiley, New York, NY, 1979.

[81] Dowell, E. H. and Tang, D., "Nonlinear aeroelasticity and unsteady aerodynamics," *AIAA Journal*, Vol. 40, 2002, pp. 1697–1707.

[82] Gilliatt, H. C., Strganac, T. W., and Kurdila, A. J., "An investigation of internal resonance in aeroelastic systems," *Nonlinear Dynamics*, Vol. 31, 2003, pp. 1–22.

[83] Liu, L., Wong, Y. S., and Lee, B. H. K., "Application of the center manifold theory in non-linear aeroelasticity," Vol. 234, 2000, pp. 641–659.

[84] Nuhait, A. O. and Mook, D. T., "Aeroelastic Behavior of Flat Plates Moving Near the Ground," *Journal of Aircraft*, Vol. 47, 2010, pp. 464–474.

[85] Abdelkefi, A., Vasconcellos, R., Marques, F. D., and Hajj, M. R., "Bifurcation analysis of an aeroelastic system with concentrated nonlinearities," *Nonlinear Dynamics*, Vol. 69, 2011, pp. 57–70.

[86] Abdelkefi, A., Vasconcellos, R., Marques, F. D., and Hajj, M. R., "Modeling and identification of freeplay nonlinearity," *Journal of Sound and Vibration*, Vol. 331, 2012, pp. 1898–1907.

[87] Vasconcellos, R., Abdelkefi, A., Marques, F. D., and Hajj, M. R., "Representation and analysis of control surface freeplay nonlineariy," *Journal of Fluids and Structures*, Vol. 31, 2012, pp. 79–91.

[88] Mei, V. and Currie, I., "Flow separation on a vibrating cylinders," *Physics of Fluids*, Vol. 12, 1969, pp. 2248–2254.

[89] Mair, W. A. and Maull, D. J., "Bluff bodies and vortex shedding-a report on Euromech," *Journal of Fluid Mechanics*, Vol. 45, 1971, pp. 209–224.

[90] Berger, E. and Wille, R., "Periodic flow phenomena," *Annual Review of Fluid Mechanics*, Vol. 4, 1972, pp. 313–340.

[91] Parkinson, G., "Mathematical models for flow-induced oscillations of bluff bodies," *Proceedings of the IUTAM-IAHR Symposium on Flow-Induced Structural Vibrations, Karlsruhe*, Vol. 16, 1972, pp. 809–823.

[92] Skop, R. A. and Griffin, O. M., "A model for the vortex-excited resonant response of bluff cylinders," *Journal of Sound and Vibration*, Vol. 27, 1973, pp. 225–233.

[93] Griffin, O. M., Skop, R. A., and Koopmann, G. H., "The vortex-excited resonant vibrations of circular cylinders," *Journal of Sound and Vibration*, Vol. 31, 1973, pp. 235–249.

[94] Iwan, W. and Belvins, R., "A model for vortex-induced oscillation of structures," *ASME Journal of Applied Mechanics*, Vol. 41, 1974, pp. 581–586.

[95] Skop, R. A. and Griffin, O. M., "On a theory for the vortex-excited oscillations of flexible cylindrical structures," *Journal of Sound and Vibration*, Vol. 41, 1975, pp. 263–274.

[96] Griffin, O. M. and Koopmann, G. H., "The vortex-excited lift and reaction forces on resonantly vibrating cylinders," *Journal of Sound and Vibration*, Vol. 54, 1977, pp. 435–448.

[97] Baz, A. and Ro, J., "Active control of flow-induced vibrations of a flexible cylinder using direct velocity feedback," *Journal of Sound and Vibration*, Vol. 4, 1991, pp. 313–340.

[98] Khalak, A. and Williamson, C. H. K., "Investigation of relative effects of mass and damping in vortex-induced vibration of a circular cylinder," *Journal of Wind Engineering and Industrial Aerodynamics*, Vol. 69-71, 1997, pp. 341–350.

[99] Khalak, A. and Williamson, C. H. K., "Fluid forces and dynamics of a hydroelastic structure with very low mass and damping," *Journal of Fluids and Structures*, Vol. 11, 1997, pp. 973–982.

[100] Khalak, A. and Williamson, C. H. K., "Motions, forces and mode transitions in vortex-induced vibrations at low mass-damping," *Journal of Fluids and Structures*, Vol. 13, 1999, pp. 813–851.

[101] Govardhan, R. and Williamson, C. H. K., "Modes of vortex formation and frequency response of a freely vibrating cylinder," *Journal of Fluid Mechanics*, Vol. 420, 2000, pp. 85–130.

[102] Govardhan, R. and Williamson, C. H. K., "Resonance forever: existence of a critical mass and an infinite regime of resonance in vortex-induced vibration," *Journal of Fluid Mechanics*, Vol. 473, 2002, pp. 147–166.

[103] Govardhan, R. and Williamson, C. H. K., "Critical mass in vortex-induced vibration of a cylinder," *European Journal of Mechanics - B/Fluids*, Vol. 23, 2003, pp. 17–27.

[104] Williamson, C. H. K. and Govardhan, R., "Vortex-induced vibrations," *Annual Review of Fluid Mechanics*, Vol. 36, 2004, pp. 413–455.

[105] Hartog, J. P. D., "Mechanical vibrations," *McGraw-Hill, New York*, 1956.

[106] Fung, Y. C., "An introduction to the theory of aeroelasticity," *Dover, New York*, 1993.

[107] Moon, F. C., "Chaotic vibrations," *Wiley, New York*, 1987.

[108] Hodges, D. H. and Pierce, G. A., "Introduction to structural dynamics and aeroelasticity," *Cambridge University Press, Cambridge*, 2002.

[109] Li, D., Guo, S., and Xiang, J., "Aeroelastic dynamic response and control of an airfoil section with control surface nonlineatities," *Journal of Sound and Vibration*, Vol. 329, 2010, pp. 4756–4771.

[110] Woolston, D. S., Runyan, H., and Byrsdsong, T., "Some effects of system nonlinearities in the problem of aircraft flutter," *NACA Technical Report*, Vol. 3539, 1955.

[111] Woolston, D. S., "An investigation of effects of certain types of structural nonlinearities on wing and control surface flutter," *Journal of the Aeronautical Sciences*, Vol. 24, 1957, pp. 1936–1956.

[112] Shen, S. F. and Hsu, C. C., "Analytical results of certain nonlinear flutter problems," *Journal of the Aeronautical Sciences*, Vol. 25, 1958, pp. 136–137.

[113] O'Neil, T., "Nonlinear aeroelastic response-analyses and experiments," *In Proceeding* 34^{th} *AIAA, Aerospace Sciences Meeting and Exhibit, Reno, NV, AIAA Paper 96-0014*, 1996.

[114] Conner, M. D., Tang, D. M., Dowell, E. H., and Virgin, L. N., "Nonlinear behavior of a typical airfoil section with control surface freeplay," *Journal of Fluids and Structures*, Vol. 11, 1996, pp. 89–109.

[115] Trickey, T., "Global and local dynamics of an aeroelastic system with a control surface freeplay nonlinearity," *PhD Dissertation, Duke University*, 2000.

[116] Trickey, T., Virgin, L. N., and Dowell, E. H., "The stability of limit-cycle oscillations in a nonlinear aeroelastic system," *In Proceeding: Mathematical, Physical and Engineering Sciences*, Vol. 458, 2002, pp. 2203–2226.

[117] Lin, C. Y., Crwley, E. F., and Heer, J., "Open and closed-loop results of a strain-actuated active aeroelastic wing," *Journal of Aircraft*, Vol. 33, 1996, pp. 987–994.

[118] Lazarus, K. B., Crwley, E. F., and Lin, C. Y., "Multivariable high authority control of plate-like active structures," *Journal of Guidance and Control Dynamics*, Vol. 19, 1996, pp. 1357–1363.

[119] Lazarus, K. B., Crwley, E. F., and Lin, C. Y., "Multivariable active lifting surface control using strain actuation: Analytical and experimental results," *Journal of Aircraft*, Vol. 34, 1997, pp. 313–321.

[120] Giurgiutiu, V., "Review of smart-materials actuation solutions for aeroelastic and vibration control," *Journal of Intelligent Material Systems and Structures*, Vol. 11, 2000, pp. 525–544.

[121] Brown, E. L., "Integrated strain actuation in aircraft with highly flexible composite wings," *PhD Dissertation, Massachusetts Institute of Technology*, 2003.

[122] McGowan, A. R., Heeg, J., and Lake, R., "Results of wind-tunnel testing from the piezoelectric aeroelastic tailoring investigation," *37th AIAA/ASCE/AHS/ASC Structures Dynamics and Materials Conference, AIAA-96-1511*, 1996.

[123] Agneni, A., Mastroddi, F., and Polli, G. M., "Shunted piezoelectric patches in elastic and aeroelastic vibrations," *Computers & Structures*, Vol. 81, 2003, pp. 91–105.

[124] Agneni, A., Sorbo, M. D., Mastroddi, F., and Polli, G. M., "Multi-modal daping by shunted piezo-patches: Possible aeroelastic applications," *International Journal of Applied Electromagnetic and Mechanics*, Vol. 24, 2006, pp. 1–24.

[125] Schultz, M. R. and Hyer, M. W., "A morphing concept based on unsymmetric composite laminates and piezoceramic MFC actuators," *In: 45th AIAA/ASME/ASCE/AHS/ASC Structures, Structural Dynamics and Materials Conference, Palm Springs, CA*, 2004.

[126] Bilgen, O., Kochersberger, K., Diggs, E., Kurdila, A., and Inman, D. J., "Morphing wing micro-air vehicles via macro-fiber composite actuators," *In: 48th AIAA/ASME/ASCE/AHS/ASC Structures, Structural Dynamics and Materials Conference, Honolulu, Hawaii, AIAA-2007-1785*, 2007.

[127] Sheta, E. F., Moses, R. W., Huttsell, L. J., and Harrand, V. J., "Active control F/A-18 vertical tail buffeting using piezoelectric materials," *In: 44th AIAA/ASME/ASCE/AHS Structures, Structural Dynamics and Materials Conference, Norfolk, VA, AIAA-2003-1887*, 2003.

[128] Wickramasinghe, V. K., Chen, Y., and Zimcik, D. G., "Experimental evaluation of an advanced buffet suppression system on full-scale F/A-18 fin," *Journal of Aircraft*, Vol. 44, 2007, pp. 733–740.

[129] Erturk, A., Bilgen, O., Fontenille, M., and Inman, D. J., "Piezoelectric energy harvesting from macro-fiber composites with an application to morphing wings aircrafts," *Proc. 19th International Conference of Adaptive Structures and Technologies (Monte Verita, Ascona)*, 2008.

[130] Anton, S. R. and Inman, D. J., "Vibration energy harvesting for unmanned air vehicles," *Proceedings of SPIE, San Diego, CA, March*, Vol. 6982, 2008, pp. 10–13.

[131] Bryant, M. and Garcia, E., "Energy harvesting: a key to wireless sensor nodes," *Proceeding SPIE*, Vol. 7493, 2009, pp. 74931W.

[132] Bryant, M. and Garcia, E., "Development of an aeroelastic vibration power harvester," *Proceeding SPIE*, Vol. 7288, 2009, pp. 728812.

[133] Elvin, N. G. and Elvin, A. A., "The flutter response of a piezoelectrically damped cantilever pipe," *Journal of Intelligent Materials Systems and Structures*, Vol. 20, 2009, pp. 2017–2026.

[134] Erturk, A., Vieira, W. G. R., Marqui, C. D., and Inman, D. J., "On the energy harvesting potential of piezoaeroelastic systems," *Applied Physics Letters*, Vol. 96, 2010, pp. 184103.

[135] Marqui, C. D., Erturk, A., and Inman, D. J., "Piezoaeroelastic modeling and analysis of a generator wing with continuous and segmented electrodes," *Journal of Intelligent Materials Systems and Structures*, Vol. 21, 2010, pp. 983–993.

[136] Marqui, C. D., Erturk, A., and Inman, D. J., "An electromechanical finite element model for piezoelectric energy harvester plates," *Journal of Sound and Vibration*, Vol. 327, 2009, pp. 9–25.

[137] Katz, J. and Plotkin, A., "Low speed aerodynamics," *Cambridge University Press, Cambridge*, 2001.

[138] Benini, G. R., Belo, E. M., and Marques, F. D., "Numerical model for the simulation of fixed wings aeroelastic response," *Journal of Brazilian Society of Mechanical Sciences and Engineering*, Vol. 13, 2004, pp. 175–195.

[139] Marqui, C. D., Vieira, W. G. R., Erturk, A., and Inman, D. J., "Modeling and analysis of piezoelectric energy harvesting from aeroelastic vibrations using the doublet-lattice method," *ASME Journal of Vibration and Acoustics*, Vol. 133, 2011, pp. 011003.

[140] Dowell, E. H., Curtiss, H. C., Scalan, R. H., and Sisto, F., "A modern course in aeroelasticity," *Sijthoff and Noordhoff, Alphen and den Rijn, The Netherlands*, 1978.

[141] Doare, O. and Michelin, S., "Piezoelectric coupling in energy harvesting fluttering flexible plates: linear stability analysis and conversion efficiency," *Journal of Fluids and Structures*, Vol. 27, 2011, pp. 1357–1375.

[142] Allen, J. J. and Smits, A. J., "Energy harvesting eel," *Journal of Fluids and Structures*, Vol. 15, 2001, pp. 629–640.

[143] Taylor, G. W., Burns, J. R., Kammann, S. M., Powers, W., and Welsh, T. R., "The energy harvesting eel: a small subsurface ocean/river power generator," *IEEE Journal of Oceanic Engineering*, Vol. 26, 2001, pp. 539–547.

[144] Pobering, S. and Schwesinger, N., "A novel hydropower harvesting device," *Proceeding 2004 International Conference on MEMS, NANO and Smart Systems, ICMENS*, 2004, pp. 480–485.

[145] Sanchez-Sanz, M., Fernandez, B., and Velazquez, A., "Energy harvesting microresonator based on the forces generated by the Karman street around a rectangular prism," *Journal of Microelectromechanical Systems*, Vol. 18, 2009, pp. 449–457.

[146] Wang, D. A. and Ko, D. A., "Piezoelectric energy harvesting from flow-induced vibration," *Journal of Micromechanics and Microengineering*, Vol. 20, 2010, pp. 025019.

[147] Wang, D. A., Pham, H. T., Chao, C. W., and Ko, J. M. C. D. A., "A piezoelectric energy harvester based on pressure fluctuations in Karman vortex street," *World Renewable Energy Congress 2011, Sweden, 8-13 May*, 2011.

[148] Akaydin, H. D., Elvin, N., and Andrepoulos, Y., "Wake of a cylinder: a paradigm for energy harvesting with piezoelectric materials," *Experiments in Fluids*, Vol. 49, 2010, pp. 291–304.

[149] Akaydin, H. D., Elvin, N., and Andrepoulos, Y., "Energy harvesting from highly unsteady fluid flows using piezoelectric materials," *Journal of Intelligent Material Systems and Structures*, Vol. 21, 2010, pp. 1263–1278.

[150] Akaydin, H. D., Elvin, N., and Andrepoulos, Y., "The performance of a self-excited fluidic energy harvester," *Smart Materials and Structures*, Vol. 21, 2012, pp. 025007.

[151] Xie, J., Yang, J., Hu, H., and Chen, X., "A piezoelectric energy harvester based on flow-induced flexural vibration of a circular cylinder," *Journal of Intelligent Material Systems and Structures*, Vol. 23, 2011, pp. 135–139.

[152] Hobbs, W. B., "Piezoelectric energy harvesting: Vortex-induced vibrations in plants , soap films, and arrays of cylinders," 2010.

[153] Hobbs, W. B. and Hu, D. L., "Tree-inspired piezoelectric energy harvester," *Journal of Fluids and Structures*, Vol. 28, 2012, pp. 103–114.

[154] de Langre, E., "Effects of wind on plants," *Annual Review of Fluid Mechanics*, Vol. 40, 2008, pp. 141–168.

[155] Dupont, S. and Brunet, Y., "Impact of forest edge shape on tree stability: a large eddy simulation study," *Foresty*, Vol. 81, 2008, pp. 299–315.

[156] Nayfeh, A. H., Owis, F., and Hajj, M. R., "A model for the coupled lift and drag on a circular cylinder," *Proceedings of DETC03 ASME 2003 Design Engineering Technical*

Conferences and Computers and Information in Engineering Conference, DETC2003-VIB48455, 2003.

[157] Marzouk, O. A., Nayfeh, A. H., Akhtar, I., and Arafat, H. N., "Modeling Steady-state and Transient Forces on a Cylinder," *Journal of Vibration and Control*, Vol. 13, 2007, pp. 1065–1091.

[158] Akhtar, I., Marzouk, O. A., and Nayfeh, A. H., "A van der Pol-Duffing Oscillator Model of Hydrodynamic Forces on Canonical Structures," *Journal of Computational and Nonlinear Dynamics*, Vol. 4, 2009, pp. 041006–1–9.

[159] Marzouk, O. A. and Nayfeh, A. H., "Characterization of the flow over a cylinder moving harmonically in the cross-flow direction," *International Journal of Non-Linear Mechanics*, Vol. 45, 2010, pp. 821–833.

[160] Akhtar, I., Nayfeh, A. H., and Ribbens, C. J., "On the Stability and Extension of Reduced-Order Galerkin Models in Incompressible Flows: A Numerical Study of Vortex Shedding," *Theoretical and Computational Fluid Dynamics*, Vol. 23, 2009, pp. 213–237.

[161] Parkinson, G. V. and Smith, J. D., "The square prism as an aeroelastic nonlinear oscillator," *Quarterly Journal Mechanics and Applied Mathematics*, Vol. 17, 1964, pp. 225–239.

[162] Parkinson, G. V., "Flow-induced structural vibrations," *(A75-15253 04-39) Berlin, Springer-Verlag*, 1974, pp. 81–127.

[163] Parkinson, G. V., "Phenomena and modelling of flow-induced vibrations of bluff bodies," *Progress in Aerospace Sciences*, Vol. 26, 1989, pp. 169–224.

[164] Novak, M. and Tanaka, H., "Effect of turbulence on galloping instability," *ASCE Journal of the Engineering Mechanics Division*, Vol. 100, 1974, pp. 27–47.

[165] Belvins, R. D., "Flow-induced vibration," *Krieger Publishing Company, Florida*, 1990.

[166] Naudascher, E. and Rockwell, D., "Flow-Induced Vibrations, An Engineering Guide," *Dover Publications, New York*, 1994.

[167] Karakevich, M. I. and Vasilenko, A. G., "Closed analytical solution for galloping aeroelastic self-oscillations," *Journal of Wind Engineering and Industrial Aerodynamics*, Vol. 65, 1996, pp. 353–360.

[168] Laneville, A., Gartshore, I. S., and Parkinson, G. V., "An explanation of some effects of turbulence on bluff bodies," *Proc. of the Fourth International Conference on Wind Effects on Buildings and Structures, Cambridge University Press*, 1977, pp. 333–341.

[169] Alonso, G., Meseguer, J., and Prez-Grande, I., "Galloping instabilities of two-dimensional triangular cross-section bodies," *Experiments in Fluids*, Vol. 38, 2005, pp. 789–795.

[170] Alonso, G., Meseguer, J., and Prez-Grande, I., "Galloping stabilities of two-dimensional triangular cross-sectional bodies: A systematic approach," *Journal of Wind Engineering and Industrial Aerodynamics*, Vol. 95, 2007, pp. 928–940.

[171] Barrero-Gil, A., Sanz-Andres, A., and Roura, M., "Transverse galloping at low Reynolds numbers," *Journal of Fluids and Structures*, Vol. 25, 2009, pp. 1236–1242.

[172] Barrero-Gil, A., Sanz-Andres, A., and Alonso, G., "Hysteresis in transverse galloping: The role of the inflection points," *Journal of Fluids and Structures*, Vol. 25, 2009, pp. 1007–1020.

[173] Novak, M., "Aeroelastic galloping of prismatic bodies," *ASCE Journal of the Engineering Mechanics Division*, Vol. 96, 1969, pp. 115–142.

[174] Barrero-Gil, A., Alonso, G., and Sanz-Andres, A., "Energy harvesting from transverse galloping," *Journal of Sound and Vibration*, Vol. 329, 2010, pp. 2873–2883.

[175] Sirohi, J. and Mahadik, R., "Harvesting wind energy using a galloping piezoelectric beam," *ASME Journal of Vibration and Acoustics*, Vol. 134, 2012, pp. 1–8.

[176] Sirohi, J. and Mahadik, R., "Piezoelectric wind energy harvester for low-power sensors," *Journal of Intelligent Material Systems and Structures*, Vol. 22, 2012, pp. 2215–2228.

[177] Erturk, A. and Inman, D. J., "On the mechanical modeling of cantilevered piezoelectric vibration energy harvesters," *Journal of Intelligent Materials Systems and Structures*, Vol. 19, 2008, pp. 1311.

[178] Tiersten, H., *Linear Piezoelectric Plate Vibrations*, Plenum Press, New York, NY, 1969.

[179] Crawley, E. F. and de Luis, J., "Use of actuators as elements of intelligent structures," *AIAA Journal*, Vol. 25, 1987, pp. 1373–1385.

[180] Stanton, S. C., Erturk, A., Mann, B. P., Dowell, E. H., and Inman, D. J., "Nonlinear nonconservative behavior and modeling of piezoelectric energy harvesters including proof mass effects," *Journal of Intelligent Material Systems and Structures*, Vol. 23, 2012, pp. 183–199.

[181] Nayfeh, A. H. and Pai, P. F., *Linear and Nonlinear Structural Mechanics*, Wiley, New York, NY, 2004.

[182] Guyomar, D., Aurelle, N., and Eyraud, L., "Nonlinearities in Langevin transducers," *In: Proc. IEEE*, Vol. 1051, 1994, pp. 925–928.

[183] Guyomar, D., Aurelle, N., Richard, C., Gonnard, P., and Eyraud, L., "Piezoelectric ceramics nonlinear behavior. Application to Langevin tansducer," *Journal de Physique III*, Vol. 7, 1997, pp. 1197–1208.

[184] Joshi, S. P., "Nonlinear constitutive relations for piezoceramics materials," *Smart Materials and Structures*, Vol. 1, 1992, pp. 80–83.

[185] Arafa, M. and Baz, A., "On the nonlinear behavior of piezoelectric actuators," *Journal of Vibration and Control*, Vol. 10, 2004, pp. 387–389.

[186] *IEEE Standard on Piezoelectricity*, IEEE, New York, NY, 1987.

[187] Nayfeh, A. H. and Lacarbonara, W., "On the descretization of distributed-parameter systems with quadratic and cubic nonlinearities," *Nonlinear Dynamics*, Vol. 13, 1997, pp. 203–220.

[188] Nayfeh, A. H. and Lacarbonara, W., "On the descretization of spatially continuous systems with quadratic and cubic nonlinearities," *JSME International Journal Series C*, Vol. 41, 1998, pp. 510–531.

[189] Nayfeh, A. H., Arafat, H. N., Chin, C. M., and Lacarbonara, W., "Multimode interactions in suspended cables," *Journal of Vibration and Control*, Vol. 8, 2002, pp. 337–387.

[190] Lacarbonara, W., Rega, W., and Nayfeh, A. H., "Resonant nonlinear normal modes. part I: Analytical treatment for one dimensional structural systems," *Int. J. Non-Linear Mechanics*, Vol. 38, 2003, pp. 851–872.

[191] Nayfeh, A. H., "Reduced-order models of weakly nonlinear spatially continuous systems," *Nonlinear Dynamics*, Vol. 16, 1998, pp. 105–125.

[192] Nayfeh, A. H., *Perturbation Methods*, Wiley, New York, NY, 1973.

[193] Nayfeh, A. H., *Introduction to Perturbation Techniques*, Wiley, New York, NY, 1981.

[194] Sebald, G., Qiu, J., D, G., and Hoshi, D., "Modeling and characterization of piezoelectric fibers with metal core," *Japanese Journal of Applied Physics*, Vol. 44, 2005, pp. 6156–6163.

[195] Jiang, W. and Cao, W., "Nonlinear properties of lead zirconate titinate piezoceramics," *Journal of Applied Physics*, Vol. 88, 2000, pp. 6684–6689.

[196] Anderson, T. J., Nayfeh, A. H., and Balachandar, B., "Experimental verification of the importance of the nonlinear curvature in the response of a cantilever beam," *ASME Journal of Vibration and Acoustics*, Vol. 118, 1996, pp. 21–28.

[197] Arafat, H. N., Nayfeh, A. H., and Chin, C. M., "Nonlinear nonplanar dynamics of parametrically excited cantilever beams," *Nonlinear Dynamics*, Vol. 15, 1997, pp. 31–61.

[198] Nayfeh, A. H., *Nonlinear Interactions*, Wiley, New York, NY, 2000.

[199] Gilliatt, H. C., Strganac, T. W., and Kurdila, A. J., "On the presence of internal resonance in aeroelastic systems," *AIAA Journal*, Vol. 98, 2004, pp. 1955.

[200] Beran, P. S., Strganac, T. W., Kim, K., and Nichkawde, C., "Studies of Store-Induced Limit-Cycle Oscillations Using a Model with Full System Nonlinearities," *Nonlinear Dynamics*, Vol. 37, 2004, pp. 329–339.

[201] Strganac, T. W., J. Ko, J., and Thompson, D. E., "Identification and Control of Limit Cycle Oscillations in Aeroelastic Systems," *Proceedings of the 40th AIAA/ASME/ASCE/AHS/ASC Structures, Structural Dynamics, and Materials Conference and Exhibit*, AIAA Paper No. 99-1463, 1999.

[202] Nayfeh, A. H., *Method of Normal Forms*, Wiley, Berlin, 2011.

[203] Ghanem, R. G. and Spanos, P. D., *Stochastic Finite Elements: A Spectral Approach*, Dover Publications, New York, NY, 2003.

[204] Reagan, M., Najm, H. N., Ghanem, R. G., and Knio, O. M., "Uncertainty quantification in reacting flow simulations through non-intrusive spectral projection," *Combustion and Flame*, Vol. 132, 2003, pp. 545–555.

[205] Xiu, D. and Karniadakis, G. E., "Modeling uncertainty in flow simulations via generalized polynomial chaos," *Journal of Computational Physics*, Vol. 187, 2003, pp. 137–167.

[206] Hosder, S., Walters, R. W., and Rafael, P., "A non-intrusive polynomial chaos method for uncertainty propagation in CFD simulations," *In: Proceeding of the 44th AIAA Aerospace Sciences Meeting and Exhibit, Reno, Nevada, January 9-12, AIAA-2006-891*, 2006, pp. 641–659.

[207] Mola, A., "Multi-physics and multilevel fidelity modeling and analysis of Olympic rowing boat dynamics," *PhD Dissertation, Virginia Polytechnic Institute and State University*, 2010.

[208] Mola, A., Ghommem, M., and Hajj, M. R., "Multi-physics modelling and sensitivity analysis of Olympic rowing boat dynamics," *Sports Engineering*, Vol. 14, 2011, pp. 85–94.

[209] Bishop, R. E. D. and Hassan, Y., "The lift and drag forces on a circular cylinder oscillating in a flowing fluid," *Proceeding of the Royal Society, London*, Vol. 277, 1964, pp. 51–74.

[210] Hartlen, R. T. and Currie, I. G., "A lift-oscillator model for vortex-induced vibrations," *Proceeding of the American Society of Civil Engineers, Journal of Engineering Mechanics*, Vol. 69, 1970, pp. 577–591.

[211] Abdelkefi, A., Nayfeh, A. H., and Hajj, M. R., "Modeling and analysis of piezoaeroelastic energy harvesters," *Nonlinear Dynamics*, Vol. 67, 2011, pp. 925–939.